Markus Bröll
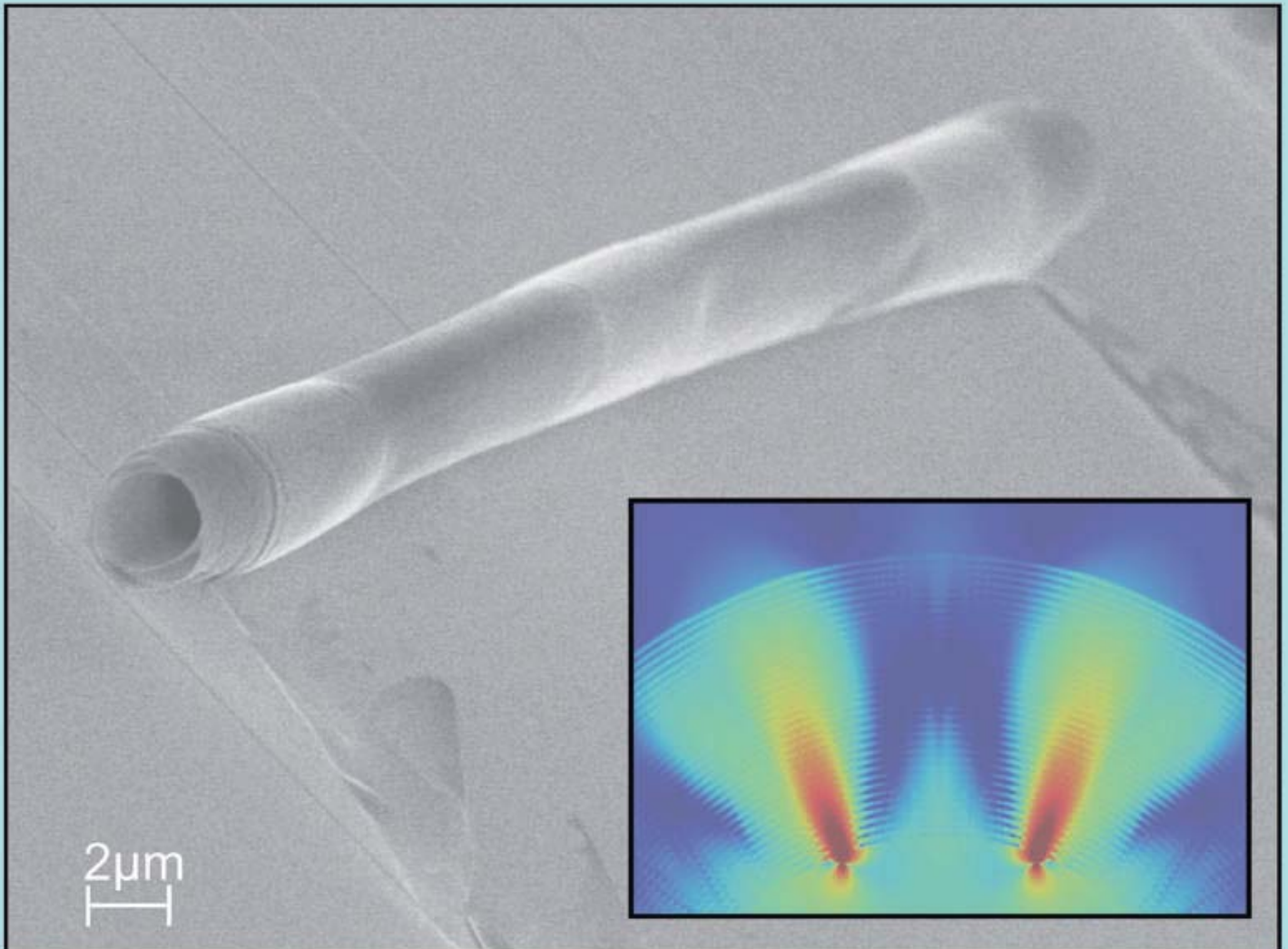
METAMATERIALS BASED ON METAL/SEMICONDUCTOR MICROROLLS

2µm

METAMATERIALS BASED ON METAL/SEMICONDUCTOR MICROROLLS

vorgelegt von
Markus Bröll
aus Unterhaching

Hamburg
2010

Gutachter der Dissertation	Prof. Dr. Detlef Heitmann
	Prof. Dr. Ulrich Merkt
Gutachter der Disputation	Prof. Dr. Detlef Heitmann
	Prof. Dr. Wolfgang Hansen
Datum der Disputation	19.02.2010
Vorsitzender des Prüfungsauschusses	Prof. Dr. Daniela Pfannkuche
Vorsitzender des Promotionsausschusses	Prof. Dr. Jochen Bartels
Dekan der Fakultät für Mathematik, Informatik und Naturwissenschaften	Prof. Dr. Heinrich Graener

1. Auflage 2010

Gedruckt auf säurefreiem Papier.

   978-3-86955-466-2

ABSTRACT

In this work novel three-dimensional metamaterials are realized by rolling-up strained metal/semiconducting nanolayers. The properties of these artificial, optical crystals can be described by effective parameters, which are investigated by numerical simulations as well as experimental transmission and reflection measurements.

Three-dimensional radial metamaterials were fabricated by rolling up a strained Ag/GaAs/InGaAs multilayer into a microroll with several rotations. The radial metamaterial, which is defined by the windings of the wall of the microroll, exhibits a dispersive and strongly anisotropic permittivity. It is shown by numerical simulations that such structures work as hyperlenses for specific wavelengths in the visible and near-infrared regime, i.e. they allow magnified, optical images with subwavelength resolution. To characterize the optical properties of the rolled-up hyperlenses a fiber-based transmission and reflection setup has been developed. From the measured reflectivity and transmission spectra the operation wavelength of the hyperlens could be determined. We could show experimentally that this wavelength depends on the ratio of layer thicknesses of the Ag/(In)GaAs layers and could be tuned in a wavelength range from 680 nm to 780 nm. Furthermore first near-field scanning microscopy measurements were performed in cooperation with the Univerity of Bourgogne to prove the magnifying subwavelength imaging of the hyperlens.

A further concept of this work is concerned with metamaterials made of arrays of many rolled-up Chromium/InGaAs microrolls. We have shown by analytical and numerical simulations that these structures interact resonantly with the magnetic component of an electromagnetic field and exhibit a negative permeability in the far infrared at frequencies of a few teraherz. By optimizing the roll-up process arrays with a high density of microrolls were prepared and first transmission measurements were performed in the far infrared.

INHALTSANGABE

In dieser Arbeit werden durch Aufrollen verspannter Metall/Halbleiter Schichten neuartige, dreidimensionale Metamaterialien realisiert. Die Eigenschaften dieser künstlichen optischen Kristalle können durch effektive Parameter beschrieben werden. Diese werden durch numerische Simulationen, sowie Transmissions- und Reflexionsmessungen experimentell untersucht.

Radiale Metamaterialien wurden durch mehrfaches Aufrollen einer verspannten Ag/GaAs/InGaAs Multilage zu einem Mikroröllchen hergestellt. Das radiale Metamaterial wird dabei durch die Windungen der Röllchenwand definiert und besitzt eine dispersive und stark anisotrope Permittivität. Durch numerische Simulationen wurde gezeigt, dass diese Strukturen für bestimmte Wellenlängen im sichtbaren- und nahinfraroten Bereich als Hyperlinsen wirken, d.h. vergrößerte, optische Abbildungen mit Subwellenlängenauflösung ermöglichen. Zur optischen Charakterisierung der Hyperlinsen wurde ein faserbasierter Transmissions- und Reflexionsmeßaufbau entwickelt. Aus den gemessenen Transmissions- und Reflexionsdaten konnte die Arbeitswellenlänge der aufgerollten Hyperlinsen bestimmt werden. Wir konnten experimentell zeigen, dass die Wellenlänge vom Schichtdickenverhältnis der Ag/(In)GaAs Schichten abhängt und konnten sie in einem Wellenlängenbereich von 680-780 nm variieren. Zum experimentellen Nachweis der vergrößernden Subwellenlängenabbildung durch die Röllchenwand wurden außerdem erste Nahfeldmikroskopmessungen an der Universität von Burgund durchgeführt.

Ein weiteres Konzept dieser Arbeit beschäftigt sich mit Metamaterialien, welche nicht durch die Wände einzelner Mikrorollen definiert sind, sondern aus einem Gitter vieler aufgerollter Chrom/InGaAs Mikroröllchen bestehen. Wir haben durch analytische sowie numerische Simulationen gezeigt, dass diese periodischen Strukturen resonant mit der magnetischen Komponente des elektro-magnetischen Feldes wechselwirken und somit eine negative Permeabilität im Ferninfaroten bei Frequenzen von wenigen THz aufweisen. Durch eine Optimierung des Aufrollprozesses wurden Arrays mit einer hohen Röllchendichte hergestellt und erste Transmissionsmessungen im Ferninfraroten durchgeführt.

CONTENTS

APPENDICES

LIST OF FIGURES

LIST OF TABLES

CHAPTER 1

INTRODUCTION

Over the last decade the new scientific field of metamaterials has grown rapidly. Metamaterials are artificial crystals, whose unit cell sizes and lattice constants are much smaller than the wavelength of the transmitted light. Therefore the optical properties of a metamaterial can be described approximately by effective parameters, as known from classical electrodynamics, like the permittivity ϵ and the permeability μ. For most metamaterials reported so far, the unit cells consist of metal and dielectric structures. By changing the composition of these structures it is possible to tune the effective optical parameters of the metamaterial. This has led to a broad range of new materials with optical properties not known so far in nature. For example metamaterials consisting of arrays of so called split ring resonators can couple to the magnetic field component of an electromagnetic wave and their permeability becomes negative for a specific frequency range. These metamaterials have gained much interest since together with a negative ϵ they exhibit a negative refractive index, as proposed theoretically by Veselago in 1968 [Ves68]. Metamaterials with such novel optical properties have opened the door to a broad range of new physical phenomena, like e.g. cloaking devices [Sch06], superlenses with subwavelength resolution [Pen00, Fan05, Liu07] or inversed Cherenkov radiation [Xi09]. While first pioneering experiments have been performed at microwave wavelengths where metamaterials have structure sizes of several millimeters, experiments have been extended into the near-infrared regime during the last years [Sha05, Dol06]. However, to fulfill the condition of an effective medium, the structure sizes of these metamaterials have to be in the range of a few hundred nanometers and the preparation of such metamaterials becomes quite demanding. Most of the structures prepared by electron-beam lithography (EBL) or focused-ion beams (FIB) are two dimensional, i.e. they do not extend in the direction of the wave vector of the transmitted light. Only few methods like direct laser writing or successive EBL and spin-on glass methods have realized the fabrication of three-dimensional metamaterials [Val08, Liu08] for the near-infrared regime.

In this work the preparation of metamaterials made of rolled-up metal/semiconductor microrolls was established. Expanding the selfrolling mechanism of semiconducting nanolayers [Pri00] to metal/semiconductor systems allows the fabrication of three-dimensional metamaterials with a high control of layer thicknesses [Sch09]. After describing the concept of the rolling-up process in chapter 2, a rolled-up three-dimensional metamaterial for the visible and near infrared is discussed in chapter 3. This metamaterial consists of a rolled-up superlattice of metal and semiconducting layers. The superlattice exhibits a permittivity which is highly anisotropic in directions parallel and perpendicular to the layers. A promising application of these structures are so called hyperlenses. Hyperlenses allow imaging of objects with a spatial resolution well below the Abbe limit, which limits the resolution of conventional far-field microscopes to about half the wavelength of the scattered light [Abb73]. To determine the optical properties of the rolled-up superlattices reflection and transmission measurements were performed. For the latter measurements a nanosized light source was developed, which could be inserted into the microroll by a special microscope-manipulation setup. We could show by these measurements that the permittivity of the rolled-up superlattices exhibits a metallic dispersion with a characteristic plasma frequency ω_p. By means of finite difference time domain simulations we revealed that rolled-up superlattices with the measured optical parameters are expected to exhibit hyperlensing at ω_p [Sch09]. The position of ω_p, i.e. the operating frequency of the hyperlens, could be tuned by varying the ratio of layer thicknesses of the superlattice. To observe subwavelength imaging through the rolled-up hyperlens first near-field scanning microscopy measurements were performed in cooperation with the University of Bourgogne.

Another concept to realize metamaterials by metal/semiconductor microrolls is discussed in chapter 4. Now, the metamaterial is defined by an array of many rolled-up microrolls. We show with numerical simulations that such a metamaterial exhibits a negative permeability at wavelengths in the far-infrared regime. The preparation of the arrays as well as first transmission measurements with a Fourier spectrometer are presented. Chapter 5.1 summarizes all results obtained so far and gives a short outlook to further experiments, which can be performed in the future.

CHAPTER 2

PRINCIPLES OF ROLLED-UP NANOTECH

The rolling up of nanolayers into micro- and nanorolls was first demonstrated by Prinz et al. [Pri00]: Strained bilayers minimize their strain energy after lift off from the substrate by rolling up into microrolls. Different material systems can be used for the strained bilayers, like strained semiconducting films [Pri00, Sch01, Sch05], or, as shown recently, strained polymer nanomembranes [Mei09]. In our work microrolls consisting of metal and the III-V semiconductors (In)GaAs were prepared. The principle is shown in figure 2.1: A thin metal film is evaporated on top of a semiconductor layer system grown by molecular-beam epitaxy (MBE). All samples were grown by Dr. Holger Welsch and Andrea Stemann in the group of Professor Dr. Wolfgang Hansen. The layer system consists of an AlAs sacrificial layer on top of a GaAs substrate and a strained bilayer of $In_xGa_{1-x}As$ and GaAs. The GaAs substrate and the AlAs layer have almost the same lattice constant of $0.55\,nm$ and $0.56\,nm$, respectively [Ada85]. The lattice constant of the $In_xGa_{1-x}As$ layer in the relaxed state is larger than for AlAs and can be approximately calculated by the concentration-weighted average of the lattice constants of InAs and GaAs [Veg21, Woi96]:

$$d(In_xGa_{1-x}As) = 0.61\,x + 0.56\,(1-x) \tag{2.1}$$

Depending on the Indium concentration, one has to distinguish between different growth mechanisms of the $In_xGa_{1-x}As$ on top of the AlAs, as shown in the phase diagram in figure 2.2 [Mat74, Hey01, Wel07]. For Indium concentrations $x < 0.4$ and layer thicknesses $d < d_{crit}$ the $In_xGa_{1-x}As$ grows pseudomorphically, i.e. the lateral lattice constant of $In_xGa_{1-x}As$ is adapted to the lattice constant of AlAs. This leads to strain inside the $In_xGa_{1-x}As$ layer. Above a critical thickness d_{crit} the strain is released into misfit dislocations [Mat74], while for an Indium content $x > 0.4$ quantum dots are formed by the

so called Stranski-Krastanov growth [Str39, Hey01]. Typically the $In_xGa_{1-x}As$ is grown pseudomorphically to maximize the strain stored in the multilayer to be rolled up.

After the removal of the AlAs sacrificial layer, which is typically done be selective etching with hydrofluoric acid [Hjo96], the strained $In_xGa_{1-x}As/GaAs$ bilayer and the metal film can minimize their strain energy by up-bending and forming a microroll. The radius r of the microroll is determined by the growth parameters and can be calculated approximately by a model of Tsui and Clyne [Tsu97]:

$$\frac{1}{r} = \frac{6(1-\nu)\,E_1E_2h_1h_2(h_1+h_2)(a_2-a_1)/a_1}{E_2^2h_2^4 + 4E_1E_2h_2^3h_1 + 6E_1E_2h_2^2h_1^2 + 4E_1E_2h_2h_1^3 + E_1^2h_1^4} \qquad (2.2)$$

where ν is the Poisson ratio of $In_xGa_{1-x}As$ and $a_{1/2}$ are the lattice constants, $E_{1/2}$ the Young's moduli and $h_{1/2}$ the thicknesses of the strained ($In_xGa_{1-x}As$) and unstrained layers (GaAs/metal), respectively. This model was established originally only for epitaxially grown monocrystalline layers. To include the influence of the evaporated, polycrystalline metal film into this model we approximate the unstrained GaAs/metal layer by a pure GaAs layer of equal thickness. This approximation neglects the additional strain induced by metals with high melting temperatures (e.g. chromium) and differences in elastic properties of the metal and the GaAs [Sch05, Tho89]. However, for our structures the measured microroll radii were in good agreement with the theoretical values using the above approximations.
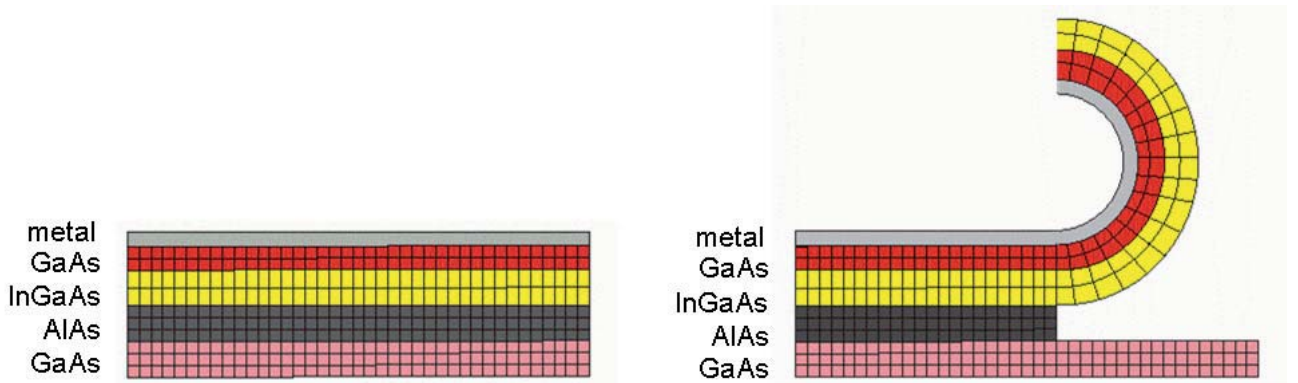
Figure 2.1: Principle of the roll up process of a strained metal/(In)GaAs bilayer into a microroll.

By rolling up metal/semiconductor layers into microrolls, three-dimensional metamaterials, which are periodic in the radial direction, can be prepared in a single step. In our experiments large arrays of microrolls with only one rotation (chapter 4) as well as

multirotated microrolls (chapter 3) were prepared. The specific preparation steps for each type of metamaterial will be discussed in detail in the corresponding chapters.
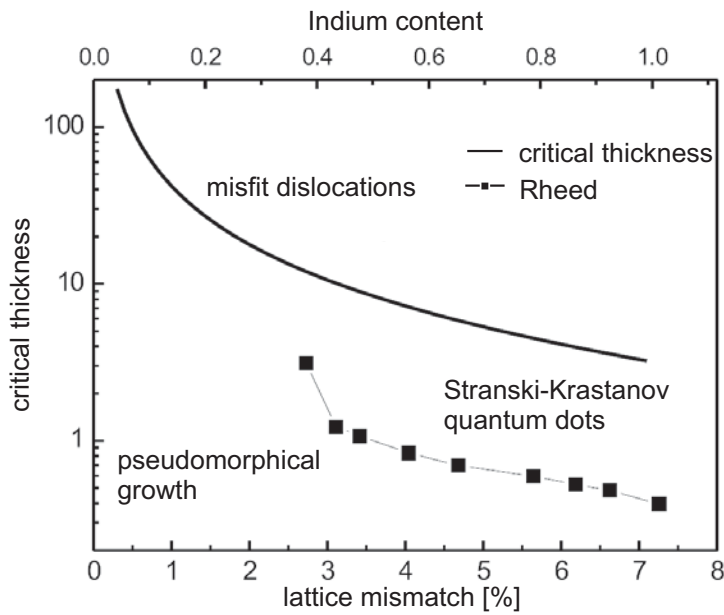
Figure 2.2: Phase diagram for the epitaxial growth of strained $In_xGa_{1-x}As$ on $AlAs$. The solid line shows the theoretical curve for the critical thickness with respect to lattice mismatch and Indium content [Mat74]. The phase boundary for Stransky-Krastanov growth (black points) was experimentally measured by Christian Heyn [Hey01].

CHAPTER 3

METAMATERIALS MADE OF ROLLED-UP METAL/SEMICONDUCTOR SUPERLATTICES

A special class of metamaterials is formed by metal/dielectric superlattices. If the layer thicknesses of the superlattice are much thinner than the wavelength of the transmitted light, the optical properties of the superlattice can be described by an effective and highly anisotropic permittivity tensor. The components of this tensor and therefore the optical properties of the metamaterial can be tuned by varying the thickness ratio of the dielectric and metal layers. These metamaterials offer interesting applications like so called hyperlenses, which allow imaging with subwavelength resolution. As described in chapter 2 superlattices of semiconducting (In)GaAs as dielectric and metal layers can be formed by rolled-up metal/semiconductor microrolls. The self-organized formation of the superlattice offers a high control over layer thicknesses. Furthermore the curvature of the microroll allows the fabrication of magnifying hyperlenses. In the following chapters the theory of light transmission through rolled-up metal/semiconductor microrolls as well as the concept of hyperlensing will be described. In the experimental part a special micro-manipulation microscope setup will be presented which allowed us to observe transmission and reflection of the rolled-up superlattices experimentally and to retrieve their effective optical constants.

3.1 Electromagnetic fields inside superlattices and effective media

As a first step the electromagnetic fields inside a plane superlattice as shown in figure 3.1 will be calculated. The superlattice which extends in z direction consists of periodic layers of two materials with different permittivities ϵ_1 and ϵ_2 and thicknesses d_1 and d_2. The superlattice is illuminated by a plane wave, whose wavevector can be separated in a transversal component $k_{||}$ parallel and a component k_z perpendicular to

the layers of the superlattice. Without loss of generality we chose a two-dimensional $x - z$ coordinate system, such that $k_{\parallel}$ points into x direction and k_z points into z direction.

The transmission and reflection coefficients of the superlattice can be calculated by a transfer matrix approach [WK91]. Within this approach the fields inside each layer i of the superlattice are expressed as a superposition of two plane waves propagating in positive and negative z direction:

$$\vec{E}_i(z) = \begin{pmatrix} E_i^+ \exp(i(k_x x + k_{zi} z - \omega t)) \\ E_i^- \exp(i(k_x x - k_{zi} z - \omega t)) \end{pmatrix} \tag{3.1}$$

Due to continuity conditions for plane media the wavevector k_x is continous through the whole superlattice while in each layer i the wavevectors k_{zi} obey the dispersion relation:

$$k_{zi} = \sqrt{\left(\frac{\omega}{c}\right)^2 \epsilon_i - k_x^2} \tag{3.2}$$

 As shown in appendix A1 the fields on the left and on the right side of a single layer are associated to each other by a phase matrix $\hat{P}$:

$$\vec{E}_{i\,left} = \hat{P}_i \vec{E}_{i\,right} \tag{3.3}$$

$$\hat{P}_i = \begin{pmatrix} \exp(ik_z d) & 0 \\ 0 & \exp(-ik_z d) \end{pmatrix} \tag{3.4}$$

The fields on both sides of an interface between two layers i and k are related to each other by continuity conditions which are expressed by the transfer matrix $\hat{T}$:

$$\vec{E}_i = \hat{T}_{ik} \vec{E}_k \tag{3.5}$$

$$\hat{T}_{ik} = \begin{pmatrix} 1 + \kappa^{ik} & 1 - \kappa^{ik} \\ 1 - \kappa^{ik} & 1 + \kappa^{ik} \end{pmatrix} \tag{3.6}$$

The constant κ^{ik} depends on the polarization of the plane wave:

$$\kappa_p^{ik} = \frac{\epsilon_i k_{zk}}{\epsilon_k k_{zi}} \qquad transverse\,magnetic\,polarization \tag{3.7}$$

$$\kappa_s^{ik} = \frac{k_{zk}}{k_{zi}} \qquad transverse\,electric\,polarization \tag{3.8}$$

One unit cell of the superlattice consists of a bilayer of both optical media which is periodically repeated in z direction with the lattice constant $\Delta = d_1 + d_2$. The fields of two subsequent unit cells are related to each other by the matrix $\hat{M}_n$:

$$\vec{E}_n = \hat{M}_n \vec{E}_{n+1} = \hat{P}_1 \hat{T}_{12} \hat{P}_2 \hat{T}_{21} \vec{E}_{n+1} \tag{3.9}$$
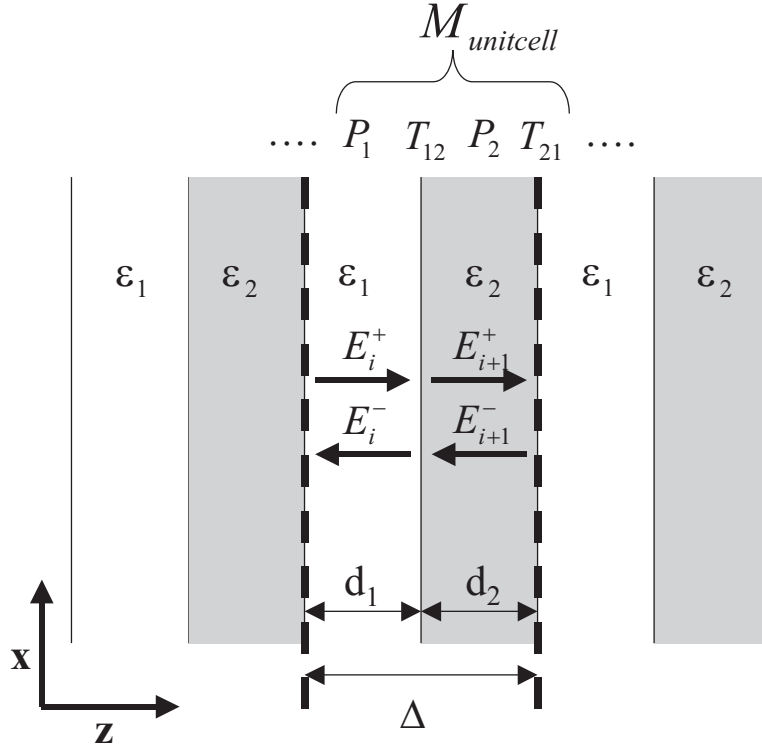
Figure 3.1: Sketch of a superlattice consisting of periodic layers with permittivities ϵ_1 and ϵ_2 and thicknesses d_1 and d_2. One unit cell of the superlattice is formed by a double layer of both materials. This unit cell is periodic in z direction with a lattice constant $\Delta = d_1 + d_2$.

Furthermore a periodic boundary condition can be applied to the plane waves inside the superlattice due to the periodicity of the superlattice :

$$\vec{E}_n = \exp(ik_z^*\Delta)\vec{E}_{n+1} \tag{3.10}$$

In analogy to electrons in crystalline solids the solutions for the fields, which obey equation 3.10 are called Bloch waves with the Bloch wavevector k_z^*. Comparing equations 3.9 and 3.10 results in the eigenvalue equation:

$$\hat{M}_n\vec{E}_i = \exp(ik_z^*\Delta)\vec{E}_i \tag{3.11}$$

where the Bloch wavevector k_z^* is connected to the eigenvalue λ of the transfer matrix $\hat{M}_n$ by:

$$\lambda = \exp(ik_z^*\Delta) \tag{3.12}$$

The eigenvalue λ depends on the transversal wavevector k_x and on the frequency ω, so equation 3.12 gives the dispersion relation for the Bloch wavevector k_z^*. In the effective medium approximation the layer thicknesses are much smaller than the wavelength of

transmitted light. Therefore both sides of 3.12 can be expanded in powers of the layer thicknesses d_1 and d_2. As shown in appendix A2 for TM polarization the dispersion relation becomes:

$$\left(\frac{\omega}{c}\right)^2 = \frac{k_x^2}{\epsilon_z} + \frac{k_z^{*2}}{\epsilon_x} \tag{3.13}$$

with

$$\epsilon_x = \frac{d_1}{\Delta}\epsilon_1 + \frac{d_2}{\Delta}\epsilon_2 \tag{3.14}$$

$$\epsilon_z = \left(\frac{d_1}{\Delta}\frac{1}{\epsilon_1} + \frac{d_2}{\Delta}\frac{1}{\epsilon_2}\right)^{-1} \tag{3.15}$$

Equation 3.13 is the dispersion relation for an anisotropic medium whose optical properties are described by a diagonal permittivity tensor with components ϵ_x parallel and ϵ_z perpendicular to the superlattice. We will investigate the frequency dependence of these components on the example of a superlattice consisting of GaAs and silver layers. Figure 3.2 shows the permittivities of bulk silver and GaAs which are taken from the literature [Pal97]. The permittivity of silver can be described by a Drude model, with some additional contributions from d-band transitions at energies above $2\,\text{eV}$. At the plasma frequency $\omega_p \approx 4\,\text{eV}$, which lies in the ultraviolet regime, the real part of the permittivity becomes zero. The semiconductor GaAs is a dielectric with a high optical permittivity. Above an energy of $1.4\,\text{eV}$ absorption inside this material increases strongly, due to the excitation of electron-hole pairs above the band gap of GaAs. Combining both materials into a superlattice with a thickness of layer ratio $\eta = \frac{d_{GaAs}}{d_{Ag}} = 1.3$ results in an effective medium with permittivity tensor components ϵ_x and ϵ_z, which are plotted in figure 3.2(b). The real part of the permittivity ϵ_x shows a metallic behavior similar to silver, but with a shifted plasma frequency $\omega_p \approx 1.6\,\text{eV}$ in the red visible regime. The real part of the component ϵ_z shows a Lorenz resonance and changes sign at the frequency ω_{z0}. The strong change in the real part of ϵ_z is associated with a sharp peak in its imaginary part due to Kramers-Kronig relation [Jac98]. The imaginary part of ϵ_x increases only sligthly at higher frequencies due to the high absorption of the GaAs layers. Both permittivitiy components can be tuned by varying the ratio of layer thicknesses η, i.e. a metamaterial with tunable permittivity is formed by the metal/dielectric superlattice. As will be shown in the next section the high anisotropy of the permittivity tensor leads

to an unsusual light propagation through this effective medium and allows the formation of an image with subwavelength resolution.

3.1.1 Imaging through superlattices with subwavelength resolution

The spatial resolution of far-field optical microscopy is limited by the so called Abbe limit [Abb73] and lies in the range of half the wavelength of the illuminating light. Optical lenses made of superlattices offer an enhanced spatial resolution as shown in the following:

An optical microscope collects light which is scattered by the illuminated object of interest. The wavevector distribution of the scattered light is connected to the shape of the object by its Fourier transform:

$$\vec{E}(k_x, k_y, t) = \int \int_{xy} \vec{E}(x, y, t) \, exp(ik_x x + ik_y y + ik_z z - \omega t) \, dx \, dy \qquad (3.16)$$

where k_x and k_y are the transversal wavevector components perpendicular to the optical
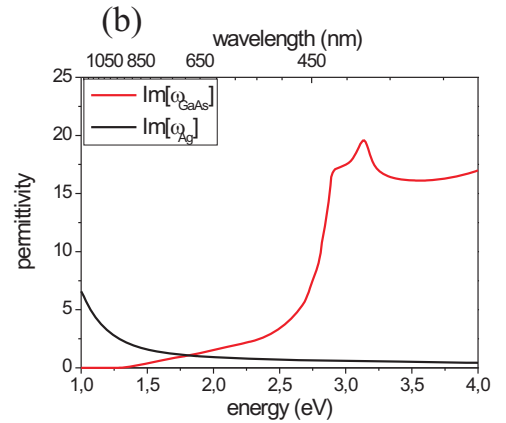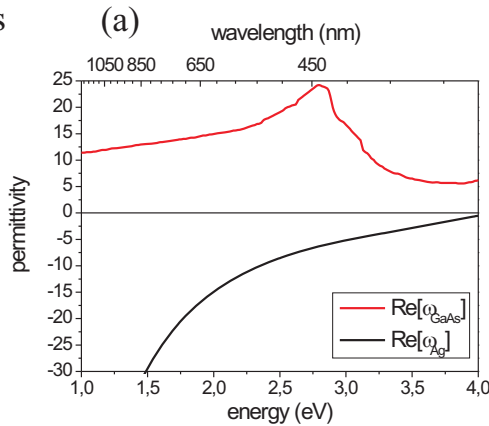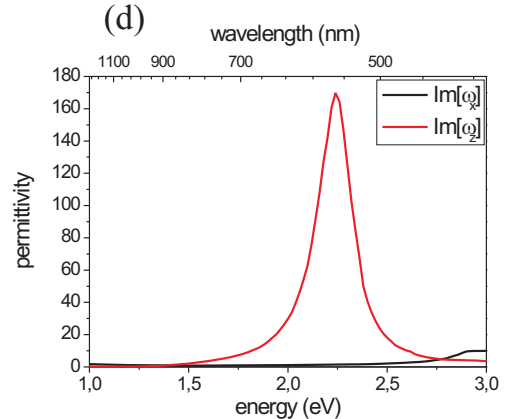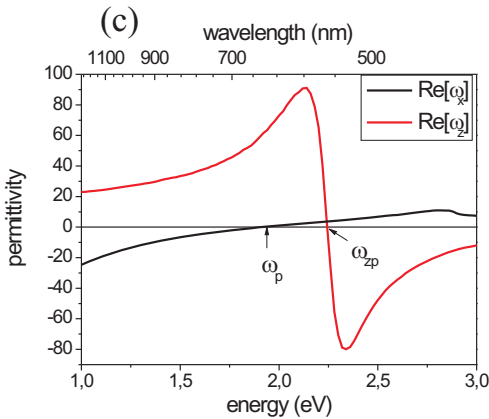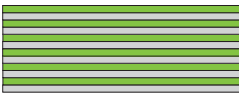
Figure 3.2: (a)-(b) Real and imaginary parts of the permittivities of bulk GaAs and silver. Data were taken from the literature [Pal97]. (c)-(d) Real and imaginary parts of the components of the effective permittity tensor for a silver/GaAs superlattice with a layer of thickness ratio $\eta = 1.3$.

axis. The light transmits through a medium to the far field where it is collected by an optical lens system and transfered to the image plane. For a perfect image all wavevectors scattered from the object have to pass to the image plane, otherwise spatial information about the object will be lost in the back Fourier transformation. The electric field which passes through a medium can be calculated by the transmission coefficient $t(\omega, k_{||})$ which depends on the frequency as well as on the transversal wavevector components $k_{||} = \sqrt{k_x^2 + k_y^2}$:

$$\vec{E}_{trans}(\omega, k_{||}) = \vec{E}_{scatt}(\omega, k_{||})\, t(\omega, k_{||}) \tag{3.17}$$

For a medium with permittivity ϵ the transversal wavevector components are connected to the component k_z which is parallel to the optical axis of the imaging system by the dispersion relation:

$$k_z^2 = \epsilon \left(\frac{\omega}{c}\right)^2 - k_{||}^2 \tag{3.18}$$

where ω is the frequency of light, and c is the light velocity in vacuum. For vacuum all wavevectors lie on a sphere with radius $k_0 = \omega/c$. Fields with larger transversal wavevectors than k_0 decrease exponentially with increasing distances from the scattering object. They do not propagate to the image plane since the wavevector k_z becomes imaginary in this regime. Therefore the transmission coefficient $t(\omega, k_{||})$ drops to zero for $k_{||} > k_0$, which limits the spatial resolution Δ to half the wavelength of light [Abb73]:

$$\Delta = \frac{2\pi}{2k_0} = \lambda/2 \tag{3.19}$$

To increase the spatial resolution of an imaging system a material which also transmits higher wavevectors has to be brought into the near field of the scattering object. These materials are called hyperlenses. An ideal hyperlens should meet the following conditions:

- All transversal wavevectors scattered from the object should be transmitted through the lens

- The hyperlens should form an image of the object at a well defined image plane

- For a perfect image different wavevectors have to be transmitted with equal amplitude

To understand how superlattices can fullfill the above conditions for hyperlensing the transmission coefficients in dependence of the incident transversal wavevector as well as

the wavevector dispersion inside the superlattice have to be calculated. In a first step we will focus on the effective medium approximation, i.e. the layer widths of the superlattice will be assumed to be infinitely thin. In accordance with the experimental part the permittivities of the metal and the dielectric layers are chosen to be silver and GaAs. However to demonstrate the underlying physics we will assume that the imaginary parts of the dielectric functions are scaled down by a factor $\alpha = 0.1$.

As shown in appendix $A1$ the transmission coefficient through a superlattice can be calculated by a transfer matrix which connects the fields on both sides of a superlattice of n rotations. In the effective medium approximation the transmission through the superlattice corresponds to the transmission through a slab of thickness d with an anisotropic permittivity tensor

$$T(\omega, k_{||}) = \left| t(\omega, k_{||}) \right|^2 = \left| \frac{2}{2 \cos(k_z^* d) - i \left(\frac{k_z^* \epsilon}{k_{z0} \epsilon_{||}} + \frac{k_{z0} \epsilon}{k_z^* \epsilon_{||}} \right) \sin(k_z^* d)} \right|^2. \tag{3.20}$$

In this equation ϵ is the permittivity and k_{z0} the z component of the wavevector in the surrounding medium and k_z^* is the wavevector component perpendicular to the layers of the superlattice which obeys the dispersion relation of equation 3.13.

The dispersion of the normalized wavevector k_z^*/k_0 is plotted in figure 3.3 for different frequencies versus the normalized transversal components k_x/k_0 and k_y/k_0, where the wavevector $k_0 = \frac{\omega_0}{c}$ is the maximum propagating wavevector in vacuum. In contrast to the dispersion of an isotropic medium where the wavevector components lie on a sphere with diameter k_0 for all frequencies, the dispersion in the anisotropic medium changes drastically with frequency. Three different cases are shown: For $\epsilon_{||} < 0$ and $\epsilon_z > 0$ (frequency ω_1) no lateral components smaller than $k_0 \sqrt{\epsilon_z}$ propagate through the superlattice. For larger lateral wavevectors the component k_z becomes real and increases in a hyperbolic fashion. The transmission in this regime is almost zero for small lateral componentss $k_{||} < k_0$. For wavevectors larger than $k_{||} < k_0 < k_0 \sqrt{\epsilon_z}$ a strong peak appears, which can be assigned to a plasmon resonance on the effective medium/air interface. For $k_{||} > k_0 \sqrt{\epsilon_z}$ light waves can propagate through the effective medium slab and guided Fabry Perot modes are formed due to internal total reflections inside the effective medium slab. The wavevector positions where these modes appear depend strongly on the layer thickness of the slab. In this regime there is no cutoff in the transmission for large wavevectors. In practice the transmission of wavevectors is limited by absorption inside the layers as well as by the finite width of the single layers of the superlattice, which will

be discussed in more detail in the next section. Since small wavevectors are absent in the transmission spectrum and large wavevectors are transmitted dominantly at the position of the Fabry-Pérot resonances, there will be modulations in the optical image. In this case the information on the object has to be reconstructed by detailed knowledge of the transmission function.

In the second case of interest $\epsilon_\parallel$ is close to zero while the component ϵ_z is large and positive (frequency ω_2). As can be seen in equation 3.13, k_z^* is close to zero for all lateral wavevectors k_x and k_y and the dispersion surface changes to a flat disk. In the transmission spectrum a strong Fabry-Pérot resonance appears slightly above k_0. For larger lateral wavevectors the transmission becomes equal to 1 up to a wavevector $k_m = \frac{\omega}{c}\sqrt{\epsilon_z}$. Therefore the effective medium works as a perfect lens for wavevectors $k_\parallel \gg k_0$ and $k_\parallel < \frac{\omega}{c}\sqrt{\epsilon_z}$. The component ϵ_z can be tuned by the ratio of the layer thicknesses d_{Ag} and d_{GaAs}. For equal layer widths $|\epsilon_z|$ becomes infinitely large at the same frequency where $\epsilon_\parallel = 0$. Therefore for $d_1 = d_2$ there is no upper limit for lateral wavevectors which are transmitted through the superlattice. In practice both GaAs and silver layers show wavelength dependent absorption, so by different ratios of d_{GaAs} and d_{Ag} an operation wavelength can be adjusted which minimizes the aborption in the effective medium and therefore maximizes the resolution of the hyperlens.

Another important case occurs if $\epsilon_\parallel > 0$ and $\epsilon_z < 0$. The dispersion changes to a hyperbola which is centered around the k_z^* axis. The opening angles of the two hyperbolic cones are given by the ratio $\frac{|\epsilon_z|}{\epsilon_\parallel}$ and become flat for higher frequencies. There is no upper limit for $k_\parallel$, but the transmission is dominated by Fabry-Pérot interferences, which disturb the image.

Beside the transmission of high lateral wavevector components an image has to be formed by the effective medium. This image formation can be illustrated by looking at the group velocity inside the effective medium. In contrast to an isotropic medium, where the group velocity is parallel to the wavevector, this is not the case in an anisotropic medium, as shown in figure 3.4. The group velocity $\vec{v}_g \sim \vec{\nabla}_k\omega$ in k-space is proportional to the gradient of the energy dispersion. Graphically this means that the group velocity points to a direction perpendicular to the dispersion planes and draws a finite angle with the wavevector $\vec{k}$ which points from the origin to the dispersion curve. At the frequencies ω_2 and ω_3 the dispersion is flat and the group velocity points to the same direction for all $k_\parallel$. This means that all waves scattered from the object are channeled in a beamlike
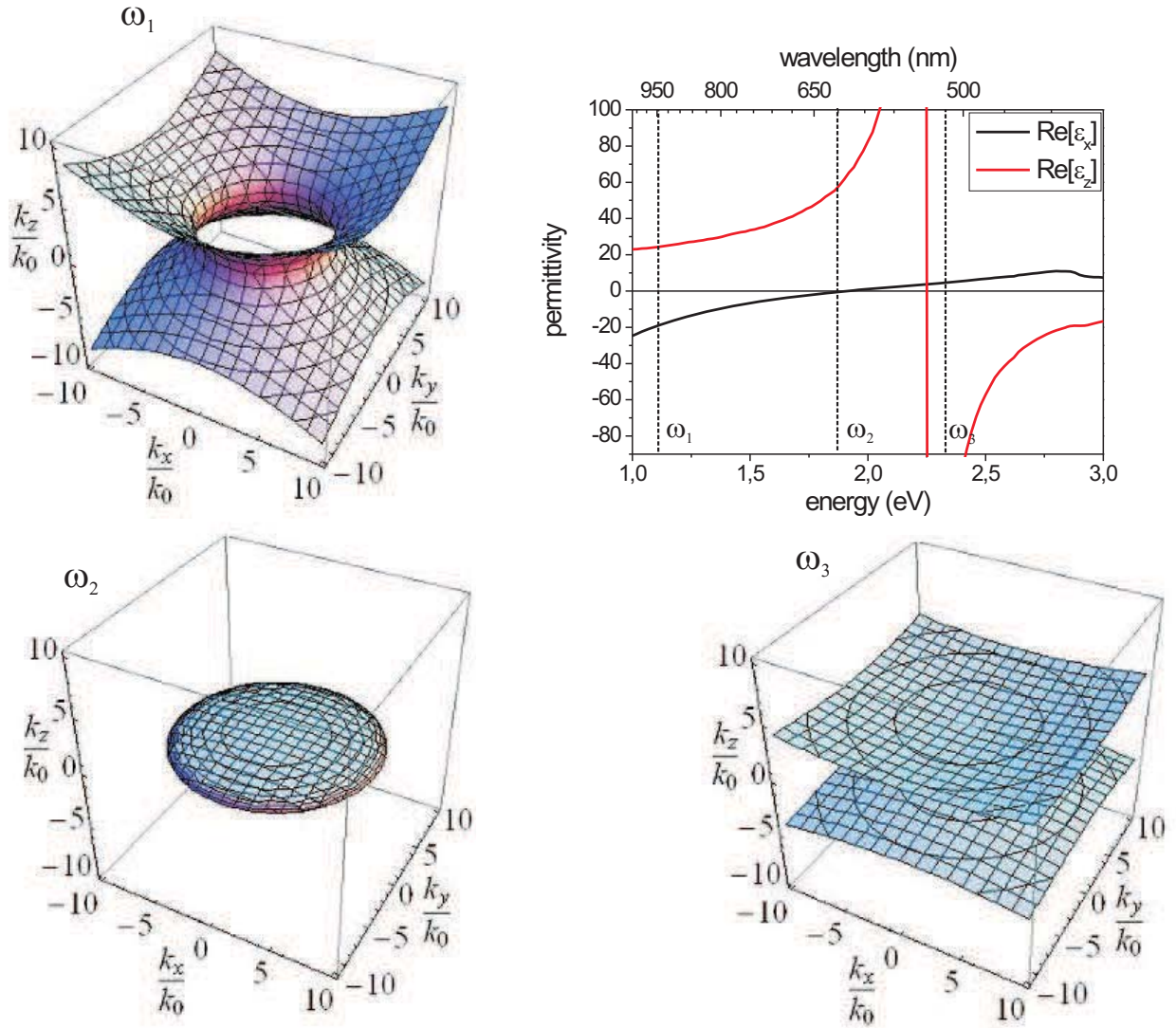
Figure 3.3: Wavevector dispersion relation for different photon energies in an effective medium consisting of thin silver and GaAs layers. The ratio of layer thicknesses is $\eta = 1.3$. Due to the high anisotropy of the permittivity tensor higher wavevectors can be transmitted.

fashion from one side of the superlattice to the other side where an image of the object is formed. This channeling is illustrated with finite difference time domain simulations (FDTD) in figure 3.5 for a single scattering angle. A Gaussian beam impinges on a slab of an isotropic medium (a) as well as on an anisotropic medium with $\epsilon_z \gg \epsilon_x$ (b). In the first case the Gaussian beam gets refracted in the same way as its wavefronts, so the wavevector is parallel to the group velocity. In the second case the wavefronts of the beam enclose an angle $\alpha \neq 90°$ with the group velocity which transfers the wave packet almost perpendicularly through the slab.

Permittivity	Dispersion	Transmission

$\varepsilon_{||} = \varepsilon_z$

$\varepsilon_{||} < 0, \varepsilon_z > 0$

$\varepsilon_{||} = 0, \varepsilon_z > 0$

$\varepsilon_{||} > 0, \varepsilon_z < 0$
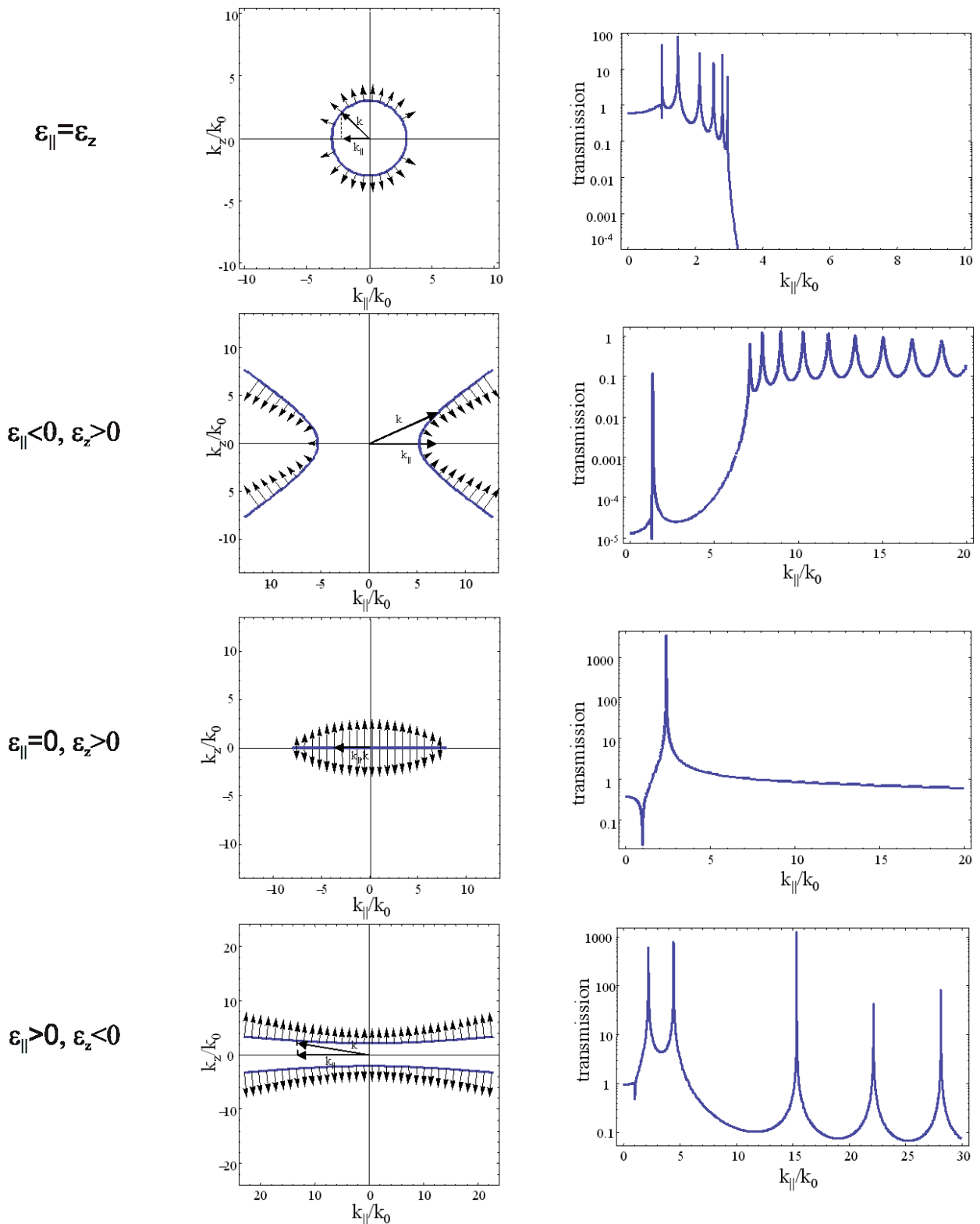
Figure 3.4: Wavevector dispersion for $k_y = 0$ for an isotropic medium and for the three different frequencies ω_1, ω_2 and ω_3 discussed in the text. The direction of the group velocity which is perpendicular to the dispersion relation in k-space is plotted by arrows. In the region $\epsilon_{||} = 0$ the group velocities point to the same direction for all lateral wavevectors $k_{||}$. This leads to channeling of all wavevectors through the effective medium slab.
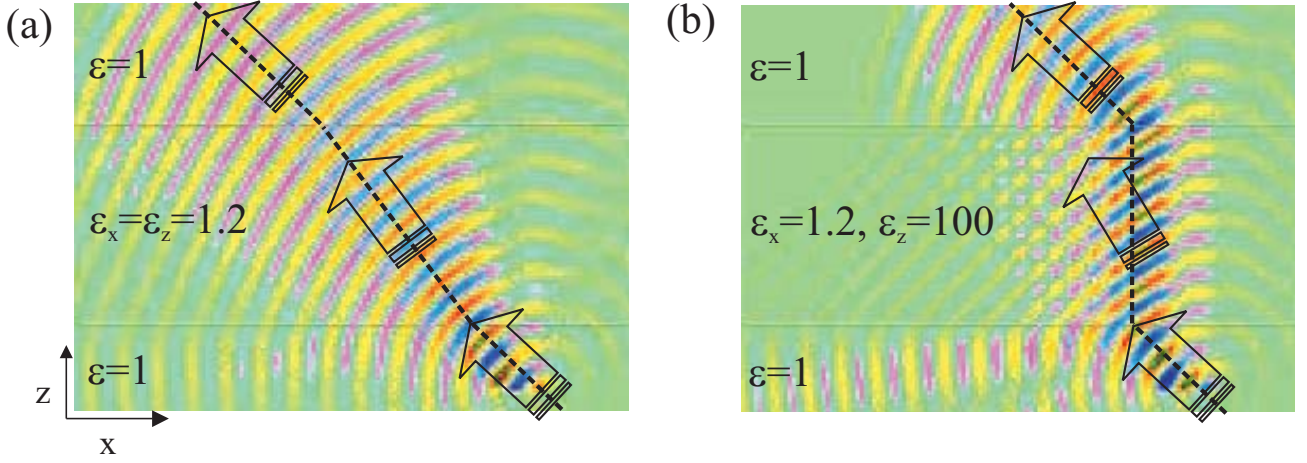
Figure 3.5: Numerical simulation of a light beam impinging on an effective medium with an (a) isotropic permittivity $\epsilon = 1.2$ and (b) an highly anisotropic permittivity ($\epsilon_x = 1.2$, $\epsilon_z = 100$). The arrows are parallel to the wavevectors of the beam, while the dashed line shows the propagation of the wave packet along the group velocity.

The findings of this section can be summarized as follows: An effective medium with an highly anisotropic permittivity tensor is able to image objects with subwavelength resolution. In the case of no losses the best resolution is achieved for $\epsilon_{||} = 0$ and $\epsilon_z \to \infty$, which means that the thicknesses of metal and dielectric layers have to be equal and the operating wavelength has to be adjusted in such a way that $\epsilon_{Dielektric}(\lambda_W) = -\epsilon_{Metal}(\lambda_w)$. In this case all large wavevectors which carry the subwavelength details of the illuminated object are transfered in a channel-like behavior through the effective medium and a perfect image is formed on the other side. In the following section influences on the resolution due to finite layer widths as well as absorption will be discussed in detail.

3.1.1.1 Influence of finite layer thicknesses on the resolution of a hyperlens

In the case of finite layer widths the wavevector dispersion for k_z^* has to be solved by the eigenvalue dispersion 3.12. Due to the periodicity of the superlattice in z direction a Brillouin zone is formed in k-space which extends on the k_z axis from $-\pi/\Delta$ to π/Δ, where $\Delta = d_{Ag} + d_{GaAs}$ is the periodicity of the superlattice. As shown in figure 3.6(a) the dispersion curve is bent towards the boundaries of the Brillouin zone, thus limiting the lateral wavevector to a maximum value. According to the changes of the dispersion curves the transmission drops sharply above this maximum wavevector, as shown in figure 3.6(b).
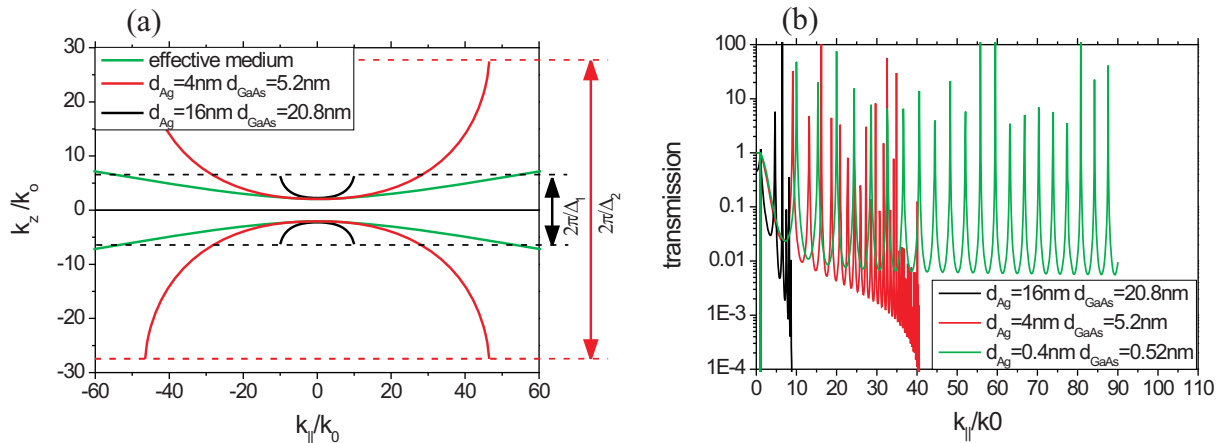
Figure 3.6: (a) Wavevector dispersion for finite layer widths in the hyperbolic regime at the frequency $\hbar\omega = 2.3\,\mathrm{eV}$. Due to the finite layer thickness of the superlattice unit cell $\Delta = d_{Ag} + d_{GaAs}$ a Brillouin zone is formed which extends on the k_z−axis from $-\pi/\Delta$ to π/Δ (dashed lines). For finite layer width the dispersion curves are bent up towards the border of the Brillouin zone, which sets a limit to the maximum lateral wavevector $k_{||}$. (b) Corresponding transmission spectrum versus $k_{||}/k_0$. Above the wavevector cutoff shown in (a) the transmission drops to zero, thus limiting the resolution of the hyperlens.

3.1.1.2 Influence of absorption on the resolution of a hyperlens

So far absorption of electromagentic waves inside the superlattice has been neglected. However for a superlattice consisting of silver and GaAs layers absorption arises due to interband excitations in the semiconducting GaAs and due to the Drude like behavior of the silver film. This absorption reduces strongly the resolution of the hyperlens. To investigate this influence the imaginary parts of the GaAs and silver permittivities were scaled by an absorption factor α, which is tuned from zero (no absorption) to 1 (absorption for GaAs and silver, known from the literature). Figure 3.7 shows the transmission function in the channeling regimes at $\epsilon_{||} = 0$, $\epsilon_z > 0$ and $\epsilon_{||} > 0$, $\epsilon_z \ll 0$ for different scaling factors α. For higher absorption the total transmission through the superlattice decreases and the transmission falls off for larger wavevectors $k_{||}$. This leads to a lower resolution of the hyperlens. On the other hand the Fabry-Pérot resonances shown in figure 3.7(b) are diminished. Therefore absorption can be helpful in reducing modulations from the image which arise due to the prefered transmission of wavevectors at the position of Fabry-Pérot interferences and the superlattice works as a perfect lens in both optical regimes of figure 3.7(a) and (b).

At first sight the high absorption in the GaAs layers seems to be disadvantageous with
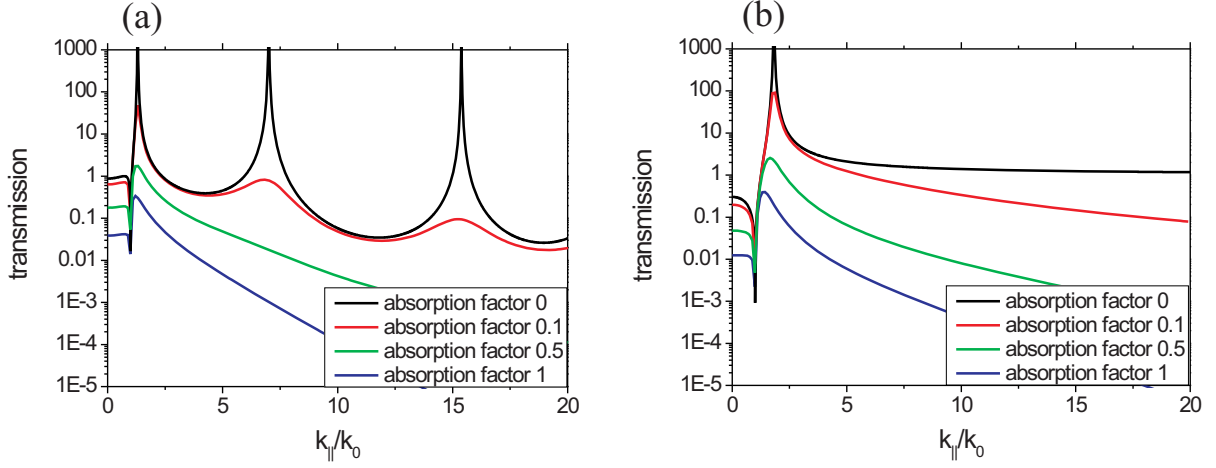
Figure 3.7: Influence of absorption on the transmission through a superlattice. The permittivities of the single layers are those of GaAs and silver but the absorption is varied by a parameter α from the lossless case to experimental data absorption.

respect to other dielectrics like glasses, which show almost no absorption at all in the visible. However by using a different thickness of layer ratio the channeling regimes can be tuned to energies below the bandgap of GaAs, where the absorption becomes zero. Furthermore it is possible to integrate quantum structures like (Al)GaAs quantum wells or (In)GaAs quantum dots inside the GaAs layers. When optically or electrically pumped these quantum structures exhibit optical gain which could compensate the absorption of the metal layers. Possible realizations of these optically active superlattices will be discussed in more detail in chapter 5.1.

3.1.2 The image of a double slit transmitted through a superlattice consisting of GaAs and silver layers

We will now investigate the image resolution of a silver/GaAs hyperlens using realistic permittivities for the single layers. At the plasma frequency of the effective medium an image is formed on the surface of the hyperlens. This image can be calculated by evaluating equation 3.17. First the Fourier transform of the field distribution at the position of the object has to be calculated to get the scattering profile:

$$\vec{E}(k_x, t) = \frac{1}{\sqrt{2\pi}} \int_{x,y} E(x, y, t) \exp(-i(k_x x + k_y y + k_z z - \omega t)) dx \, dy$$

As field sources we will assume two slits in an absorbing medium which are illuminated by a plane wave and which are separated by the distance a from each other. The slits are

infinitely long in y direction and infinitely thin in x direction, so the field distribution in x direction can be described by two Gaussian-Delta functions:

$$\vec{E}(x, z = 0, t) = \delta \left(x - \frac{a}{2} \right) + \delta \left(x + \frac{a}{2} \right) \tag{3.21}$$

The Fourier transform of this field distribution is just the sum of two complex exponential functions, so the scattered field distribution is:

$$\vec{E}(\omega, k_x, t) = \exp \left(ik_x \left(x - \frac{a}{2} \right) + ik_z z - i\omega t \right) + \exp \left(ik_x \left(x + \frac{a}{2} \right) + ik_z z - i\omega t \right) \tag{3.22}$$

where k_z is the wavevector in the sourrounding medium, which will be air in this example. After passing through the hyperlens with total thickness d the transmitted field distribution in k-space becomes

$$\vec{E}_{trans}(\omega, k_x, t) = \vec{E}(\omega, k_x, t) \cdot t(\omega, k_x, d) \tag{3.23}$$

The spatial distribution of the image on the surface of the hyperlens is calculated by the reverse Fourier transformation:

$$\vec{E}_{Image}(\omega, x, z = d, t) = \int_{k_x} \vec{E}_{trans}(\omega, k_x, t) \, dk_x \tag{3.24}$$

Figure 3.8(a) shows the transmission versus lateral wavevector for a $300 \, \text{nm}$ thick hyperlens consisting of silver and GaAs with a thickness ratio $\eta = 1$. Due to the large absorption inside the silver and the GaAs layers the transmission drops for larger wavevectors. Nevertheless the transmission for the hyperlens is still larger than 1% for wavevectors up to $8 \, k_0$, while the transmission for pure GaAs (red curve) becomes zero for wavevectors $k_{||} > \sqrt{\epsilon_{GaAs}} k_0$. Figure 3.8(b) shows the image of two line sources with a distance of $200 \, \text{nm}$ from each other, which is created on top of the hyperlens. Since the distance of both slits is much smaller than the wavelength of the transmitted light ($600 \, \text{nm}$) the slits cannot be resolved anymore by optical microscopy in vacuum (green curve). However after passing through the hyperlens a clear image of both slits is created. The local maximum in the middle of both slit images results from prefered transmission of wavevectors between $1.3 \, k_0$ and $4 \, k_0$, which forms modulations in the transferred image. By detailed knowledge of the transfer function of the hyperlens the original image can be retrieved. Figure 3.8 shows clearly that subwavelength details can be transmitted through a GaAs/silver superlattice.
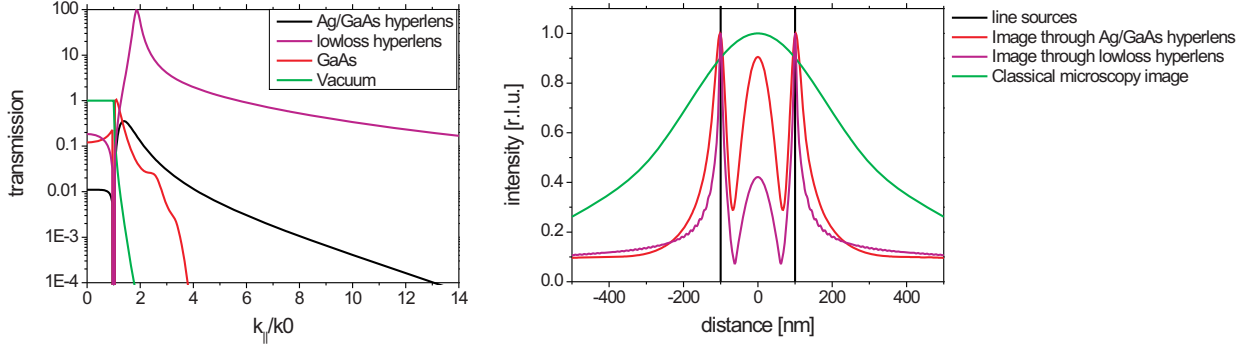
Figure 3.8: (a) Transmission versus lateral wavevector through an effective medium slab of 300 nm thickness, consisting of GaAs and silver layers with a thickness ratio $\eta = 1$. The frequency of the transmitted light is chosen to be the plasma frequency of the effectice medium: $\hbar\omega_p = 2.0$ eV. The pink curve shows the transmission through the hyperlens with reduced absorption ($\alpha = 0.1$). For comparison the transmission through a single GaAs layer (red curve) as well as through vacuum (green curve) is plotted. While for GaAs and vacuum there is a cutoff at $1\,k_0$ and $3.8\,k_0$ the transmission for the hyperlens structure is still larger than 1% for wavevectors up to $8\,k_0$. (b) Image of two line sources formed on the surface of the hyperlens. Although the distance of 200 nm between both line sources is much smaller than the wavelength of light, two clear peaks can be observed in the image plane. If the image is observed by an optical microscope in air (green curve) both line sources cannot be resolved anymore.

3.1.3 Cylindrical hyperlenses

So far it has been shown that a superlattice can transform subwavelength details of an object to an image plane. However the image size is still the same as on the entrance plane and cannot be resolved by conventional far-field microscopy. One possible way to couple the near field information of an object to the far field was suggested in [Jac06] by cylindrically curved hyperlenses. Figure 3.9(a) shows a sketch of a hyperlens in a cylindrical geometry. The effective permittivities $\epsilon_{||}$ and ϵ_z of the plane superlattice are transformed to their counterparts in polar coordinates, with ϵ_ϑ pointing in tangential direction and ϵ_r pointing in radial direction:

$$\epsilon_\vartheta = \frac{\epsilon_1 + \epsilon_2}{1 + \eta} \tag{3.25}$$

$$\epsilon_r = \left(\frac{1}{\epsilon_1} + \frac{\eta}{\epsilon_2}\right)^{-1} \tag{3.26}$$

(a)

(b)
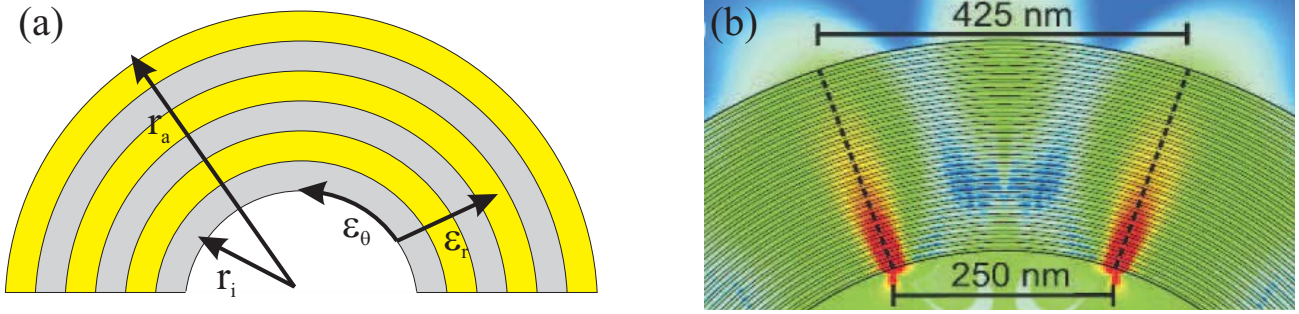
Figure 3.9: (a) Sketch of a cylindrical hyperlens consisting of metal (grey) and dielectric (yellow) layers. (b) Finite difference time domain simulation of the field propagation through a cylindrical hyperlens consisting of 20 rotations of silver (10 nm) and GaAs (20 nm). The H_y component of the magnetic field, which is perpendicular to the plane of the hyperlens, is plotted in false colors (red colors mean high intensity, blue colors low intensity). Two dipole sources are located directly at the inner wall of the superlattice in a distance of 250 nm from each other. On the outer surface of the hyperlens the distance between both dipole sources is magnified by a factor of 1.7.

Therefore, like for a plane geometry, a cylindrical hyperlens works as a perfect lens at the plasma frequency ω_p, where $\epsilon_\vartheta = 0$. For this regime the field propagation of two dipoles placed very close to the inner surface of the cylindrical hyperlens is shown in figure 3.9(b): The hyperlens consist of 20 layers of GaAs and silver with a thickness of layer ratio of 2. This corresponds to a wavelength $\lambda_p = 700$ nm where the tangential permittivity ϵ_ϑ becomes zero. Since the lateral distance between both dipoles is 250 nm, it is not possible to resolve them separately at this wavelength by a conventional microscope. The field emitted from both TM-polarized dipoles was calculated by a finite difference time domain solver and the transversal component of the magnetic field is plotted in a false color plot. As can be seen from the simulation the field distribution of the dipoles is channeled radially through the superlattice and an image is formed at the outer side of the hyperlens at the radius r_a. Therefore the lateral distance between both dipoles is magnified by the magnification factor $V = \frac{r_a}{r_i} = 1.7$ to a distance of 425 nm. This distance can be separated clearly with an optical microscope, so the near field distribution of both dipole sources is transfered to the far field.

3.2 Preparation of cylindrical hyperlenses by rolled-up microrolls

A promising way to fabricate magnifying hyperlenses is rolling-up strained semiconducting layers and metal films into microrolls. As sketched in figure 3.10, the walls of

the microroll form a radial metal/semiconductor superlattice. In contrast to successive evaporation methods [Liu07], the formation of the superlattice (SL) is performed in a self-assembled, single step. This leads to high quality SL with a precise control over the layer thicknesses [Den07, Sch05]. To achieve a large magnification with this rolled-up superlattice in the channeling regime, a high curvature as well as a large winding number of the microroll is required. The reachable number of rotations crucially depends on the optimization of growth parameters and the lithographic procedure. A preparation method to form multirotated superlattices was developed in this work. This method will be discussed in the following (figure 3.11):

Our MBE-grown samples consist of a strained $Al_xGa_{1-x}As/In_xAl_yGa_{1-x-y}As$ bilayer on top of a 40 nm thick AlAs sacrificial layer. We used an aluminum amount of up to 30% inside the strained bilayer to shift the band gap of the semiconductor to higher energies and therefore to reduce the absorption at wavelengths in the near infrared. All samples were grown by Dr. Holger Welsch and Andrea Stemmann in the group of professor Dr. Wolfgang Hansen in our institute. The exact composition of the wafers is listed in appendix B.1.

As a first preparation step a thin silver film is evaporated on top of the strained bilayer, which serves as a roll-up template. Silver is the metal of choice due to its low
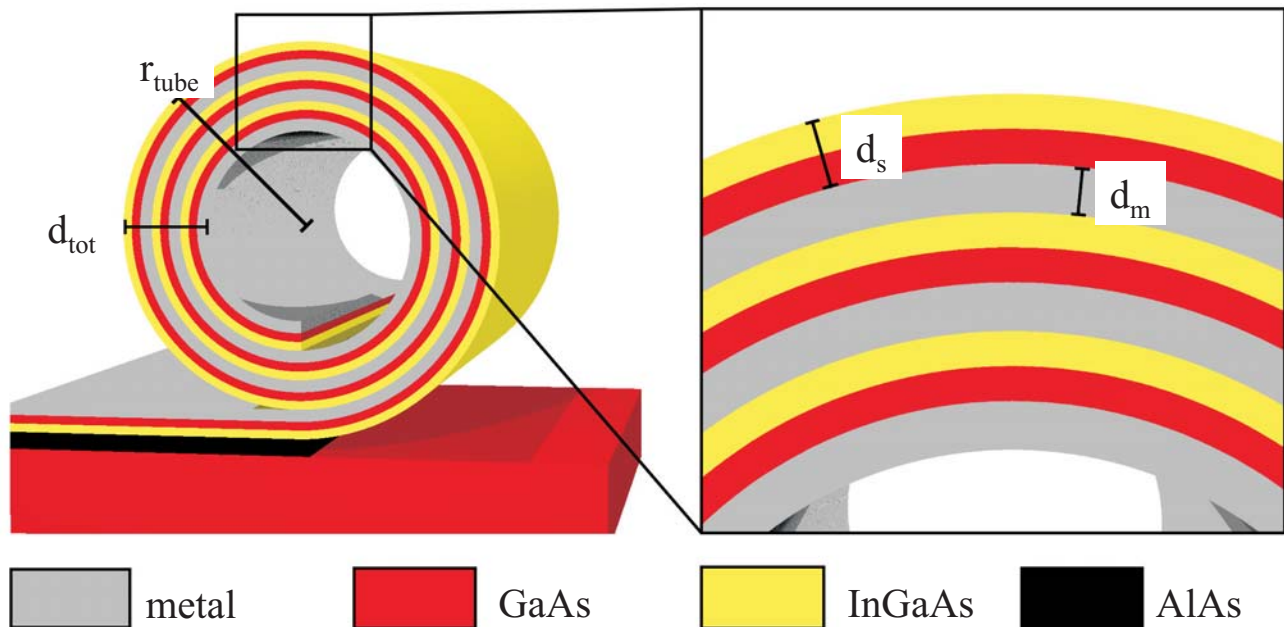
Figure 3.10: Sketch of a microroll consisting of three rotations of (In)GaAs and metal. The wall of the microroll defines a metal/semiconductor superlattice with thicknesses d_s for the semiconductor and d_m for the metal layers.

absorption coefficient at visible and near-infrared wavelengths [Pal97]. The films were evaporated at a pressure of less than $1 \cdot 10^{-7}$ mbar at an evaporation rate of 0.1 nm/s. Both thickness and roughness of the films were measured by atomic force microscopy. The average roughness (rma) of the films was about 1.5 nm for layers thicker than 10 nm. During the preparation of several microroll samples we observed that the roll-up process of the microroll is hindered by the silver film. Most of the microrolls did not roll up compactly, i.e. gaps were formed between successive silver/(In)GaAlAs layers. This might be attributed to the low tensile strain of metals like silver and gold, which does not support the roll-up of the semiconducting layers [Sch05]. To minimize the influence of the silver film, a mesa of silver stripes was prepared by optical lithography with lateral dimensions of several microns. These stripes are rolled-up instead of a whole, closed silver film, i.e. a smaller amount of silver has to be rolled-up by the strained bilayer. We observed that this method increased the yield of rolled-up microrolls as well as their layer compactness.

After evaporation, a shallow etching step is performed: Parts of the (In)GaAlAs layers on both sides of the silver stripes are removed, so only the bilayer below the silver stripe structure remains strained. While in chapter 4.2 the rolling direction could be controlled by the ratio of the microroll length and the rolling distance, this is not possible for microrolls with multiple rotations, since the rolling distance is much larger than the length of the microroll. Therefore the etching has to be stopped inside the InGaAlAs layer and the AlAs sacrificial layer remains completely covered by semiconducting material. Otherwise the microroll would roll up from its side edges in an undefined way. On the other hand the etching depth has to be deep enough, so the semiconducting layers on the edge between strained and unstrained regions are ripped and the microroll can roll up easily. Therefore a precise control of the etching rate is required. We used diluted phosphoric acid [Men05] in a ratio of $H_2O : H_3PO_4 = 500 : 1$, which gave us a high control of the etching depth (etching rate: 1.3 nm/s) for layer thicknesses of a few tens of nanometers.

At one side of the silver stripes a so called starting edge is etched deeply into the AlAs layer which is removed selectively by diluted hydrofluoric acid. Since etching of the AlAs starts only at this starting edge, the microroll is rolled-up along the direction defined by the shallow-etched mesa. For this last etching step the concentration of the hydrofluoric acid was varied between 5% and 10%. Generally a higher yield of rolled-up microrolls was achieved by using higher concentrated hydrofluoric acid, which might be due to the increased formation of hydrogen bubbles which support the roll-up process [Den05].

During the last etching step the silver films are exposed to hydrofluoric acid. We justified by atomic force microscopy that the silver films are resistant against this etchant. Comparing the silver films before and after etching revealed only a slight increase of the surface roughness from 1.4 nm to 2.2 nm. Therefore we believe that the optical properties of the silver films are not changed due to the preparation process.

Figure 3.12(a) shows a scanning electron micrograph of a typical microroll prepared during this work, which consists of seven rotations of 34 nm thick (In)AlGaAs and 16 nm thick silver layers. With an inner radius of $r_{tube} = 1.5\,\mu m$ the magnification of this rolled-up hyperlens is expected to be $V = 1.23$.

To investigate the quality of the rolled-up layers the microroll was cut by focused ion beam (FIB), so the layer cross-section could be inspected with scanning electron microscopy (SEM). As shown in figure 3.12(b) the microroll is not rolled-up compactly and gaps appear between successive layers at the left side of the microroll. However, on the top side of the microroll, where transmission and reflection measurements will be performed, all layers are in close contact to each other and form a well defined, compact superlattice (figure 3.12(c)).
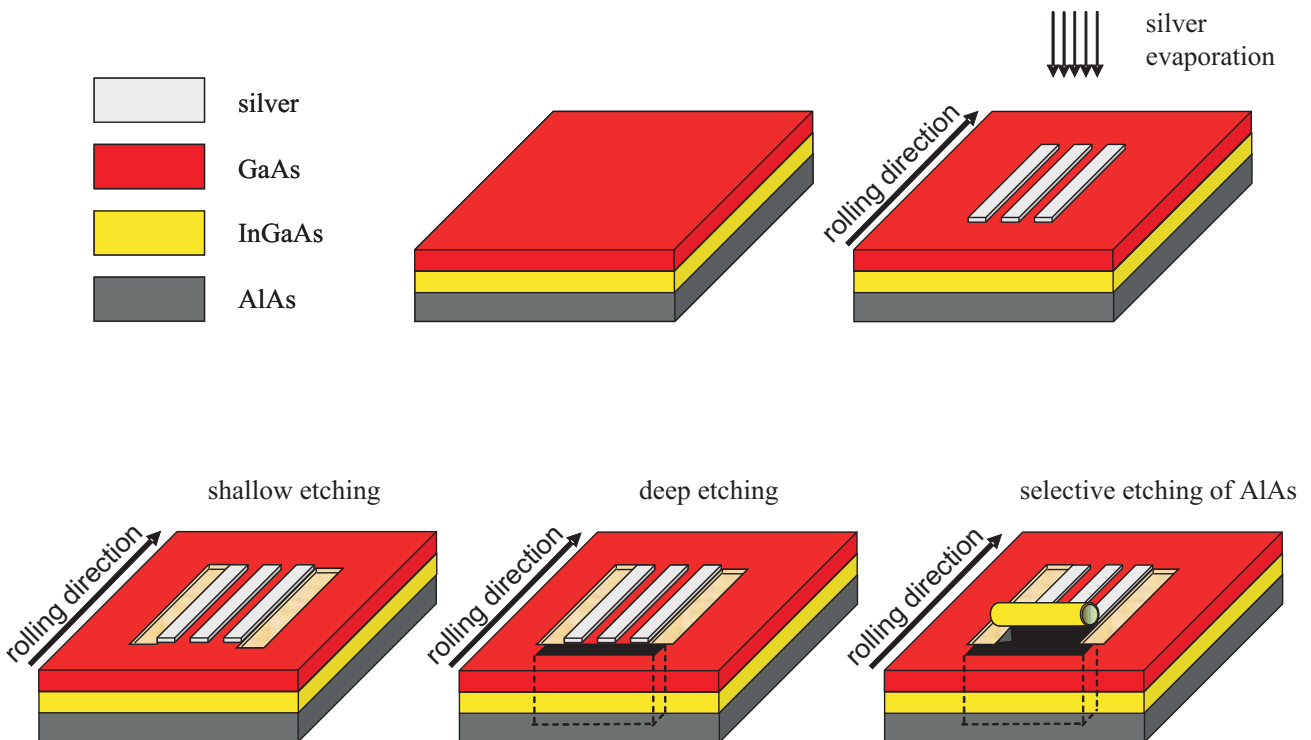
Figure 3.11: Preparation steps for rolled-up metal/semiconductor microrolls
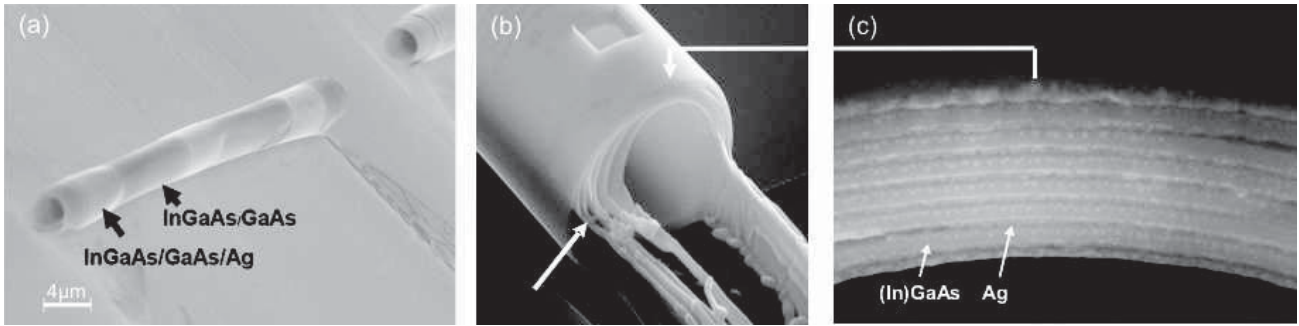
Figure 3.12: (a) Scanning electron micrograph of a rolled-up microroll consisting of 7 layers of 35 nm (In)AlGaAs and 16 nm silver. (b) The same microroll after FIB preparation, which was performed by Daniel Stickler from the group of professor Dr. Hans Peter Oepen. On the left side of the microroll gaps appear between successive layers (white arrow), while a compact superlattice is formed on the top as shown in (c). The silver layers show a darker image contrast than the (In)GaAs layers and can be clearly separated in the SEM image.

As described in section 3.1.1 the single layer thicknesses influence the transmission through the superlattice as well as the resolution of the hyperlens. Therefore we also prepared microrolls with thinner layer thicknesses of $d_s = 20$ nm which approach the effective medium limit in a better way. For microrolls with even thinner layer thicknesses, we found that the preparation exhibits a very low yield due to the limited control of the shallow etching step.

3.3 Transmission and reflection measurements on rolled-up microrolls

To investigate the optical properties of rolled-up metal/semiconductor superlattices we have performed transmission and reflection measurements. Since our microrolls form closed cylinders with diameters of a few microns we faced the problem to get a light source inside the microroll that exhibits subwavelength features which could be imaged onto the outside of the rolled-up hyperlens. Such a light source was realized by tapered fiber tips which were metallized and structured by FIB. Furthermore a special microscope setup was constructed which allowed us to manipulate the tapered fiber tips into the microroll and to illuminate it from its inside for transmission measurements.

3.3.1 Preparation of nanosized light sources

The preparation of sharp tips from optical fibers is a well known procedure in near-field scanning microscopy (NSOM). Optical fibers are widely used waveguides, which guide

light over long distances with low absorption. The light wave is guided inside a core (with typical diameters of 5 µm for single mode fibers), which is surrounded by a 200 µm thick glass with an higher refractive index. In our experiment we used single mode fibers which only allow the propagation of one single mode inside the core for wavelengths larger than the cutoff wavelength of the fiber (for our latest fibers we chose a cutoff wavelength of about 800 nm). Two different methods are commonly applied to taper fibers to a sharp tip: Etching methods using hydrofluoric acid [Lam98] and heat pulling methods [Yak93]. We chose the latter method due to its simplicity and the formation of long, thin fiber tips with small opening angles. A home built setup was constructed whose principle is shown in figure 3.13: An optical fiber is heated by an external heating source to a temperature well above its melting point, which is about 1100 °C for typical optical fibers. For such high temperatures we had to use a propane gas burner, whose flame reaches a maximum temperature of about $1900\,°C$. During the heating process the fiber is pulled by a weight. Due to the softening of the glass above its melting point the fiber gets longer, while its diameter decreases until the fiber breaks at a very fine tip end. For optimizing the pulling process the temperature as well as the pulling weights were varied. The temperature of the propane gas flame could be only controlled by varying the oxygen flow mixed with the propane gas and by putting the fiber into different regions of the flame. Best results were obtained by heating the fiber at a flame position where the flame color becomes almost black, indicating a temperature of about 1900 °C. Furthermore the total gas flow should be minimized, otherwise the fiber tips buckle. The fibers were pulled by weights of about 200 g. With this setup tip diameters in the range of 1 µm could be prepared in a reproducible way. For smaller tip diameters better defined heating sources like CO_2 lasers are favorable.

The pulled sharp fiber tips were metallized afterwards to prevent light leakage out of the tip end. In our first experiments we evaporated aluminum onto the fiber, while the fiber was rotated by a rotation stage inside the evaporation chamber. This metal cladding is widely used in near-field scanning microscopy due to the low light penetration depth of aluminum, which is only some ten nanometers at optical wavelengths. However, the aluminum formed grains on the fiber which scattered out the light in an undefined way. We achieved much smoother films by sputtering of AuPd in a magnetron sputter chamber. During the sputtering process the fiber does not need to be rotated, since the metal is deposited uniformly from all sides onto the fiber. Due to the slightly larger
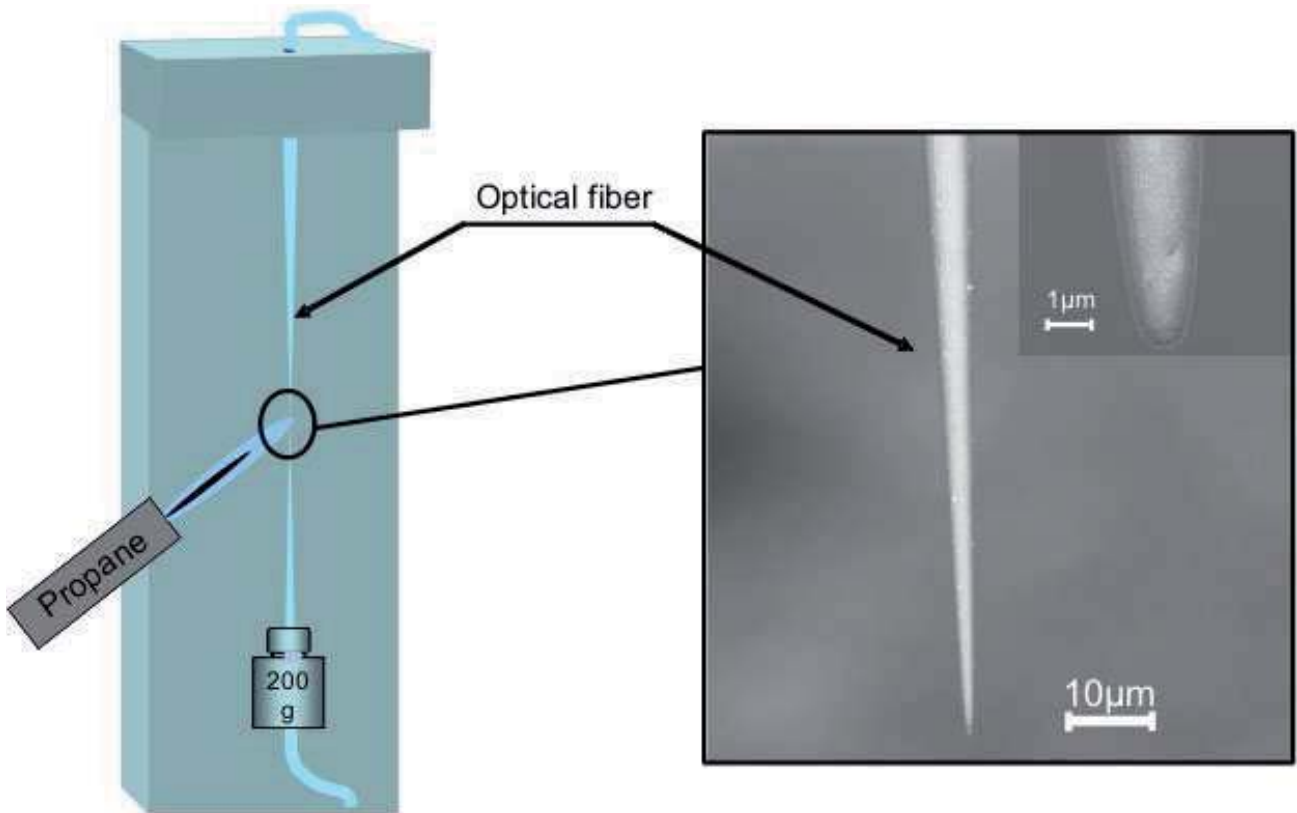
Figure 3.13: Sketch of our home-built fiber puller for tapered fiber tips. Optimum results were obtained with a pulling weight of about 200 g.

penetration depth of AuPd at optical wavelengths a layer thickness of about 100 nm is needed to prevent light leakage out of the fiber.

To get a well defined light source different structures were cut into the fiber by FIB. The FIB preparation was performed in cooperation with Yuliya Stark in the group of professor Dr. Hans Peter Oepen. Using this technique light emitting structures with subwavelength features could be realized as shown in figure 3.14(a). Several hole pairs with distances of some hundred nanometers from each other were cut into the metallization and into the glass of the tapered fiber. Light which is coupled into the fiber gets strayed out of the holes and can be observed by an optical microscope. This nano-light source allows us to perform transmission measurements through rolled-up metal/semiconductor microrolls. Furthermore it is possible to observe the image of the hole structure on the surface of the microroll, so imaging of subwavelength features through the curved superlattice can be investigated.
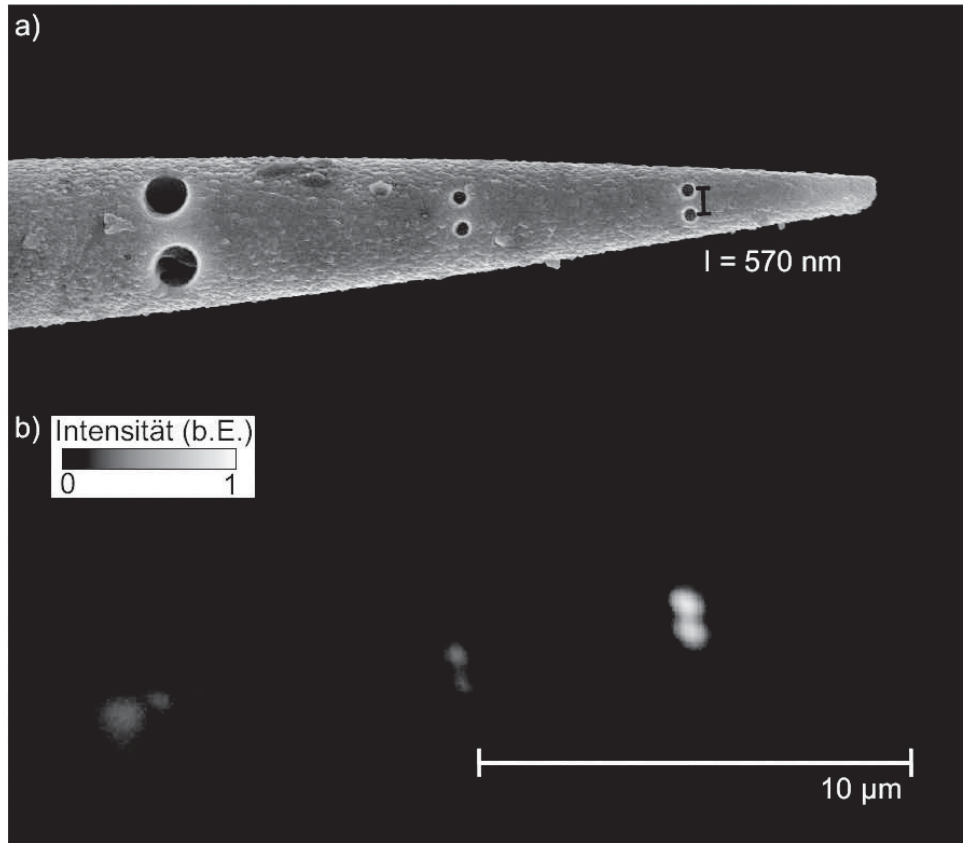
Figure 3.14: (a) SEM image of a metallized fiber tip, which has been structured by FIB. The distance between the two holes on the right side of the fiber is about 570 nm with a hole diameter of 200 nm. (b) Light which is coupled into the fiber gets strayed out at the position of the two holes, resulting in a nano-sized light source.

3.3.2 Microscope setup for transmission and reflection analysis on rolled-up superlattices

To manipulate tapered fibers into microrolls a special microscope/manipulation setup was constructed. The setup is sketched in figure 3.15. The tapered fiber is mounted on a xyz-piezo stack, which can move the fiber in all spatial directions with a resolution of a few nanometers. The position of the fiber is controlled optically by a microscope and a CCD camera. Since both, fiber tip diameter and spatial resolution of the manipulation setup, are much smaller than the diameter of a typical microroll ($\approx 3\,\mu m$) we are able to insert the fiber into the microroll. Figure 3.16(b) shows a micrograph of a tapered fiber, which is approached close to a microroll (upper part). Two point sources can be clearly identified at the tip end of the tapered fiber (red arrow). The lower part of the figure shows the same tapered fiber which has been inserted into the microroll. Both point sources are still clearly visible and the transmitted intensity through the microroll can be measured.
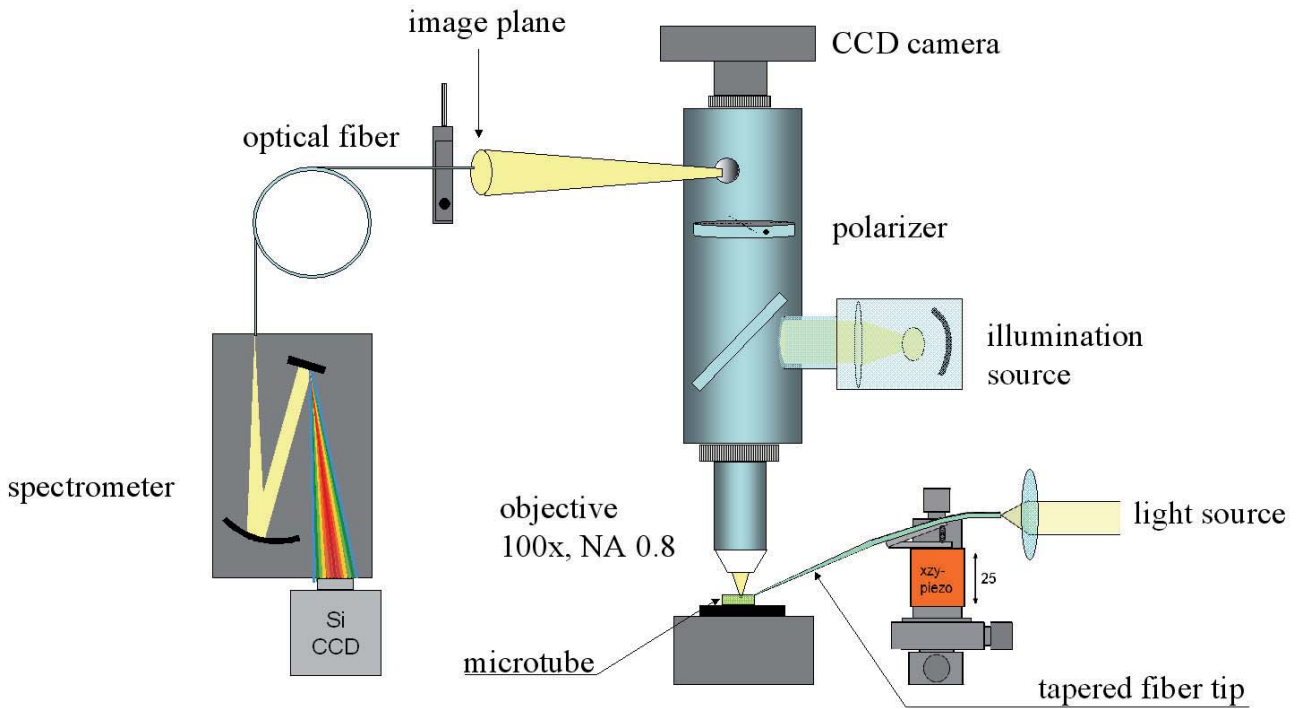
Figure 3.15: Fiber based microscopy setup. The specific elements are explained in the text.

3.3.2.1   Transmission measurements

For transmission measurements light generated by the supercontinuum white-light source *SuperK Versa* from the company *Koheras* is coupled into the fiber. This light source consists of a pulsed pump laser ($\lambda = 800$ nm, pulse duration $\tau_{Pump} = 5$ ps) and a photonic crystal fiber (PCF). The laser pulse, which is coupled into the PCF broadens due to nonlinear effects to a white light spectrum with a wavelength range from 490 nm to 2200 nm [Ran00]. Since the photonic crystal fiber has a diameter of only a few microns the emitted light can be collimated to a parallel beam with a beam divergence of less than 5 mrad. This beam passes through a monochromator consisting of a grating ($75 \frac{1}{mm}$) with a spectral resolution of about 2 nm and a long-pass filter which filters out second order diffractions of the grating.

Afterwards the beam is focused into the tapered fiber by a microscope objective (10x, NA 0.25). Light scattered out at the tip end by the holes drilled by FIB is collected by the microscope objective (100x, NA 0.8) and is transferred to the CCD camera on top of the microscope. The CCD camera is sensitive for visible light up to a wavelength of 1100 nm. The transmission through the microroll is calculated by the ratio of the light scattered out of the fiber tip outside and inside the microroll:

(a)

(b)
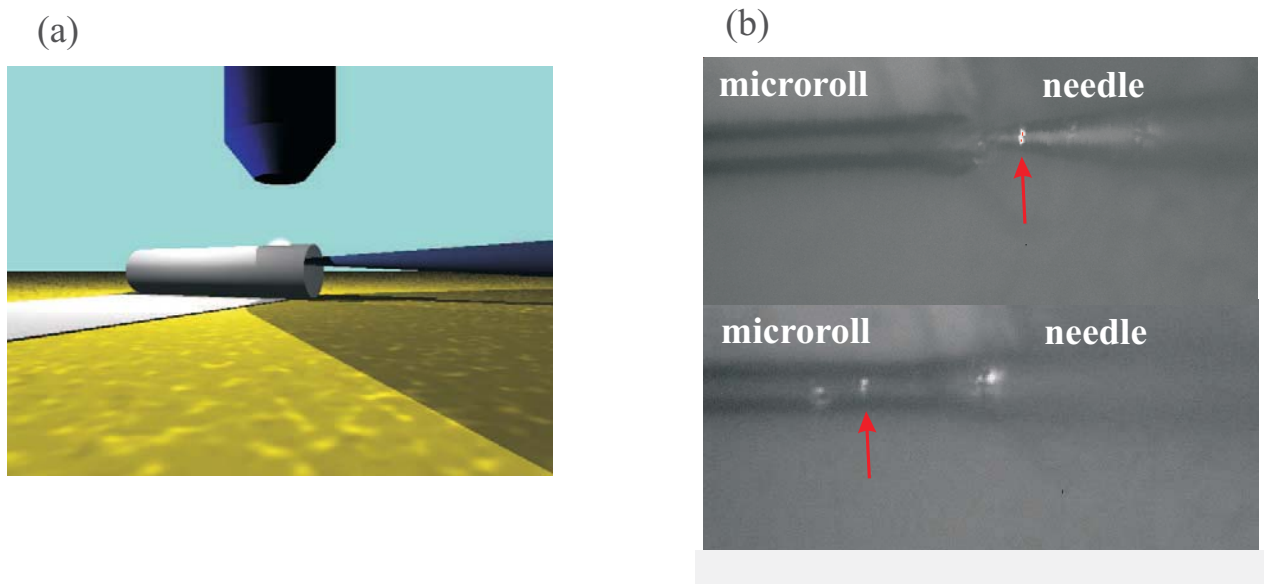
Figure 3.16: (a) Sketch of the setup with a tapered fiber inside the microroll. (b) Micrograph of a tapered fiber directly in front (upper part) and inside a microroll (lower part).

$$T = \frac{I_{outside}}{I_{inside}}$$

The intensities can be measured by a software supplied with the CCD camera, which allows one to integrate over the intensities of all camera pixels within a software defined radial aperture, as shown in figure 3.17. The aperture was set around the image of the hole structure and covered an area of some few microns on the sample. Therefore stray light from different parts of the fiber tip could be filtered out and errors due to slight defocusing could be minimized.

3.3.2.2   Reflectivity measurements

For reflectivity measurements the illumination light source of the microscope was used, which generates a white light spectrum ranging from 500 nm to 950 nm. The light is coupled into the microscope objective by a beam splitter and illuminates the whole sample. The reflected light passes again through the objective, is reflected out of the microscope by an additional beam splitter and passes through a collimation lens. Therefore an additional image plane of the sample is created in front of the microscope. A multimode fiber with a core diameter of 100 μm is positioned within this image plane by a translation stage. Since the microscope objective and the collimation lens magnify the image of the sample about 50 times, only light which is reflected by an area with a diameter of 2 μm on the sample enters the fiber core. The fiber transmits this light to a spectrometer with a
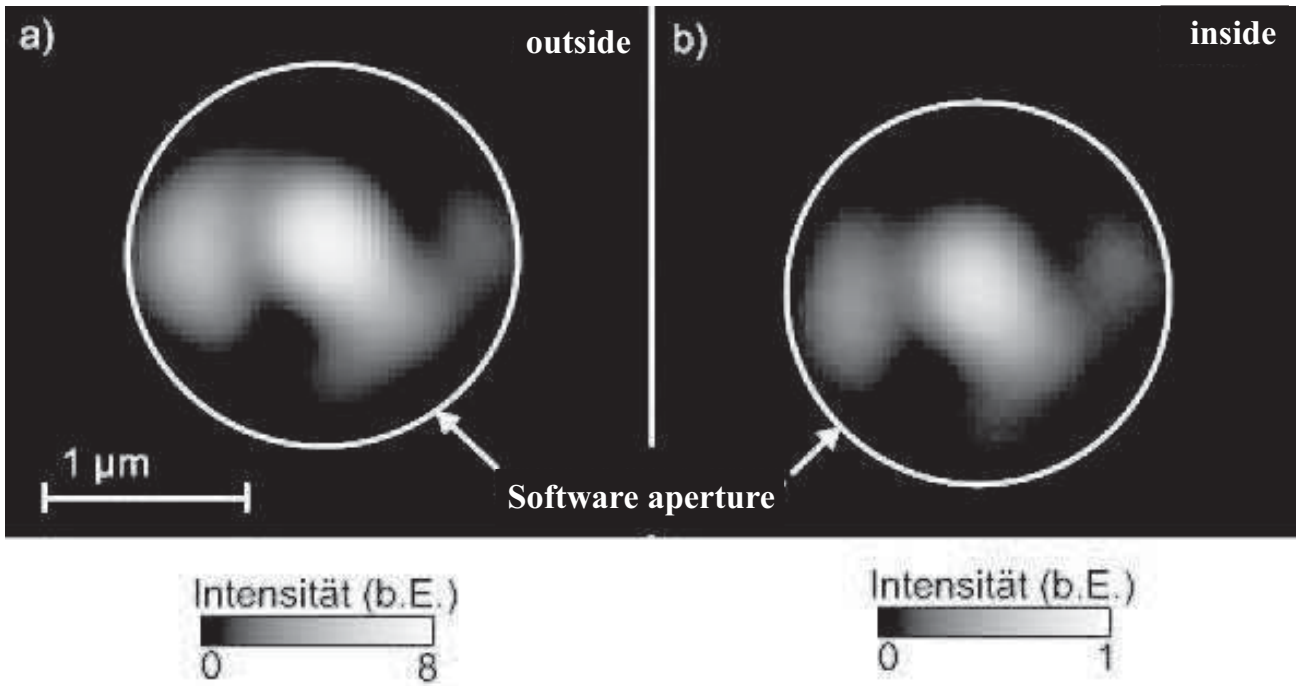
Figure 3.17: Micrographs of the tapered fiber lightsource (a) outside and (b) inside the microroll. The scattered light intensities are calculated by integrating over all pixels inside the software aperture.

back-illuminated CCD detector. Therefore the reflected intensity on the sample can be measured in a single shot with a spatial resolution of about $2\,\mu m$. The reflected intensity of the microroll is normalized to the reflected intensity of a silver mirror yielding the reflectivity:

$$R = \frac{I_{microroll}}{I_{Ag-mirror}}$$

3.3.3 Shifted plasma frequencies of metal/semiconductor superlattices

Transmission and reflection spectra were measured on several rolled-up microrolls consisting of (In)AlGaAs and silver with varying ratios of layer thicknesses. A typical measured spectrum is shown in figure 3.18 for a microroll consisting of 8 rotations of 11 nm thick silver and 20 nm thick (In)GaAlAs layers. In the following discussion we will assume that the light transmits perpendicularly through the microroll wall, i.e. the lateral wavevector $k_{||} = 0$. For such a wavevector only the tangential permittivity component $\epsilon_{||}$ influences the transmission and reflection spectra, while the component ϵ_z is canceled, as can be seen from equations A.5 and A.6. From section 3.1 we expect that the dispersion component $\epsilon_{||}$ is negative below the effective plasma frequency ω_p, which depends on the ratio of metal and dielectric layer thicknesses. This is consistent with

the sharp drop of the transmission and the increase of the reflection curves in figure 3.18 for photon energies below 1.6 eV. For higher energies the effective medium is expected to become transparent and light can propagate through it. In the spectrum the transmission increases for the corresponding energies and Fabry-Pérot resonances appear, i.e. the intensity oscillates sinusoidally with wavelength due to interferences of multiple reflected light beams. Therefore reflection and transmission measurements allow us to prove the validation of the effective medium theory on rolled-up superlattices and to determine their effective plasma frequencies ω_p. As described in section 3.1.1 these frequencies are of special importance for hyperlensing, since ω_p corresponds to the working frequency in the channeling regime.

To estimate the position of ω_p, the theoretically calculated reflection and transmission spectra as well as the dispersion curve for the corresponding permittivities $\epsilon_{||}$ are compared to each other in figure 3.19. In the transmission spectrum on the left side the position of ω_p is approximately at the point where the transmission has dropped to one half of its maximum value:

$$T(\omega_p) = \frac{T_{max}}{2} \tag{3.27}$$

Accordingly, in the reflectivity spectrum ω_p corresponds to the position of the local minimum above the sharp increase of the reflectivity.

To investigate the dependence of ω_p on the metal/dielectric ratio of layer thicknesses, transmission and reflection measurements were performed on different microrolls. In table 3.1 the data of the microrolls, which will be investigated in the following, are listed. The thicknesses of the semiconducting layers are known from the MBE growth, while the thicknesses of the silver layers were measured by atomic force microscopy after their evaporation. The winding number of the microrolls and therefore the total thicknesses of the superlattice was determined by measurements of the roll-up distances of the microrolls as well as by cross-sectional SEM images like the ones in figure 3.12.

Figure 3.20 shows the transmission spectra for the samples listed in table 3.1, which have an (In)AlGaAs thickness of (34 ± 1) nm and varying silver layer thicknesses. These spectra agree well with theoretical curves calculated by a transfer matrix approach (solid curves in figure 3.20(b) and (c)).

The sample $K8$ (orange dots) has only a very thin silver film of less than 1 nm on top of the (In)AlGaAs layer resulting in a thickness of layer ratio of more than $\frac{d_{(In)AlGaAs}}{d_{Ag}} > 33$. Therefore the effective plasma frequency lies far below the visible
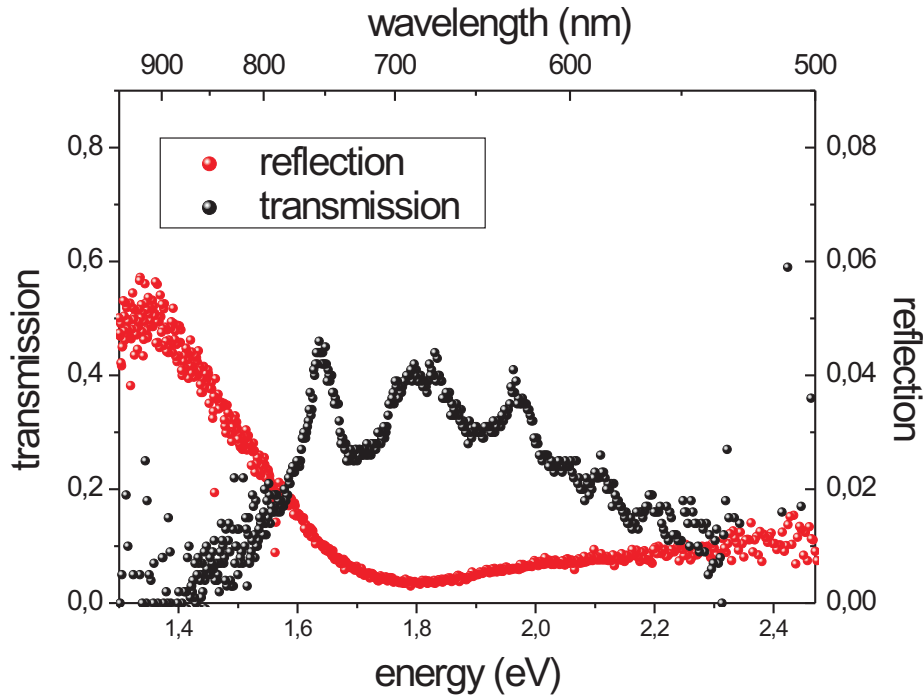
Figure 3.18: Exemplary reflection and transmission spectra of the sample G23.

frequency range and the superlattice behaves like a dielectric. For large frequencies the transmission drops to zero due to the enhanced absorption of (In)AlGaAs. At an energy of $\hbar\omega = 1.85\,\mathrm{eV}$ a maximum due to a Fabry-Pérot resonance would be expected. In the experimental data this maximum is suppressed, probably due to slight thickness variations of the very thin silver film. For thicker silver layers the plasma frequency moves to the visible range. The drop of the transmission can be clearly recognized for all samples and it shifts to higher frequencies for smaller thickness ratios. Again Fabry-Pérot resonances are not as pronounced as expected from theory. The reason for this might be

#	$d_{(In)AlGaAs}$	d_{Ag}	winding number
$\alpha 7$	34 nm	25 nm	5
$\alpha 9$	34 nm	22 nm	6
$\alpha 3$	34 nm	19 nm	4
$K2$	35 nm	16 nm	4
$K8$	34 nm	<1 nm	5
$G23$	20 nm	11 nm	8

Table 3.1: Layer thicknesses and winding numbers of the microrolls investigated during this thesis.
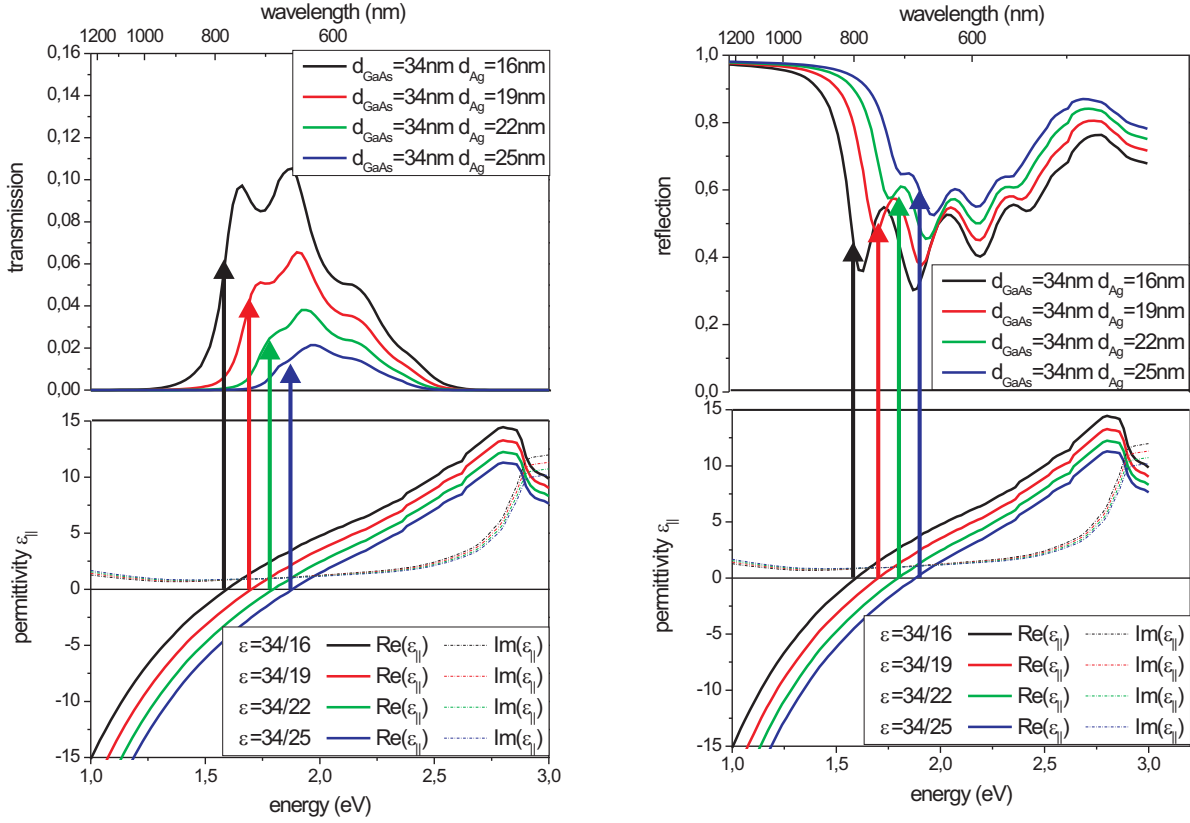
Figure 3.19: Calculated transmission and reflection spectra of superlattices consisting of six rotations of GaAs/silver double layers and the corresponding effective permittivities. While the semiconductor layer thicknesses are kept constant ($34\,\mathrm{nm}$) the thicknesses of the silver layers are varied, thus tuning the position of the effective plasma frequency.

again the surface roughnesses of the silver films. Furthermore our nanosized light source emits light with lateral wavevectors larger than $k_{||} = 0$ and the microscope objective collects wavevectors with lateral components up to $k_{||} = 0.8\,k_0$, where k_0 is the maximum propagating wavevector in vacuum. Therefore the Fabry-Pérot resonances are smeared out further due to different transmission angles through the superlattice. Since we do not know the wavevector distribution of the emitting light source a quantitative analysis is not possible.

Figure 3.20(d) shows the positions of the plasma frequencies versus thicknesses ratio η for the different rolled-up superlattices. The plasma frequencies were estimated from the transmission spectra as described above. For comparison the theoretical plasma frequency for an effective medium is plotted. Both curves show the same qualitative characteristics, i.e. the plasma frequency shifts to larger energies for lower thickness ratios η.

The reflectivities for all samples are shown in figure 3.21. The sample $K8$ with a
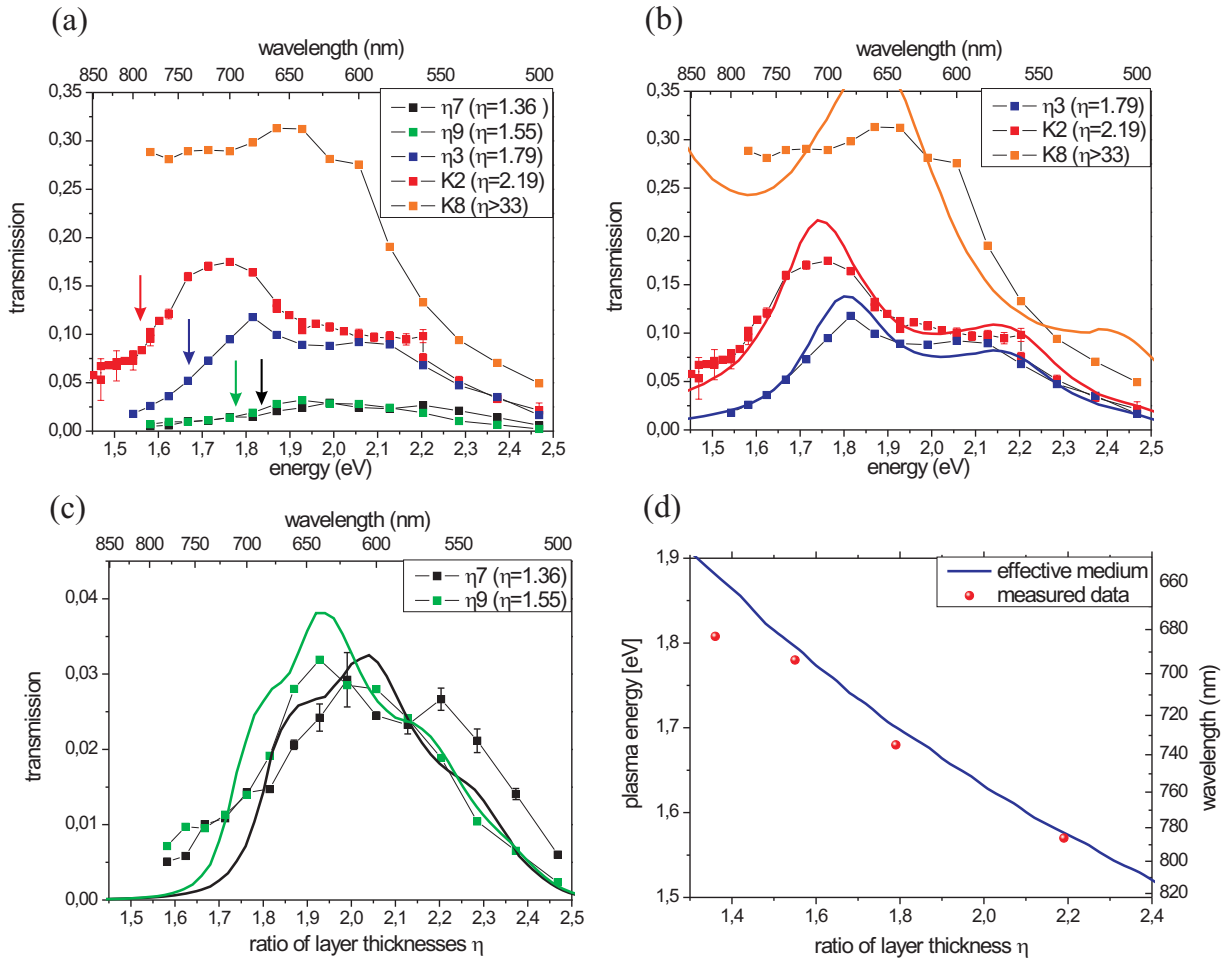
Figure 3.20: (a) Transmission measurements on microrolls with different ratios of layer thicknesses for (In)AlGaAs and silver layers. The dots correspond to measured data points, while the lines are guides to the eye. For these samples the thickness of the (In)AlGaAs was $(34 \pm 1)\,\mathrm{nm}$, while the thicknesses of the silver layers were varied. For a better demonstration two groups of the same samples are shown together ((b), (c)) with the transmission calculated by a transfer matrix approach (solid lines). (d) The plasma frequencies for all samples were estimated from the transmission curves and compared to an effective medium model.

very thin silver film shows only Fabry-Pérot interferences in the reflectivity spectrum, while the reflectivity for samples with finite silver layer thicknesses increases up to one below the plasma frequencies ω_p. For the samples $\alpha3$ ($\eta = 1.79$) and $K2$ ($\eta = 2.19$) the experimental data coincide well with theoretically calculated reflection curves: Above ω_p Fabry-Pérot resonances appear, whose maxima and minima have the same position as in the calculations. For the samples $\alpha7$ ($\eta = 1.36$) and $\alpha9$ ($\eta = 1.55$) there are some deviations between the theoretical and experimental curves, which might be due to additional gaps between successive layers of the microroll. Nevertheless clear Fabry-

Pérot resonances as well as an increase in reflectivity for frequencies smaller than ω_p can be observed. Furthermore the reflectivity curves are shifted with respect to each other for different thickness ratios. The positions of the plasma frequencies are estimated as described in the following: A linear regression line is fitted to the increase of the reflectivity curve below ω_p, while a second regression line is fitted to the increasing reflectivity curve of the first Fabry-Pérot resonance. The intersection of both lines gives the position of the local minimum, which coincides qualitatively with the plasma frequency of an effective medium as described above. These data show, that our rolled-up superlattices can be qualitatively described by an effective medium with a permittivity component $\epsilon_{||}$ and a plasma frequency ω_p. In the following we will discuss how effective parameters can be retrieved from these transmission and reflection curves.
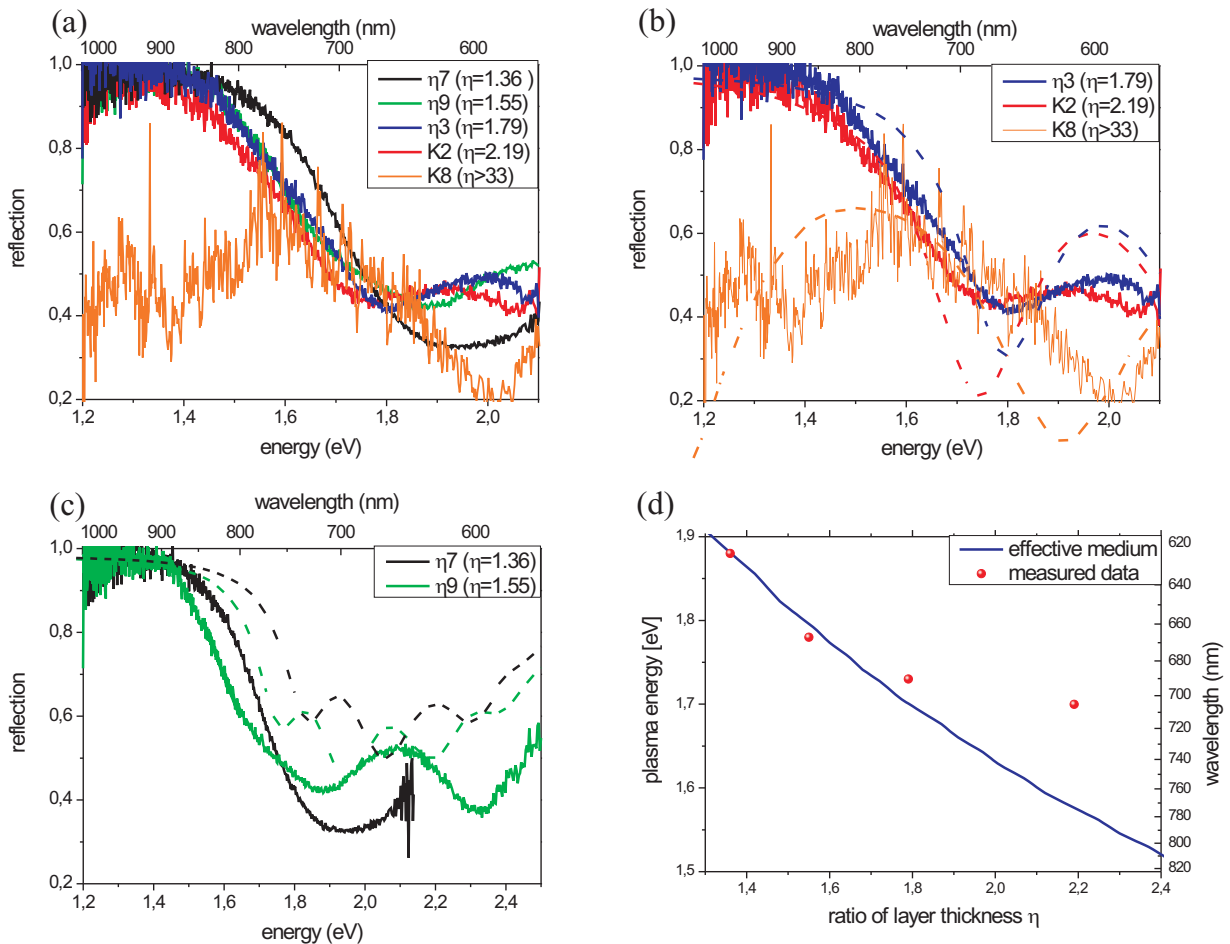
Figure 3.21: (a) Reflection measurements for the microrolls discussed in figure 3.20. For a better demonstration two groups of the same samples are shown together ((b),(c)), with the reflection calculated by a transfer matrix approach (dashed lines). (d) Estimated plasma frequencies are compared to an effective medium model.

3.3.4   Retrieval of optical parameters

As described in chapter 4 the effective optical permittivity and permeability of a metamaterial can be retrieved from its complex reflection and transmission coefficients. In the case of superlattices the permittivity is described by a bianisotropic tensor, so two components $\epsilon_{||}$ and ϵ_z, as well as the isotropic permeability μ (TM polarization) have to be retrieved. In our experiment we assume $k_{||} = 0$, i.e. only $\epsilon_{||}$ influences the transmission and reflection spectra. Furthermore we can assume that the permeability $\mu = 1$ for all frequencies. For different values of μ a coupling between the magnetic field component of the light wave and the metamaterial would be necessary and ring currents would have to be induced inside its metallic structures. However since the metallic layers of the superlattice are extended infinitely in two dimensions their inductivity is equal to zero and no coupling to the magnetic field component of an external field is possible.

In principal the remaining component $\epsilon_{||}$, which consists of a real and an imaginary part, could be retrieved from reflection and transmission curves, i.e. two parameters which are available in our measurements. For this retrieval the metamaterial is assumed to be a slab with a thickness d and an effective isotropic permittivity $\epsilon_{||}^*$. The absolute values of the transmission and reflection coefficients of the slab can be calculated by equations A.5 and A.6. Putting the experimental data into these equations, they can be solved numerically for the real and the imaginary part of $\epsilon_{||}^*$. However we found that such a retrieval is instable with respect to its input parameters and fails for superlattices with layers thicker than a few nanometers. To test the retrieval method reflection and transmission curves of silver/GaAs superlattices have been generated by a transfer matrix calculation. The data for an effective medium as well as for superlattices with finite layer thicknesses are shown in Figure 3.22(a). The total thicknesses of the superlattices as well as their thickness ratios have been kept constant. Especially for frequencies above the effective plasma frequency differences between the superlattices and the effective medium appear: For increasing layer widths the transmission is lowered while the reflection is enhanced. The reason for this is that for thicker layers transmission and reflection of a superlattice are more and more dominated by the air/silver and the GaAs/air interfaces on both ends of the superlattice. Since the absolute values of the permittivities of GaAs and silver are larger than the permittivity of the corresponding effective medium, the transmission is lowered while the reflectivity increases. The enhanced layer reflectivity is also the reason for more pronounced Fabry-Pérot resonances.

Figure 3.22(b) shows the calculated permittivities retrieved from the transmission and reflection curves in (a) with equations A.5 and A.6. As starting points for the numerical calculations of $\epsilon_{||}^*$, the permittivities of an effective medium with the same thickness ratio were set. For very thin layer thicknesses ($d_{Ag} = 1\,\text{nm}$) the retrieved permittivities approach the permittivities of a corresponding effective medium quite well (red dots). This is also true for thicker layers. However at frequencies nearby the effective plasma frequency the curves retrieved for layer thicknesses much larger than $1\,\text{nm}$ are bent down and no physical meaningful solutions can be found for higher frequencies. This is surprising since the corresponding wavelengths of the transmitted light are still much larger than the lattice constants of the superlattices and the effective medium approximation should be fullfilled. Variations of the starting conditions of the numerical approach did not give meaningful results either as investigated in detail by the diploma student Andreas Rottler [Rot10]. We conclude from this that the retrieval fails in the case of superlattices with thick layers and additional information is required.

If we give up the condition $\mu = 1$ and consider additionally to the transmission and reflection data also the phase of the transmitted and reflected light, we can use the retrieval method developed by Smith et al. [Smi05] for inhomogenous metamaterials, which has been already used in section 4 for split ring resonators. To test the retrieval data the complex transmission and reflection coefficients of a superlattice consisting of GaAs and silver layers have been calculated theoretically. Since the phase of the transmission and the reflection coefficients can vary by $\pm 2\pi m$ (m is an integer), there exists an infinite number of mathematical solutions for the retrieved permittivities and the physically meaningful branches have to be chosen. Figure 3.23 shows the retrieved permittivities of superlattices consisting of GaAs and silver layers with varying layer thicknesses. Different colors correspond to different phase factors m, physically meaningful branches are marked by red arrows: For very thin layer thicknesses (figure 3.23(a)) the permeability μ of the superlattice is almost equal to one as expected from the discussion above. For thicker layers the permeability of the same branches deviates from this value. We believe that this is an artefact of the retrieval mechanism, which compensates the effect of the finite layer thicknesses on the transmission and reflection spectra. However, as shown figure 3.23(c) the retrieved permittivities agree well with the effective medium theory (pink dashed line) for thin (black line) and thick layers (red line). Therefore this retrieval can be used to retrieve the effective permittivity of our superlattices and to predict the position of the

(a)

(b)
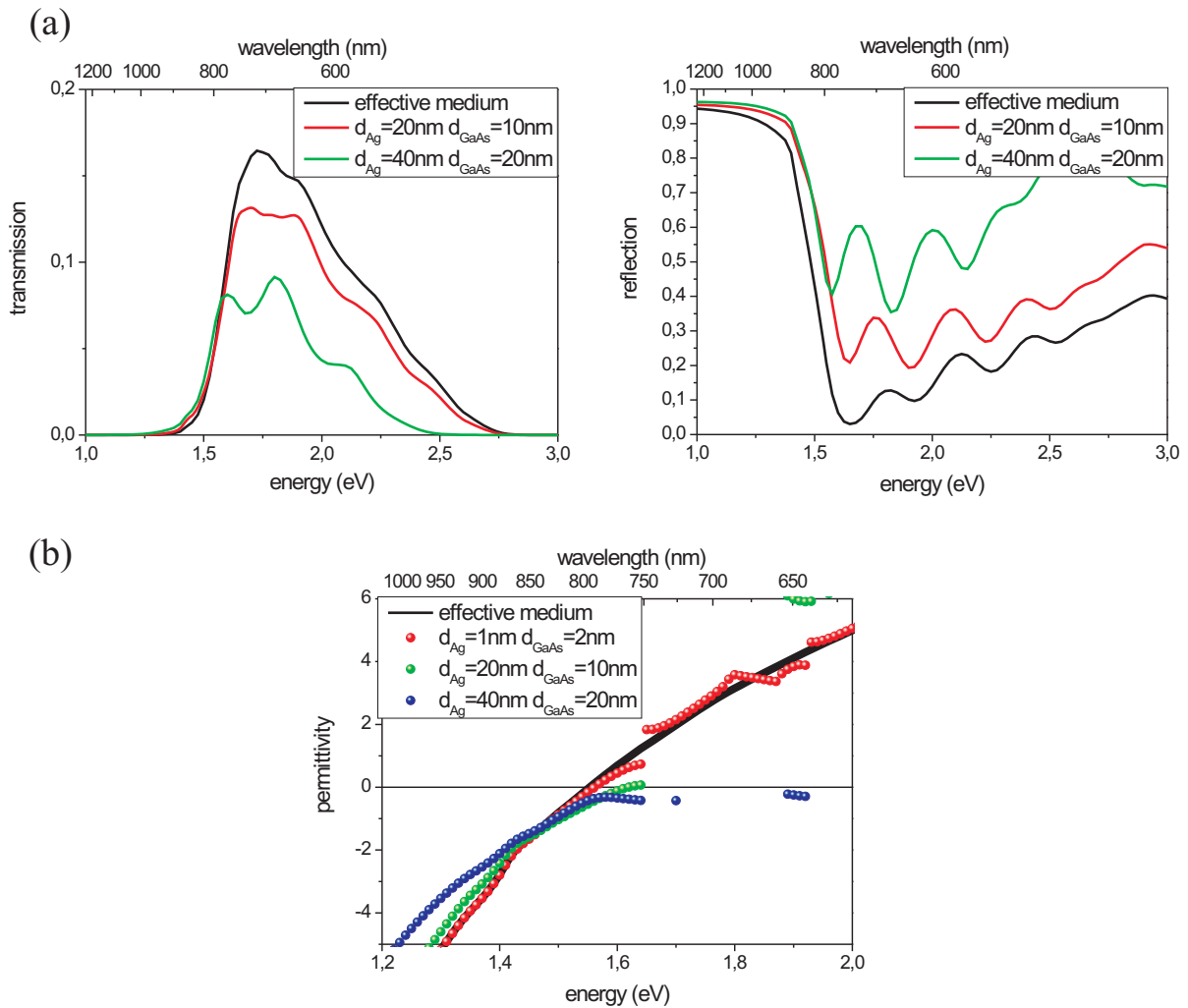
Figure 3.22: (a) Retrieved permittivities $\epsilon_{||}$ for superlattices with $\eta = 2$, but different layer thicknesses. The permittivity was retrieved from transmission and reflection data, which were generated by a transfer matrix calculation. (b) Transmission and reflection curves for the same superlattices.

effective plasma frequency.

Unfortunately we are only able to measure absolute values of the transmission and reflection coefficient. To obtain the phase of the transmitted and reflected light a Michelson interferometer would have to be used, as for example in [Dol06]. To retrieve the permittivities from our experimental data the phases were calculated theoretically and put together with the measured transmission and reflection spectra. Figure 3.24 shows the retrieved permittivities for our samples. The arrows mark the positions of the theoretical plasma frequencies of corresponding effective media. The theoretical plasma frequencies agree well with the retrieved data from the samples $K2$ and $\alpha3$, while for the samples $\alpha9$ and $\alpha7$ some deviations appear. Nevertheless the plasma frequencies of these samples
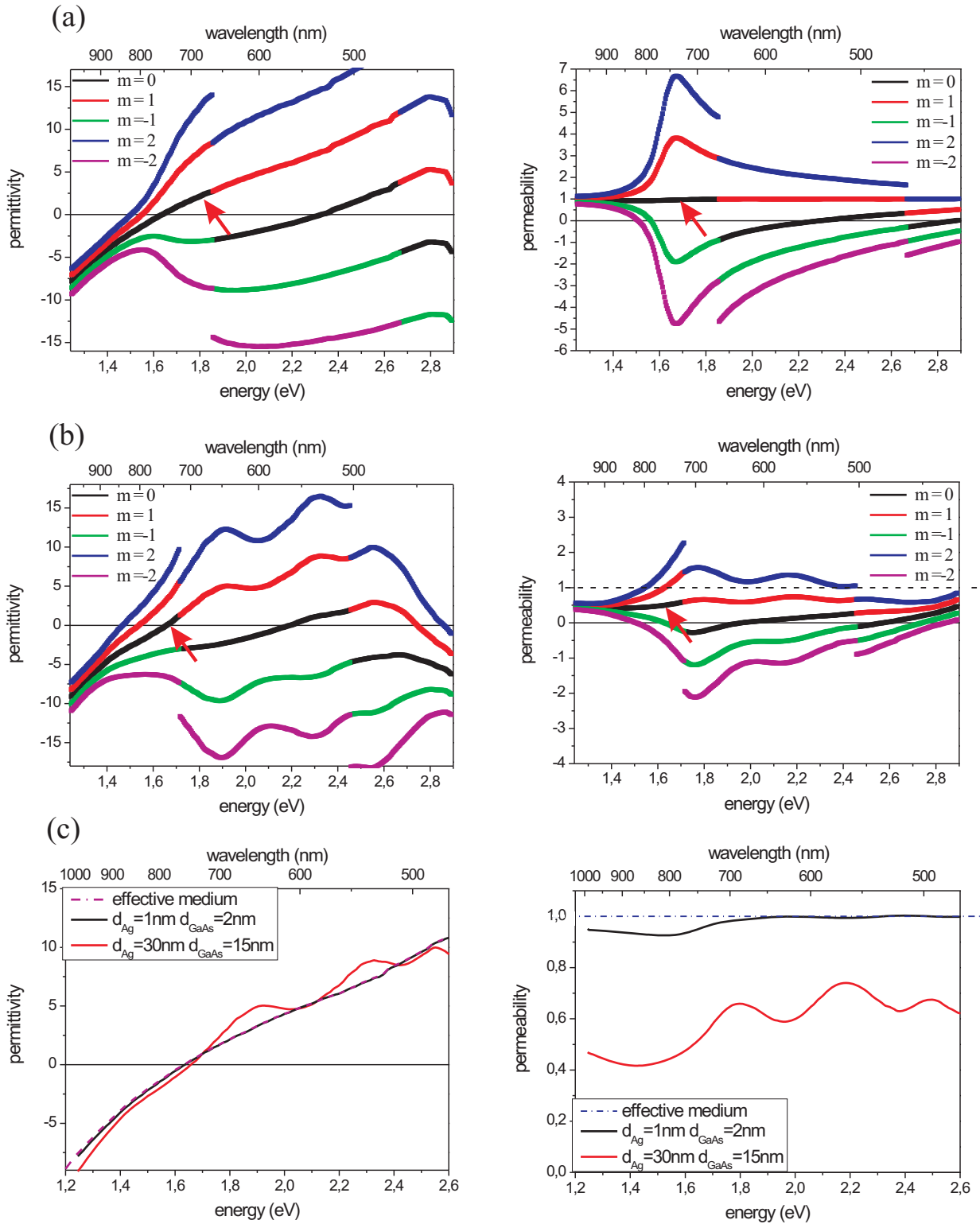
Figure 3.23: Retrieved permittivities and permeabilities for superlattices with (a) $d_{Ag} = 1\,\text{nm}$, $d_{GaAs} = 2\,\text{nm}$ and (b) $d_{Ag} = 15\,\text{nm}$, $d_{GaAs} = 30\,\text{nm}$. The solutions for different phase factors m are plotted in different colors. The correct branches are marked by red arrows. These branches are plotted separately in (c). Even for thick layers an effective $\epsilon_{||}$ can be retrieved, while the effective permeability shows some nonphysical deviations.

are shifted to higher values, due to the lower thickness ratios of (In)AlGaAs and silver in these samples. The permittivity of the sample $K8$ shows no transition to a metallic state and stays positive for all frequencies. As in section 3.3.3 the retrieval indicates that the plasma frequency is shifted by varying the thicknesses ratio of the microrolls in a broad range of the visible and near-infrared regime.

The results of this section can be summarized as follows: On the supposition $\mu = 1$ the retrieval of the effective permittivity $\epsilon_{||}$ from transmission and reflection data fails for layer thicknesses larger than $1/100$ of the wavelength of the transmitted light. For thicker layers changes of the reflectivity and transmission spectra can only be compensated by assuming values of μ different from one. In this case retrieved values for $\epsilon_{||}$ are in good agreement with the effective medium theory, also for layer thicknesses up to $\lambda/10$. However the good agreement is bought dearly by the unphysical solution $\mu \neq 1$. Nevertheless this method can be used to determine the position of ω_p and therefore the working wavelength of the channeling regime, where the microrolls are expected to show hyperlensing with subwavelength resolution.

3.4 Near-field scanning microscopy measurements in cooperation with the University of Bourgogne

As discussed in section 3.1.1 it is possible to use rolled-up metal/semiconductor microrolls as magnifying hyperlenses for wavelengths in the visible and near-infrared regime. The tapered fiber tips, described in section 3.3.1, can be used as light sources with subwavelength spatial features, which are magnified and form an image on the surface of the hyperlens. However the magnifications of hyperlenses prepared so far are too small to observe a clear change of the image by optical microscopy. For example the magnification of the microroll $\alpha9$ with the thickest wall of $330\,\mathrm{nm}$ and an inner radius of $1.5\,\mathrm{\mu m}$ is expected to be $V = \frac{r_{out}}{r_{in}} = 1.22$. This means, that the distance of $570\,nm$ between the two holes inside the metallization of the tapered fiber, shown in figure 3.14, is magnified to a distance of $695\,nm$ on top of the microroll. At a working wavelength of $700\,\mathrm{nm}$ this change in distance is too small to be observed by an optical microscope. A possible way to investigate the image with high spatial resolution is near-field optical scanning microscopy (NSOM) [MAP96]. In cooperation with Dr. Fréderique de Fornel and Dr. Benoit Cluzel at the University of Bourgogne (Dijon) first NSOM measurements were performed on rolled-up metal/semiconductor microrolls. The setup is shown in figure 3.25: Like in our
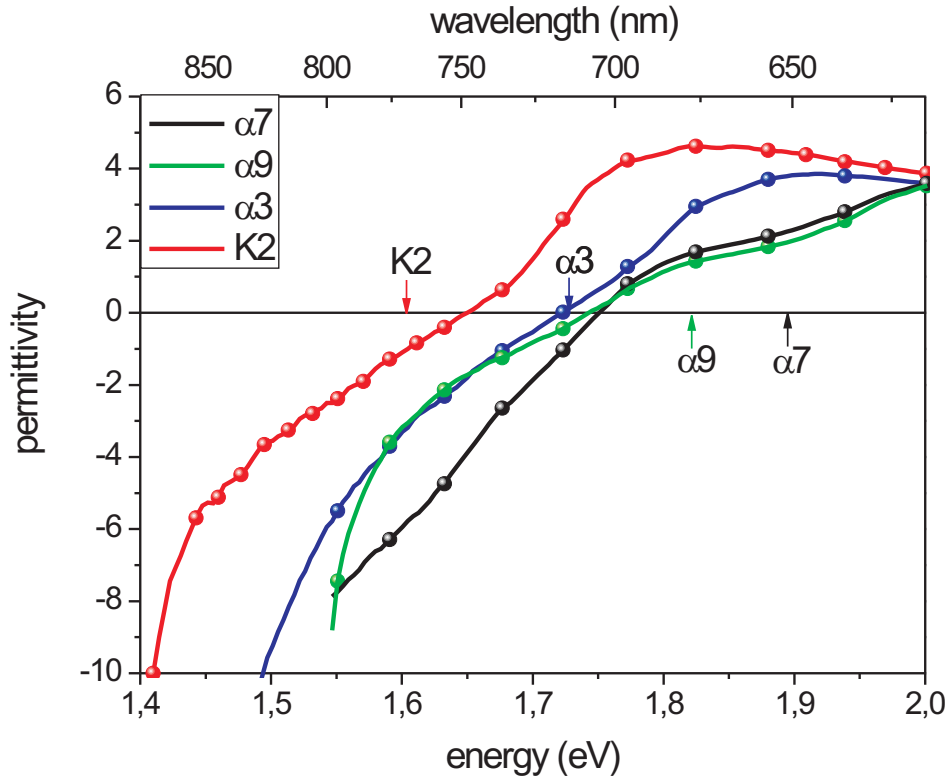
Figure 3.24: Retrieved permittivities for the samples investigated in the previous section. Arrows mark the positions of the plasma frequencies expected from an effective medium theory.

microscope transmission setup a tapered fiber with a hole structure drilled by FIB inside its metallization illuminates a rolled-up microroll from the inside. As a light source the beam of a supercontinuum white-light was coupled into the fiber. Another sharp tapered fiber tip, the so called NSOM probe, with a tip diameter of typically $50 - 200\,\text{nm}$, is brought into close proximity to the microroll. The fiber is scanned by two piezos in x and y direction parallel to the plane of the sample, while the height h above the sample was kept constant by a so called shear-force feedback loop. For this purpose the NSOM probe is excited resonantly by a tube piezo (dither piezo) to perform small oscillations with an amplitude of about $1\,\text{nm}$ parallel to the sample surface. The resonance frequency of the NSOM probe changes due to forces between the probe and the sample surface and therefore depends on the sample-probe distance. The change of the resonance frequency feed back is used to control the distance between the NSOM probe and the sample. The error feedback signal supplies a topographical image of the sample, as in atomic force microscopy. This topographical image can be overlayed with the corresponding optical signal. Further details about the setup can be found in [Fab08].

In our measurements the NSOM was performed in so called collection mode: The light emitted from the tapered fiber is collected by the NSOM probe and is transmitted to a spectrometer and a photomultiplier. By scanning the NSOM probe in two dimensions at constant height above the sample an image of the field distribution of the scattered light can be obtained. Thereby not only the far field but also the near field is coupled into the NSOM probe and transferred to the detector.
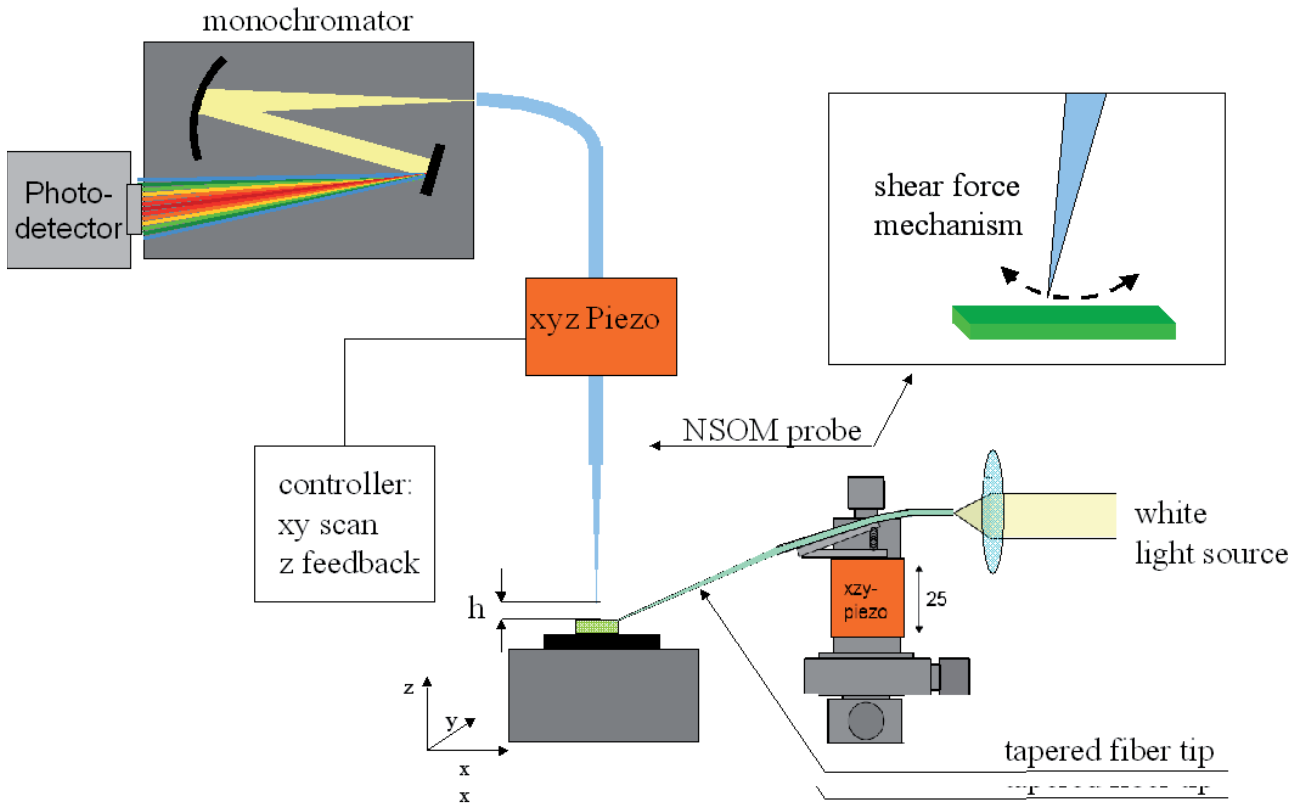
Figure 3.25: Sketch of the NSOM setup used in cooperation with the University of Bourgogne on rolled-up metal/semiconductor microrolls. The inset illustrates the principle of the shear force mode, explained in the text.

In the experiment scans on top of the tapered fiber tip as well as on top of the microroll $G23$ (compare table 3.1) were performed. As shown in figure 3.18 of the preceding section, this microroll has a plasma wavelength at about $800\,\text{nm}$, where the transmission drops sharply and the reflection increases. Nearby this wavelength at $\lambda = 725\,\text{nm}$ NSOM images above the tapered fiber and above the microroll were performed. A SEM image of the tapered fiber is shown on the left side of figure 3.26(a). The FIB drilled structure inside the tapered fiber consists of two hole pairs which are seperated by $4\,\mu\text{m}$ from each other.

The holes at the tip end have a distance of 600 nm from each other. On the right side of the figure the corresponding optical NSOM image of the tapered fiber is shown. At the position of the two holes a strong field intensity is measured. The image of the two holes is blurred, due to influences of the tapered fiber tip, which will be discussed in detail at the end of this section. The cross-section through the image, shown in figure 3.26(c) shows some sharp peaks which can be allocated to the hole structure. Furthermore NSOM scans on top of the microroll have been performed (figure 3.26(b)). On the left side a topographical image of the microroll is shown, which helps to determine the position of the tapered fiber inside the microroll. Clearly the silver layer can be separated from the (In)AlGaAs layers. The two figures in the middle and on the right side of figure 3.26(b) show NSOM scans of the tapered fiber field profile which is transmitted through the microroll. The scans were performed at two different heights above the microroll. In the figure in the middle the NSOM probe had a distance of only a few nanometers from the sample, while the probe was lifted to a distance of about 700 nm at the right figure. At this distance we would expect that all near field components of the hole structure image have vanished. Cross-sections along the lines of the field profiles in figure 3.26(a) and (b) are compared with each other in (c). The field profile on top of the microroll resembles the profile above the needle, while there is a clear broadening in the far field above the microroll. This is a first indication that near field components of the hole structure inside the tapered fiber have been transmitted through the microroll. Unfortunately the resolution of the NSOM probe seems to be not good enough to resolve a clear subwavelength image. The reason for this is that the NSOM probe was not coated by a metal and therefore no subwavelength aperture on the NSOM probe was defined. This kind of probes is used for experiments where the fields are bound to the surface of the sample, like for microresonators. Unfortunately a large part of the light emitted from our tapered fiber is propagating to the far field, thus leading to artefacts in the NSOM image, since propagating waves are able to couple into the fiber from a broad spatial region. To testify our first results either NSOM probes with a subwavelength aperture inside a metallisation, or light sources which emit only evanescent waves have to be used. Based on the experience we gained during our cooperation further experiments at the University of Hamburg are planned. The experiments will be performed with a commercial NSOM microscope (Attocube), which has just been delivered to our lab.
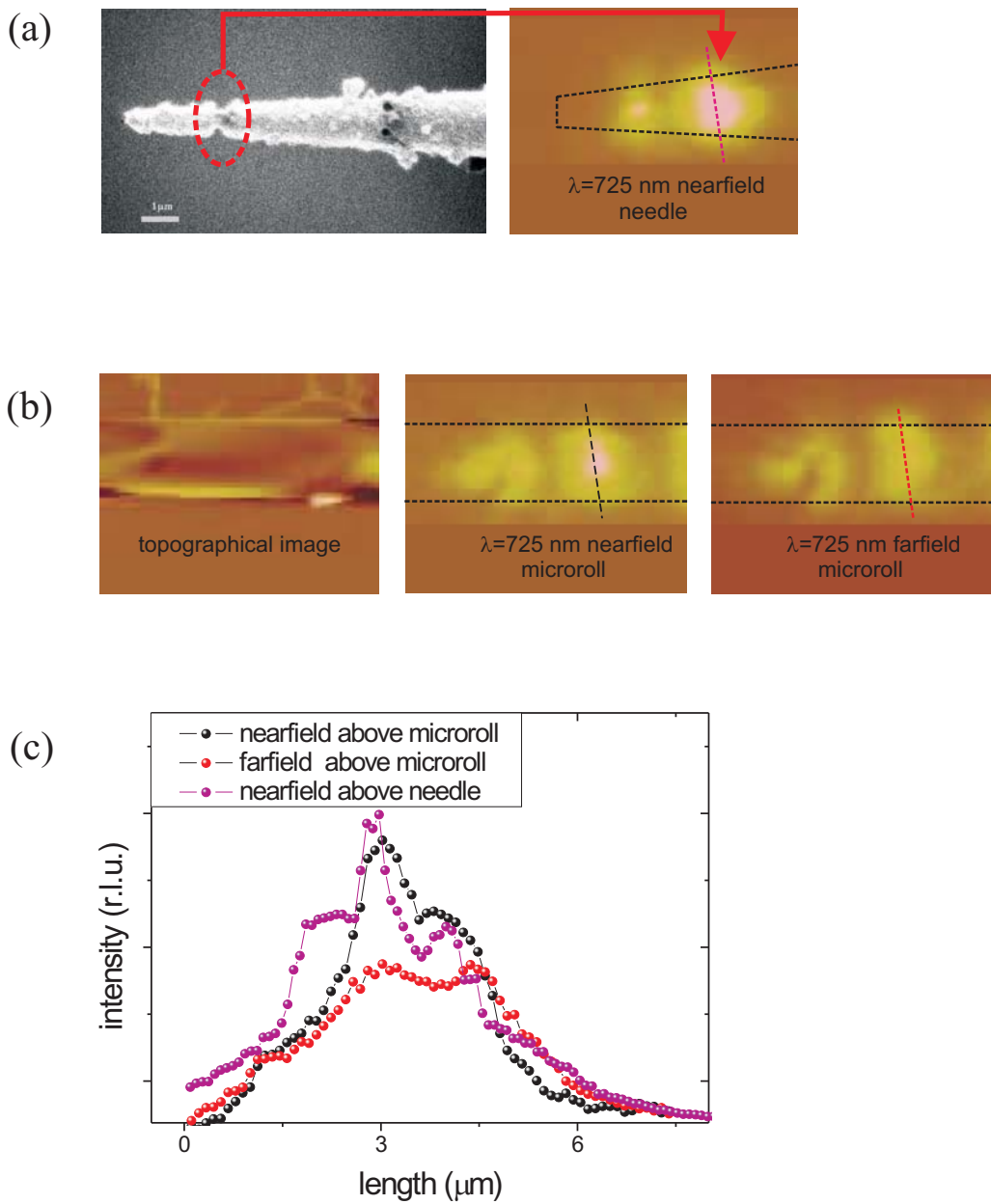
Figure 3.26: (a) Scanning-electron micrograph of the tapered fiber used in the experiment at the University of Bourgogne. On the right side the corresponding NSOM image is shown. Dashed black lines mark the shape of the tapered fiber. (b) Topographical NSOM image of the microroll (left image) and the field profiles directly above (middle image) and in a distance of 700 nm (right image) above the microroll. (c) The cross-sections of the fields along the lines shown in the images of (a) and (b). While sharp features can be observed in the near field of the tapered fiber and of the microroll, the image is broadened in the far field of the microroll.

CHAPTER 4

METAMATERIALS MADE OF
INAS/METAL
MICROROLL ARRAYS

While in the preceding chapter metamaterials were defined by the subsequent layers inside the wall of a rolled-up microroll, it will be shown in this chapter how metamaterials can be realized by arrays of microrolls. It is expected from analytical calculations that these arrays exhibit a negative permeability μ for frequencies in the far infrared. To justify the analytical calculations and for a deeper understandig of more complex structures numerical calculations have been performed in the framework of the diploma thesis of Nils Gerken [Ger08] with a three-dimensional solver of Maxwell's equations (CST Microwave Studio). Several aspects how the resonance frequency can be tuned will be discussed.

4.1 Negative permeabilities for microroll arrays

The permeability of all materials known so far in nature is equal to one for frequencies well above the gigahertz regime, i.e. there is no coupling of the material with the magnetic field of an electromagnetic wave. John Pendry proposed in the year 1999 that such a coupling could be realized by artificial metamaterials made of arrays of so called split-ring resonators [Pen99]. Figure 4.1 shows the concept of a conventional split-ring resonator. Each split-ring consists of a single metal winding, which forms an inductance L, and a gap between the metal layer, which exhibits a capacitance C. In a simple model the split-ring can be described as a LC circuit that gets resonantly excited at the resonance frequency $\omega_0 = 1/\sqrt{LC}$ by the magnetic field component of the electromagnetic field irradiating the split-ring. This way ring currents are induced inside the metal winding, which lead to a magnetic field inside the split-ring opposite to the external field. If the lattice constant of an array of splitrings is much smaller than the wavelength of the exciting light the permeability of such an effective medium can be described by a Lorenz lineshape:

$$\mu = 1 - \frac{F\omega^2}{\omega^2 + i\frac{R}{L}\omega - \omega_0^2} \tag{4.1}$$

where $F = \frac{V_{lattice}}{V_{splitring}}$ is the fraction of the unitcell and the splitring volume and R is the resistance of the metal winding. As shown in figure 4.1(c) the permeability μ becomes negative for frequencies between $f_0 = \omega_0/2\pi$ and f_1. The positions of the frequencies f_0 and f_1 can be tuned by the geometrical dimensions of the split-ring array. During the last years split-ring resonators with resonance frequencies from the microwave- to the near-infrared regime have been realized [Smi00, Liu08].

We propose to fabricate metamaterials with negative permeabilities by arrays of rolled-up microrolls. The concept is shown in figure 4.3(a). A double layer of strained (In)GaAs and metal is rolled-up one time, so that the metal layer overlaps on top of the microroll, separated by the insulating (In)GaAs. A capacitance is formed which is proportional to the overlap area of the metal layers:

$$C = \epsilon_0\epsilon\frac{A_{overlap}}{d_{InGaAs}} \tag{4.2}$$

The inductivity can be approximately calculated by the inductivity of a ring coil with a single winding:

$$L = \mu_0\frac{\pi r^2}{l_{microroll}} \tag{4.3}$$

Using the commercial three-dimensional Maxwell's equations solver CST microwave studio the transmission and reflection coefficient through a microroll array could be determined. In the simulation setup sketched in figure 4.2(b) the microroll consisting of GaAs and gold is illuminated by a plane wave (which is defined by so called Floquet ports in the software), whose magnetic field component points into the direction of the microroll axis. An array of microrolls was simulated by applying periodic boundary conditions to the lateral directions of the simulation volume. Figure 4.2(c) shows transmission and reflection curves for an array of microrolls with diameters of about $1\,\mu\text{m}$, gold/InGaAs thicknesses $d_{Au} = d_{InGaAs} = 10\,\text{nm}$ and a winding number of $n = 1.05$. In the transmission spectrum a small dip appears at a frequency of about $3.3\,\text{THz}$, which lies in the far-infrared regime. At the same position there is a small peak in the reflection spectrum. Furthermore the phases ϕ_i of the transmitted and reflected plane waves can be calculated. From these

(a) (b) (c)
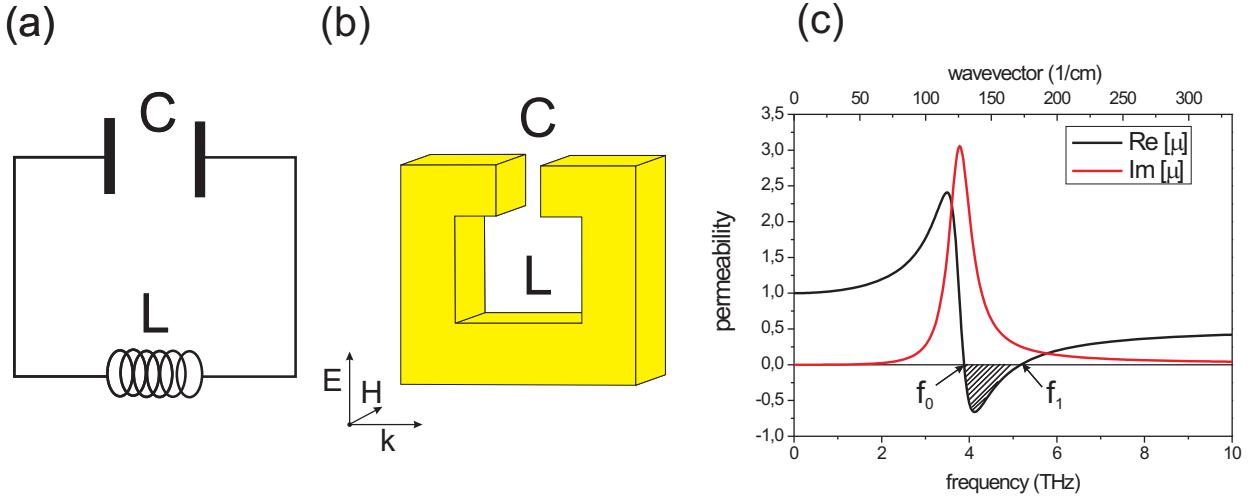
Figure 4.1: (a) Circuit diagram for the splitring resonator shown in (b). A magnetic field, which is oriented perpendicular to the splitring, induces ring currents which lead to an inductance L. The capacitance C is formed by the small gap between the metal winding on top of the ring. (c) Real and imaginary part of the effective permeability μ for an array of split-ring resonators. Between the resonance frequency f_0 and the frequency f_1 the permeability becomes negative.

parameters an effective refractive index n and an impedance Z can be retrieved for the microroll array [Smi05]:

$$n = \pm \frac{1}{kd} cos^{-1}\left(\frac{1}{2t}\left(1 - r^2 + t^2\right)\right) + \frac{2\pi m}{kd}, \quad m = \pm 1, \pm 2, \pm 3 \ldots \tag{4.4}$$

$$Z = \sqrt{\frac{(1+r)^2 - t^2}{(1-r)^2 - t^2}} \tag{4.5}$$

where $k = 2\pi/\lambda$ is the wavenumber of the light wave, d is the thickness of the effective medium, r and t are the complex reflection and transmission coefficients. In the simulation integer multiples of 2π of the phases ϕ_i do not change the complex transmission and reflection coefficients. Therefore also multiple solutions for the refractive index exist corresponding to integer multiples of $\frac{2\pi}{kd}$ added to the right side of equation 4.4. Since the microroll array is quasi two dimensional with a thickness much smaller than the wavelength of the transmitted light, the correct solution for the refractive index is always $m = 0$. The sign of the refractive index is determined by the condition $Im[n] > 0$, since the microrolls do not contain elements, which exhibit optical gain. From the refractive index the permittivity and the permeability can be calculated:

$$\epsilon \;\; = \;\; \frac{n}{Z} \tag{4.6}$$

$$\mu \;\; = \;\; nZ \tag{4.7}$$

The retrieved permeability for the microroll array is shown in figure 4.2(d). At the frequency, where the two resonances appear in the transmission and reflection spectrum the permeability shows a resonant behavior and becomes negative.

To confirm this calculation the field distributions at the resonance frequency ω_R were calculated. As expected from the LC circuit theory currents are induced by the external magnetic field inside the gold layer (4.3(b)), and an electrical field builds up at the position where the metal layers overlap (4.3(c)). This leads to a magnetic field inside the microroll which is in antiphase with respect to the external magnetic field (4.3(d)). If the lattice constant of the microroll array is much smaller than the wavelength of light, the total field response of the array can be obtained by averaging over the fields of the single microrolls, thus leading to an effective permittivity smaller than zero.

4.2 Preparation of microroll arrays

The microroll preparation described in chapter 2 utilizes a strained InGaAs/GaAs bilayer as a rolling template for the metal layer. An alternative approach for the preparation of hybride metal/semiconductor rolls with small diameters was presented in [Sch05]. The GaAs layer is replaced by specific metals with high melting temperatures like chromium, which are evaporated on top of the $In_xGa_{1-x}As$ layer. It has been found [Tho89] that due to the differences of the melting temperature of chromium ($T_{chromium} = 1900°C$) and the GaAs substrate ($T_{GaAs} = 1200°C$) tensile strain, which supports the rolling up process, is induced in the chromium. This method allows the fabrication of large arrays of metal/semiconductor microrolls with diameters of less than $1\,\mu m$. The preparation steps are shown in figure 4.4: On top of a few nanometer thick $In_{0.3}Ga_{0.7}As$ layer, small rectangular arrays of chromium are evaporated. The chromium rectangles have to be aligned along the $< 110 >$ crystal axis, since microrolls roll up preferably along this direction [Gru03, Men05]. The length of the rectangles, which defines the rolling distance, was chosen in such a way, that the microrolls roll up only one time. Around the chromium rectangles a U-shaped mesa is etched deeply into the AlAs sacrificial layer by reactive ion etching (RIE) (etching parameters are listed in appendix B2). After removing the AlAs sacrificial layer by diluted hydrofluoric acid (5%) the microrolls rolled up. The samples were dried by a critical point dryer to minimize surface tensions by the
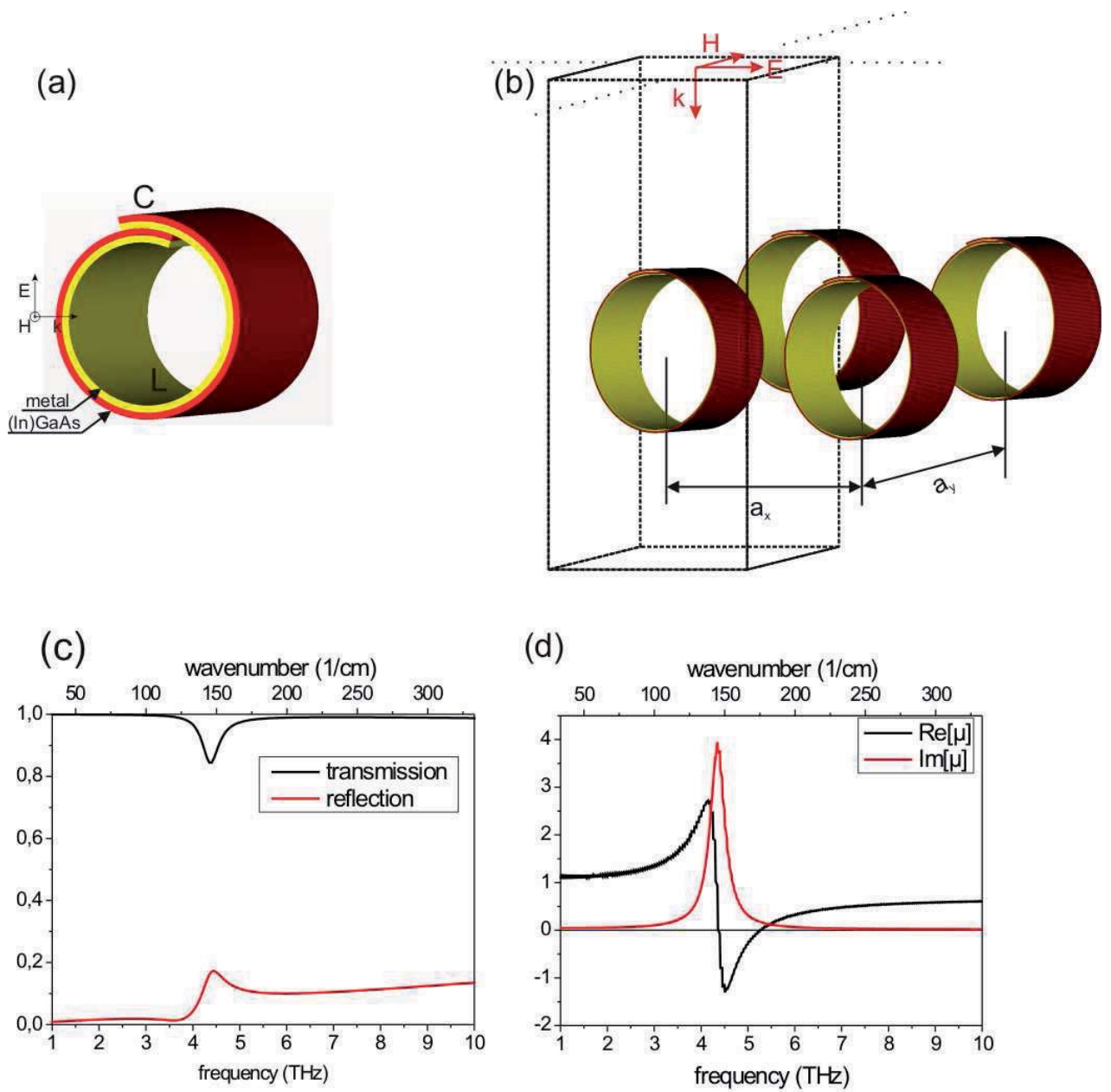
Figure 4.2: (a) Sketch of a microroll consisting of (In)GaAs and a metal. (b) Setup for all simulations in this chapter which were performed with CST Microwave Studio. The simulation volume is defined by the dashed line box. Along the x and y direction periodic boundary conditions were applied, while there is an open boundary in z direction. On top of the simulation volume a plane wave (Floquet port) is excited, which transmits at an angle of zero incidence through the structure. The H field of the plane wave points into the direction of the tube axis. The complex reflection and transmission coefficients were calculated by a frequency domain solver integrated in the software. (c) Reflection and transmission curves through an array of microrolls with the parameters $d_{Au} = d_{GaAs} = 10\,\text{nm}$, $r = 500\,\text{nm}$, $l = 500\,\text{nm}$, $a_x = a_y = 2\,\text{µm}$ and a winding number of $n = 1.05$. (d) Retrieved permeability for the same microroll array.

evaporating liquid. Figure 4.4(c) shows a scanning electron micrograph of a typical array of microrolls. The microrolls contain a 15 nm thick chromium layer and have diameters of about 1 µm. Overall 2500 microrolls were rolled up on the sample with a yield of almost one hundred percent.

Transmission experiments with a far-infrared Fourier spectrometer were performed in cooperation with Kevin Rachor at our institute. The setup is sketched in figure 4.5(a): Light emitted from a mercury lamp enters a Michelson interferometer and is split into two beams by a beamsplitter (BS). One beam is reflected by a fixed mirror (M1), the other one by a mirror (M2) which moves periodically along the light path. Depending on the distance Δx the two reflected beams are time delayed with respect to each other. The superimposed beams are guided by a waveguide into a helium-bath cryostat. At the end of the waveguide the beam passes a polarizer and the sample, which is rotatable with
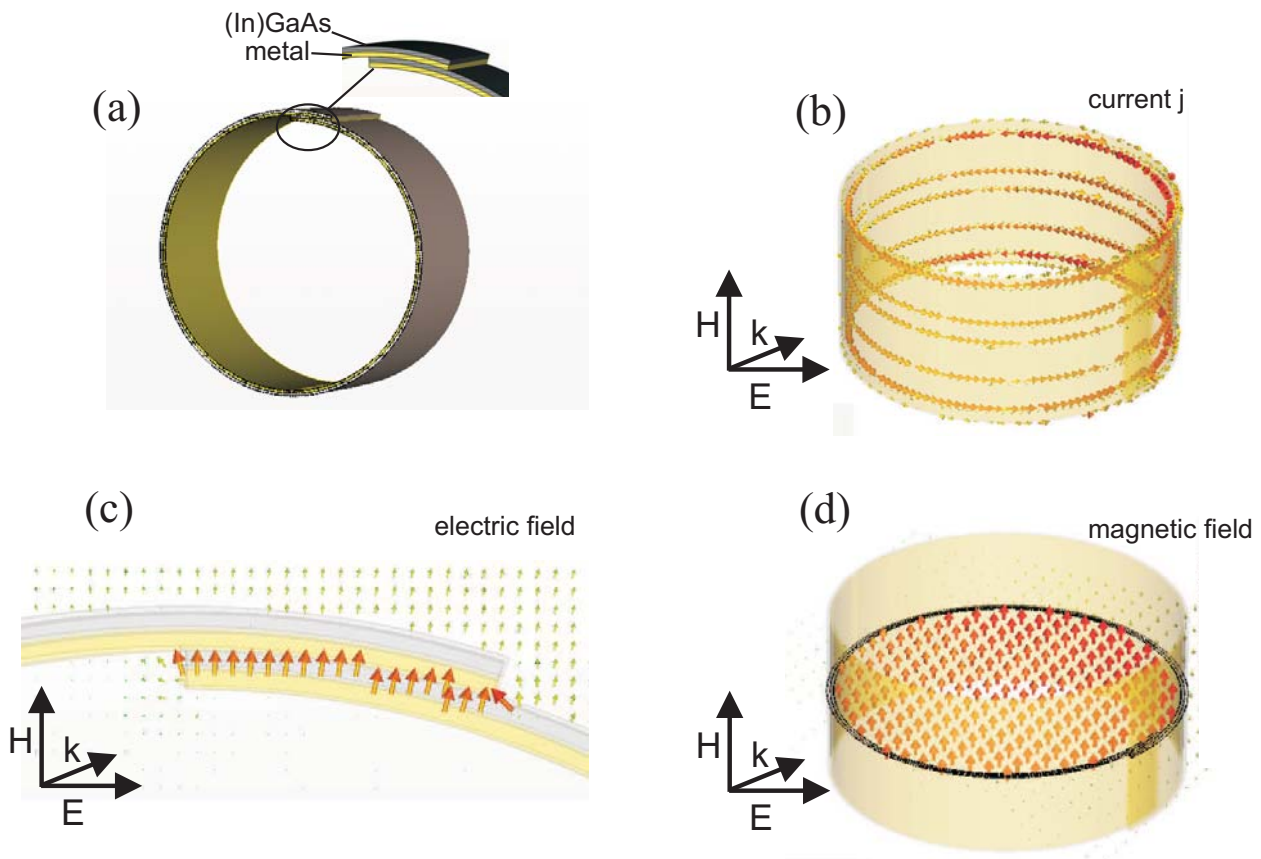
Figure 4.3: Simulated field and current distributions inside the microroll of figure 4.2 at the resonance frequency ω_R. (a) Sketch of the simulated structure. (b) Surface currents inside the metal layer of the microroll, which are induced by the external magnetic field H. (c) In the overlap region of the metal layers an electrical field is formed. (d) The magnetic field inside the microroll is opposite to the external field, thus leading to a negative permeability μ.
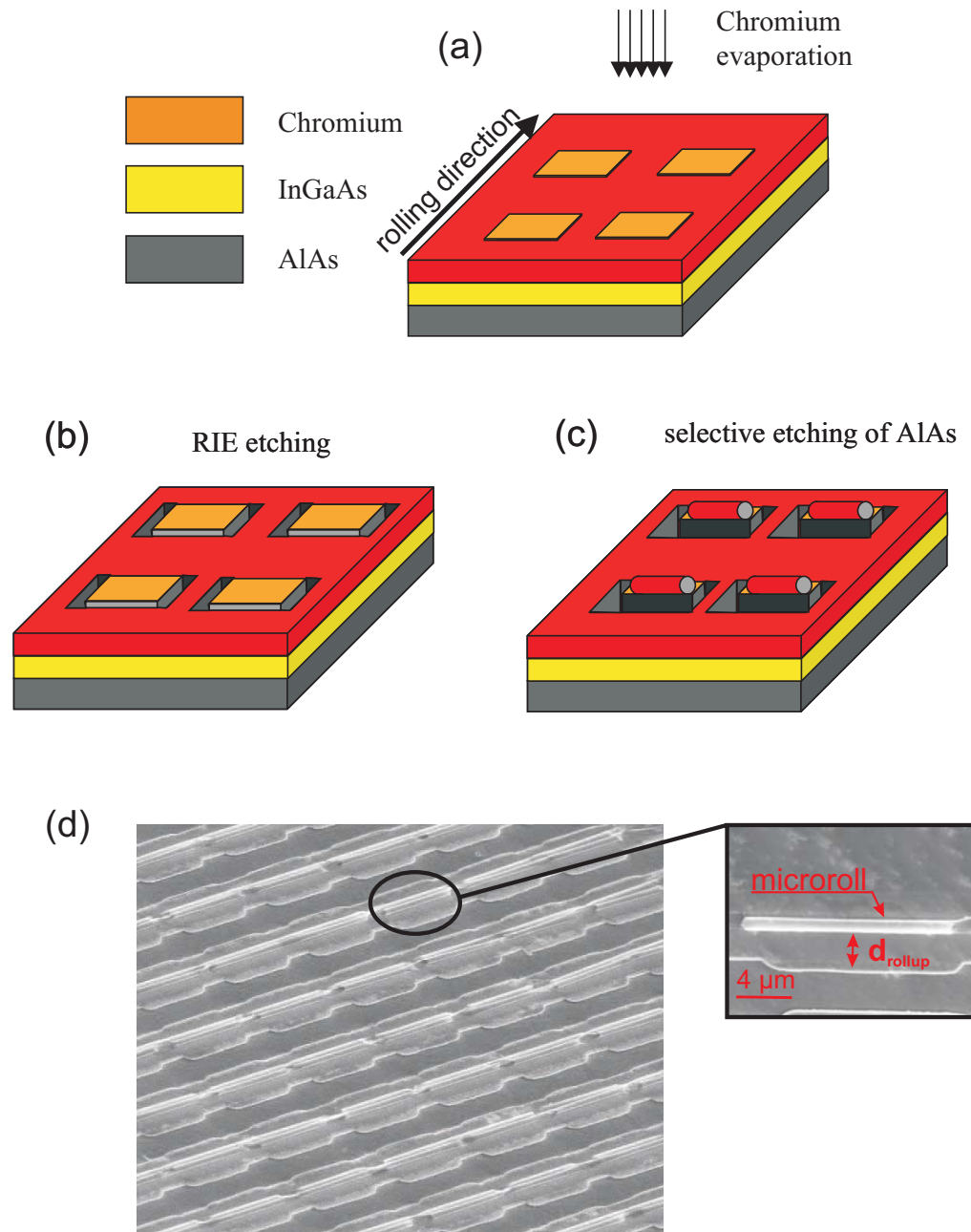
Figure 4.4: (a)-(c) Preparation steps for arrays of rolled-up microrolls. (d) Scanning electron micrograph of an array of rolled-up microrolls. The array consists of several thousand microrolls including 15 nm thick chromium layers, which are rolled one time. The lateral lattice constant of the squared microroll array is 15 x15 μm.

respect to the polarizer. The transmitted light is detected by a bolometer in dependence of the delay distance Δx. By Fourier transformation of this interferogram a frequency dependent spectrum is obtained. Further details about the spectrometer can be found in [Rac09].

Figure 4.5(b) shows the experimental transmission spectrum through the microroll array described in figure 4.4(d). Since we expect the resonance to be polarization dependent, the transmitted intensity for the microroll axis parallel (TM) to the magnetic field component was normalized to the intensity with the microroll axis perpendicular (TE) to the magnetic field component of the transmitted light. The measurements were performed with different beamsplitter configurations, since the choice of the beamsplitter as well as its velocity influence the transmission spectrum. In the figure an exemplary curve is plotted. The transmission is about one for the frequency range from 1.5 THz to 7.3 THz. The frequency range between 7.3 THz and 9.5 THz (grey shaded) have to be excluded from our considerations since the transmitted intensities for both polarizations drop to almost zero due to interaction of light with longitudinal phonons inside of the GaAs substrate (reststrahlen band). Therefore no normalisation can be performed in this regime. Above the reststrahlen band two resonances (marked by arrows) appear at the
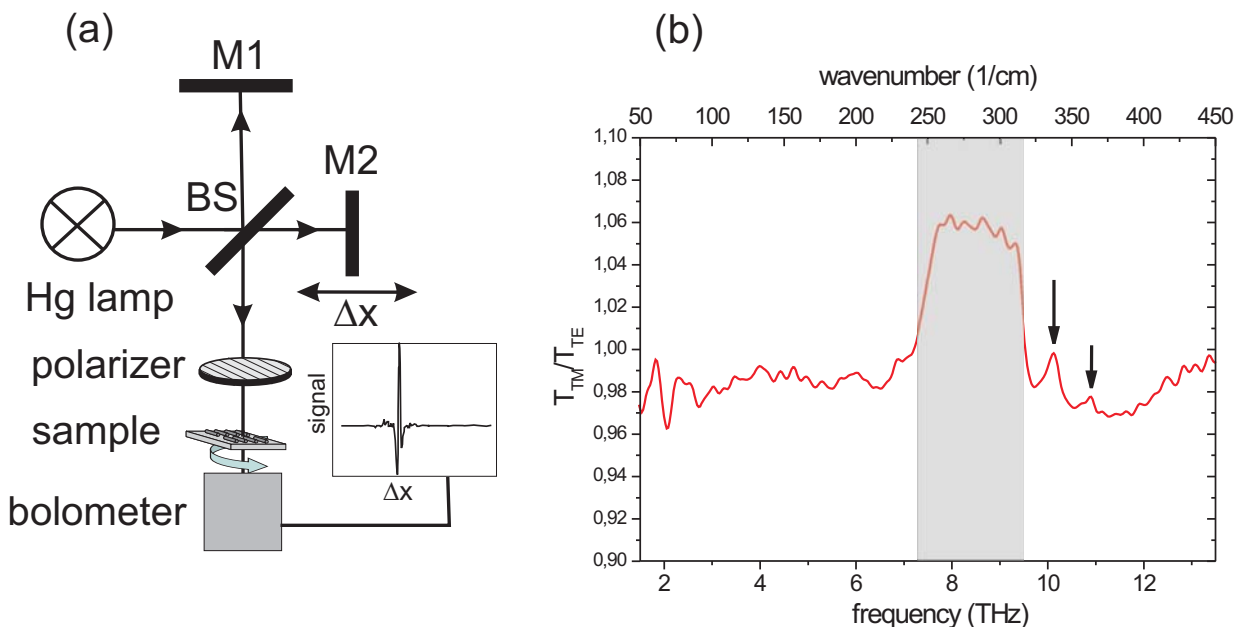
Figure 4.5: (a) Sketch of the transmission setup. Details of the setup are explained in the text. (b) Experimental transmission through a microroll array. Two peaks appear slightly above the reststrahlen band (grey shaded). The peak position does not depend on the experimental configuration.

frequencies 10.1 THz and 10.9 THz, respectively. The positions of the resonances do not depend on the beamsplitter configuration, so they can be assigned to the interaction of light with the sample. The magnetic resonance of the microroll, calculated in figure 4.2, lies in the same frequency range as the observed peaks. However from the simulation we would expect a dip in the transmission spectrum instead of a peak. Furthermore the peaks are very weak with respect to the signal-to-noise ratio of our measurements, so further measurements with optimized samples have to be performed to investigate our preliminary results further. A possible reason for the weakness of the magnetic resonance in the experiment is the difficulty to control the overlap region of the metal layers on top of the microroll. As shown in figure 4.6 already small changes in the overlap area of the metal result in a change of the capacitance and therefore of the resonance frequency ω_R. A possible route to circumvent this problem is to insert an additional, well defined slit into the microrolls, for example by electron-beam lithography. The overall capacitance is formed by a series circuit of the slit capacitance and the capacitance of the overlap region:

$$C_{total} = \left(\frac{1}{C_{Slit}} + \frac{1}{C_{Overlap}} \right)^{-1} \tag{4.8}$$

Since $C_{Slit} \ll C_{Overlap}$ small deviations of the overlap region do not influence the position of ω_R. Figure 4.6(b) shows the simulated transmission spectrum through a microroll with an additional 180 nm wide slit inside the gold layer. As expected the resonance frequency depends only weakly on the microroll overlap. Due to the smaller capacitance of the slit
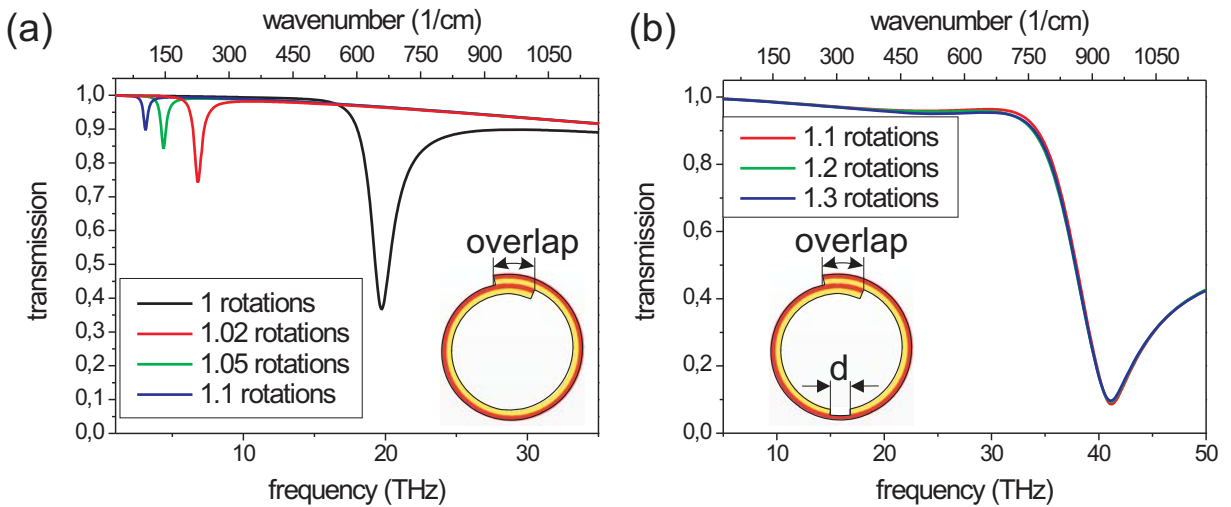
Figure 4.6: (a) Simulated reflection spectrum for slightly varying rotation numbers, which lead to different overlap regions of the metal. (b) Simulated reflection spectra for an array of microrolls with an additional slit of $d = 200$ nm (red curve) and without a slit.

the resonance frequency is shifted to higher values. However the incorporation of slits into the preparation of large microroll arrays turned out to be very difficult, so further optimizations have to be performed in the future to prepare such structures.

CHAPTER 5

SUMMARY AND OUTLOOK

5.1 Summary

In this work the realization of metamaterials by rolled-up metal/semiconductor micro-rolls has been investigated both theoretically and experimentally. We distinguish between metamaterials composed of arrays of metal/semiconductor microrolls and metamaterials defined by alternating metal and semiconductor layers inside the wall of a single microroll.

We showed in chapter 3 that the optical properties of the latter type of metamaterial can be described in an effective medium approximation by an highly anisotropic permittivity tensor. The anisotropy leads to an anomalous wavevector dispersion, which governs the field propagation through the superlattice. While large wavevectors decrease exponentially in free space, the upper boundary for wavevectors propagating through the superlattice is only limited by the layer thickness of the superlattice and absorption inside the layers for specific frequencies. A special case appears in the so called channeling regime, where the lateral permitivity components $\epsilon_{x,y}$ become zero, while the component ϵ_z perpendicular to the layers is large. In this frequency regime all wavevectors propagate in a beamlike fashion through the effective medium and an image with subwavelength resolution is formed on the surface of the superlattice. It was further shown by finite difference time domain (FDTD) simulations that for cylindrical superlattices the image is not only transferred through the superlattice but also magnified. The magnification depends on the ratio of the inner and the outer radius of the cylindrical superlattice. Therefore cylindrical superlattices work as so called hyperlenses in the channeling regime, i.e. they allow microscopy with subwavelength resolution.

In the experimental part it was described how such curved superlattices can be prepared by rolling up a strained metal/AlGaAs/InGaAlAs multilayer into a microroll with several rotations. This method yields high quality radial metal/semiconductor super-lattices with a high control over layer thicknesses. To investigate light transmission

through the walls of the microrolls a nanosized light source was prepared by drilling nanostructures inside the metallization of a tapered fiber with focused ion beam. A microscope setup, developed in the framework of this thesis, allowed us to manipulate the fiber inside the microroll and to perform transmission and reflection measurements. The measurements showed that in good agreement with transfer matrix calculations, the permittivity of the superlattice has a metallic dispersion with a characteristic plasma frequency ω_p. At this plasma frequency the permittivity components $\epsilon_{x,y}$ are zero, so we expect channeling through the superlattice as described above. By changing the ratio of metal and semiconductor layer thicknesses the frequency ω_p, and therefore the working frequency of the hyperlens, could be tuned in a broad range.

So far the magnification of our experimentally realized microrolls is too small to observe an image with subwavelength resolution with an optical microscope. Microrolls with a higher winding number and therefore a higher ratio of inner and outer radii are required for a larger magnification. To investigate the image resolution of our current microrolls near-field scanning microscopy (NSOM) was performed in cooperation with the University of Bourgogne. Although an image of the nanosize structure could be measured on the surface of the microroll the optical resolution of the microscope in Bourgogne was too low to observe clear subwavelength features.

Metamaterials consisting of microroll arrays have been investigated by numerical simulations in chapter 4. These simulations have shown that arrays of gold/InGaAs microrolls with one winding exhibit a negative permeability μ at wavelengths in the far infrared. The Lorenz like dispersion of the permeability could be described approximately by modelling the microroll as a LC circuit, whereby the inductivity L is formed by the metal winding and the capacitance C by the overlap of the two metal layers separated by the InGaAs. The coupling of the microroll array to the external magnetic field can be attributed to ring currents, which are excited resonantly inside the metal windings. Simulation and visualization of the induced currents and fields inside the microroll confirmed this model. The resonance frequency, where the permeability becomes negative, can be tuned by varying the diameter of the microrolls and the overlap region of the metal layers. Since this frequency depends strongly on the geometry of each single microroll, arrays of microrolls with a high homogeneity are required for sharp resonances. Furthermore microroll arrays with dimensions of several square millimeters and a high microroll density had to be prepared to achieve a sufficient signal-to-noise ratio for measurements in the

far infrared. By optimizing preparation parameters large arrays with several thousand chromium/InGaAs microrolls could be realized. However transmission measurements could not validate the simulated results so far, probably due to inhomogenities of the winding number of the rolled-up microrolls. As a possible improvement the insertion of additional slits inside the metal layers has been discussed. These slits form a well defined capacitance in series with the capacitance of the overlap area. If the capacitance of the slits is much smaller than the capacitance of the overlap the resonance frequency depends less on the hardly controllable winding overlap and sharper resonances would be expected.

5.2   Outlook

Rolled-up microrolls offer many perspectives for the realization of novel types of metamaterials. A major drawback of all metamaterials reported so far in the literature is the high amount of absorption, which stems from material losses as well as from strong dispersion of the effective optical constants. This absorption prevents the implementation of metamaterials into practical applications. For example the resolution of hyperlenses is strongly reduced due to absorption as shown in chapter 3. The absorption could be decreased by adding a material with optical gain to the lossy metal, as proposed in [AR03]. Rolled-up metal/semiconductor microrolls offer the unique possibility to combine high gain semiconducting quantum structures with metals into three-dimensional metamaterials. The quantum structures, e.g. AlGaAs quantum wells or quantum dots, are integrated into the strained semiconducting bilayer and are rolled-up together with the metal layer. Optical or electrical pumping of the quantum structure leads to stimulated emission, which partly compensates the losses inside the metal layers. First transfer matrix calculations, which were performed for superlattices consisting of AlGaAs quantum wells and silver layers have shown that the transmission through the superlattice could be increased considerably. For these calculations the permittivity of the quantum well was approached by a Lorenz-oscillator model with a negative imaginary part of the permittivity at its bandgap energy.

Furthermore three-dimensional metamaterials can be realized by patterning rolled-up structures afterwards with focused ion beam. The example structure, shown in figure 5.1(a), consists of an array of rectangular holes, which are "drilled" through the wall of a microroll consisting of six rotations of metal and semiconducting layers. It is known from the literature that these so called fishnet structures exhibit a negative refractive index

in the near infrared [Dol06]. We could show by numerical calculations performed with CST Microwave Studio (figure 5.1(b)) that this is also true for our rolled-up structures. However due to the complexity of these structures further progress in the preparation of metal/semiconductor microrolls has to be made to achieve a higher yield of compactly rolled-up three-dimensional superlattices.
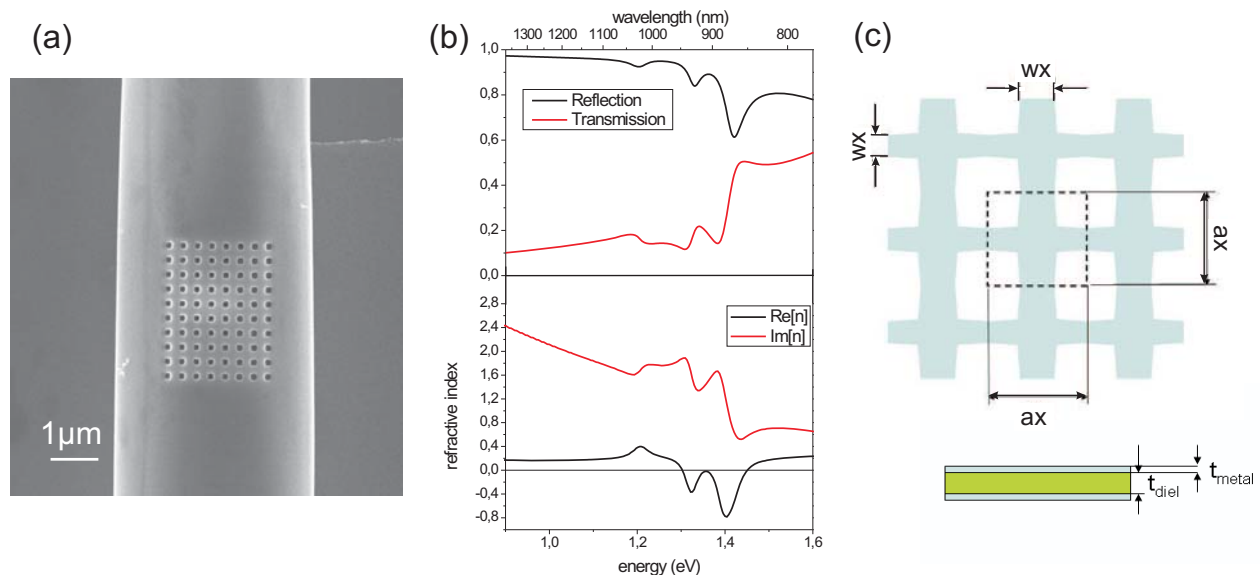
Figure 5.1: (a) Fishnet structure drilled inside a metal/semiconductor microroll (in cooperation with Daniel Stickler from the group of professor Dr. Hans Peter Oepen). (b) Simulated transmission and reflection as well as retrieved refractive indices for a fishnet structure consisting of rectangular holes inside six layers of a silver/GaAs superlattice. The parameters of the fishnet structure are defined in (c): $a_x = a_y = 300\,\mathrm{nm}$, $w_x = 102\,\mathrm{nm}$, $w_y = 68\,\mathrm{nm}$, $t_{Ag} = t_{GaAs} = 17\,\mathrm{nm}$.

Appendix A

A.1 Transfer matrix for metal/dielectric superlattices

In the following the reflection and transmission coefficients through a multilayer consisting of single layers i with permittivities ϵ_i and permeabilities μ_i will be calculated using a transfer matrix approach. We assume that the magnetic field $\vec{H}$ inside each single layer can be expressed by a superposition of plane waves which travel in positive and negative z directions and have a vector component k_x in x-direction:

$$\vec{H}_i(\vec{k}, \omega) = \vec{H}_i^+ e^{i(k_x x + k_z z - \omega t)} + \vec{H}_i^- e^{i(k_x x - k_z z - \omega t)}$$

For the following calculations we assume p polarization of the fields, i.e. $\vec{H} = H_{0i} \begin{pmatrix} 0 \\ 1 \\ 0 \end{pmatrix}$ Th electrical and the magnetic field of a plane wave are connected with each other by the Maxwell equation:

$$i\omega \vec{E} = \vec{k} \times \vec{H}$$

At the boundary between two layers the parallel components of the magnetic field H and the electrical field $\vec{D} = \epsilon \vec{E}$ have to be continuous. This leads to a set of two equations:

$$H_{0i}^+ + H_{0i}^- = H_{0i+1}^+ + H_{0i+1}^-$$
$$-\frac{k_{zi}}{\epsilon_i}(H_{0i}^+ + H_{0i}^-) = -\frac{k_{zi+1}}{\epsilon_{i+1}}(H_{0i+1}^+ + H_{0i+1}^-)$$

These equations can be written in in matrix form:

$$\begin{pmatrix} H_{0i}^+ \\ H_{0i}^- \end{pmatrix} = T_{ik} \begin{pmatrix} H_{0i+1}^+ \\ H_{0i+1}^- \end{pmatrix}$$

The transfer matrix

$$T_{ik} = \begin{pmatrix} 1 + \frac{\epsilon_i k_{zk}}{\epsilon_k k_{zi}} & 1 - \frac{\epsilon_i k_{zk}}{\epsilon_k k_{zi}} \\ 1 - \frac{\epsilon_i k_{zk}}{\epsilon_k k_{zi}} & 1 + \frac{\epsilon_i k_{zk}}{\epsilon_k k_{zi}} \end{pmatrix}$$

connects the magnetic fields on the border of the layers i and k. For s-polarization the transfer matrix reads:

$$T_{ik} = \begin{pmatrix} 1 + \frac{k_{zk}}{k_{zi}} & 1 - \frac{k_{zk}}{k_{zi}} \\ 1 - \frac{k_{zk}}{k_{zi}} & 1 + \frac{k_{zk}}{k_{zi}} \end{pmatrix}$$

Fields on the left and on the right side of a single layer of thickness d_i are connected to each other by a phase matrix:

$$P_i = \begin{pmatrix} \exp(ik_{zi}d_i) & 0 \\ 0 & \exp(-ik_{zi}d_i) \end{pmatrix}$$

With the help of these matrices the propagation of fields through a multilayer can be easily calculated by multiplying the single transfer and phase matrices for each layer with each other:

$$\begin{pmatrix} H_{00}^+ \\ H_{00}^- \end{pmatrix} = T_{01}P_1 \cdot ... \cdot P_{n-1}T_{n-1\,n} \begin{pmatrix} H_{0n}^+ \\ H_{0n}^- \end{pmatrix} = M \begin{pmatrix} H_{0n}^+ \\ H_{0n}^- \end{pmatrix}$$

Since the space after the last layer is infinetely open no light gets reflected and the field H_n^- can be set to zero, while the field H_n^+ can be arbitrarely set to 1. The reflectivity is defined by the absolute ratio of the incoming and the reflected fields in front of the first layer:

$$R = \left| \frac{H_{00}^-}{H_{00}^+} \right|^2 = \left| \frac{m_{11}}{m_{21}} \right|^2$$

The transmission through the layer is defined by the ratio of the incoming intensity and the intensity after the last layer:

$$T = \left| \frac{H_{00}^-}{H_{00}^+} \right|^2 = \left| \frac{1}{m_{11}} \right|^2$$

To calculate the transmission and reflection coefficients the superlattice of figure 3.1 is embedded in a medium with permittivity ϵ, like for example vacuum. Using the transfer matrix approach the fields on both sides of the superlattice with n rotations are connected to each other by the matrix

$$\begin{pmatrix} E_0^+ \\ E_0^- \end{pmatrix} = \hat{M}_g \begin{pmatrix} E_n^+ \\ E_n^- \end{pmatrix} \tag{A.1}$$

with

$$\hat{M}_g = \hat{T}_{01} \left(\hat{P}_1 \hat{T}_{12} \hat{P}_2 \hat{T}_{21} \right)^n \hat{P}_1 \hat{T}_{12} \hat{P}_2 \hat{T}_{23} \tag{A.2}$$

The transfer matrices $\hat{T}_{01}$ and $\hat{T}_{23}$ denote the transfers functions of the fields to the surrounding media of the superlattice, the matrix products inside the brackets yield

the unit cell matrix already known from equation 3.9. The equation system above is overdefined, so there are two coefficients which can be chosen arbitrarely. Since the space behind the last layer extends to infinity the coefficient $E_n^- = 0$, i.e. no light is reflected behind the last layer of the superlattice. As last free parameter the field component E_n^+ can be set to 1, which leads to a normalisation for transmission and reflection coefficients. From this equation system the reflection as well as the transmission can be calculated:

$$R = \left| \frac{E_0^+}{E_0^-} \right|^2 = \left| \frac{m_{21}}{m_{11}} \right|^2 \tag{A.3}$$

$$T = \left| \frac{E_n^+}{E_0^+} \right|^2 = \left| \frac{1}{m_{11}} \right|^2 \tag{A.4}$$

As already shown in equation 3.13 the optical properties of the superlattice can be described by an anisotropic permittivity tensor in the effective medium approximation. Therefore the transmission and reflection coefficients can be expanded in powers of the layer thicknesses d_1 and d_2 to a form which equals the transmission and reflection coefficients through a slab with anisotropic permittivity:

$$R = |r|^2 = \left| \frac{\left(k_z^{*2} \epsilon^2 - k_z^2 \epsilon_x^2 \right) \sin \left(k_z^* d \right)}{\left(k_z^{*2} \epsilon^2 + k_z^2 \epsilon_x \right) \sin \left(k_z^* d \right) + 2 i k_z k_z^* \epsilon \epsilon_x \cos \left(k_z^* d \right)} \right|^2 \tag{A.5}$$

$$T = |t|^2 = \left| \frac{2}{2 \cos \left(k_z^* d \right) - i \left(\frac{k_z^* \epsilon}{k_{z0} \epsilon_x} + \frac{k_{z0} \epsilon}{k_z^* \epsilon_x} \right) \sin \left(k_z^* d \right)} \right|^2 \tag{A.6}$$

Both transmission and reflection are shown in figure A.1 for an effective medium consisting of silver and GaAs with a thickness of layer ratio $\eta = 1.3$. The light transmits perpendicularly through the medium, i.e. $k_x = 0$. As can be seen from equations A.5 and A.6 for $k_x = 0$ only the transversal component ϵ_x influences the transmission and reflection spectra, while the component ϵ_z is cancelled out.

Below the plasma frequency ω_p, where the effective medium becomes metallic, the transmission drops to zero while the reflection increases to almost 1. Above the plasma frequency the superlattice becomes transparent and light waves can propagate through the effective medium slab. Due to back reflections at the interfaces of the slab Fabry-Pérot resonances form oscillations in the reflectivity and transmission spectrum. For a clearer demonstration of these resonances the imaginary part of the *GaAs* permittivity was neglected in these calculation, so the oscillations are not damped away. By inverting equations A.5 and A.6 the effective permittivity ϵ_x can be retrieved. This will be investigated in further detail in chapter 4.2.
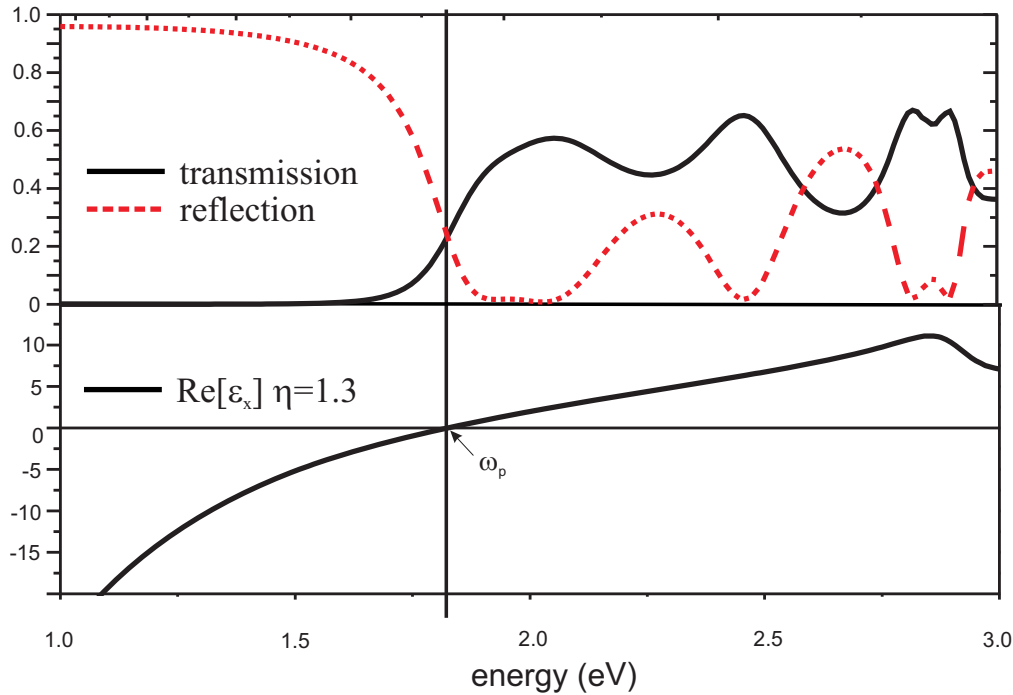
Figure A.1: Transmission for a lateral wavevector $k_x = 0$ for an effective medium consisting of GaAs and silver with a thickness of layer ratio of 1.3.

A.2 Dispersion in the effective medium approximation

As shown in chapter 3.1 the dispersion of Bloch waves in a superlattice is given by solving the eigenvalue equation:

$$\lambda(\omega, k_x) = \exp(i k_z^* \Delta) \tag{A.7}$$

where λ is the eigenvalue of the transfer matrix

$$\hat{M}_n = \begin{pmatrix} m_{11} & m_{12} \\ m_{21} & m_{22} \end{pmatrix} = \hat{P}_1 \hat{T}_{12} \hat{P}_2 \hat{T}_{21} \tag{A.8}$$

This matrix connects the fields of subsequent unit cells and $\Delta = d_1 + d_2$ is the lattice constant of the superlattice. The matrix $\hat{M}_n$ is unimodular, i.e. $det(M) = 1$. Therefore the eigenvalue is given by

$$\lambda = \frac{1}{2}(m_{11} + m_{22}) \pm \sqrt{\frac{1}{2}(a+b)^2 - 1} \tag{A.9}$$

Equation A.7 has a solution for $\frac{1}{2}|a+b| < 1$ and the dispersion for the real part of k_z^* is

$$\cos(k_z^* \Delta) = \frac{1}{2}(m_{11} + m_{22}) = \cos(k_{z1} d_1)\cos(k_{z2} d_2) - \frac{1}{2}(\kappa^{12} + \kappa^{21})\sin(k_{z1} d_1)\sin(k_{z2} d_2)$$

$$(A.10)$$

where k_{zi} and d_i are the wavevectors and thicknesses in each layer. If the thicknesses are much smaller than the wavelength of transmitted light this equation can be expanded by powers of $k_z^* \Delta$, $k_{z1}d_1$ and $k_{z2}d_2$ up to second order. Inserting the dispersion relation 3.2 for k_{zi} and neglecting powers higher than two for the layer thicknesses d_i one derives the dispersion relation:

$$k_z^{*2} = k_x^2 \frac{(d_1\epsilon_1 + d_2\epsilon_2)^2}{\Delta^2 \epsilon_1 \epsilon_2} + \left(\frac{\omega}{c}\right)^2 \frac{(d_1\epsilon_1 + d_2\epsilon_2)}{\Gamma} \tag{A.11}$$

Solving for $(\omega/c)^2$ yields the dispersion relation 3.13 for an anisotropic effective medium:

$$\left(\frac{\omega}{c}\right)^2 = \frac{k_x^2}{\epsilon_z} + \frac{k_z^2}{\epsilon_x} \tag{A.12}$$

with $\epsilon_x = \frac{d_1}{\Delta}\epsilon_1 + \frac{d_2}{\Delta}\epsilon_2$ and $\epsilon_z = \left(\frac{d_1}{\Delta}\frac{1}{\epsilon_1} + \frac{d_2}{\Delta}\frac{1}{\epsilon_2}\right)^{-1}$.

For TE polarized light the dispersion relation in the long wavelength limit becomes:

$$\left(\frac{\omega}{c}\right)^2 = \frac{1}{\epsilon_x}\left(k_x^2 + k_z^2\right) \tag{A.13}$$

This is the dispersion relation for an isotropic effective medium with the permittivity ϵ_x.

Appendix B

B.1 Sample parameters

All samples used in this thesis were grown by Dr. Holger Welsch and Andrea Stemmann by molecular beam epitaxy at our institute. The samples used for rolled-up superlattices had the following layout:

#2153		
Top layer	$Al_{0.3}Ga_{0.7}As$	17 nm
Strained layer	InAlGaAs	17 nm
Sacrificial layer	AlAs	40 nm
GaAs Substrate		
#2252		
Top layer	$Al_{0.3}Ga_{0.7}As$	10 nm
Strained layer	InAlGaAs	10 nm
Sacrificial layer	AlAs	40 nm
GaAs Substrate		

Samples for rolled-up metal/(In)GaAs arrays had the following layout:

#1988 - #1990		
Strained layer	InAlGaAs	3 nm, 4 nm, 6 nm
Sacrificial layer	AlAs	40 nm
GaAs Substrate		

B.2 Etching parameters

For shallow etching of the mesa a mixture of phosphoric acid and hydrogen peroxyde was used with a volume ratio:

$$H_3PO_4 : H_2O_2 = 500 : 1$$

Both components were stirred for at least one hour to achieve a constant etching rate. The etching rate was calibrated for each sample series and was about $1.3\,\mathrm{nm/s}$. The etched

surfaces are quite rough with an average roughness of about $6\,nm$. Therefore the etching has to be stopped several nanometers above the sacrificial layer to prevent leakage of the hydrofluoric acid through holes into the sacrificial layer. For rolled-up superlattices deep etching was performed by the same phosporic acid solution described above. For microroll arrays the U-shaped starting edge was etched by reactive-ion etching with the parameters:

$$\text{SiC}l_4 \quad : \quad 20\,\text{sccm}$$

$$P_{forward} \quad : \quad 100\,\text{W}$$

Generally we found that the deep etching of the starting edge has to be performed very shortly before the last etching step for a higher yield of rolled-up microrolls.

The selective etching of the $AlAs$ sacrificial layer was performed with diluted hydrofluoric acid, which shows a high selectivity with respect to GaAs. The concentration of the acid was 5% and 10%. We found that the yield of rolled-up microrolls increased for the higher concentration.

REFERENCES

[Abb73]   E. Abbe. *Beiträge zur Theorie des Mikroskops und der Mikroskopischen Wahrnehmung.* Archiv für Mikroskopische Anatomie **9**, 413 (1873).

[Ada85]   Sadao Adachi. *GaAs, AlAs, and $Al_xGa_{1-x}As$: Material Parameters for Use in Research and Device Applications.* Journal of Applied Physics **58**, R1–R29 (1985).

[AR03]   S. Anantha Ramakrishna and J. B. Pendry. *Removal of Absorption and Increase in Resolution in a Near-Field Lens via Optical Gain.* Phys. Rev. B **67**, 201101 (2003).

[Den05]   Ch. Deneke. *Aufgerollte Nanoröhren auf III-V Halbleiterbasis.* Dissertation, University of Stuttgart, 2005.

[Den07]   Christoph Deneke, Wilfried Sigle, Ulrike Eigenthaler, Peter A. van Aken, Gisela Schutz, and Oliver G. Schmidt. *Interfaces in Semiconductor/Metal Radial Superlattices.* Applied Physics Letters **90**, 263107 (2007).

[Dol06]   Gunnar Dolling, Christian Enkrich, Martin Wegener, Costas M. Soukoulis, and Stefan Linden. *Simultaneous Negative Phase and Group Velocity of Light in a Metamaterial.* Science **312**, 892–894 (2006).

[Fab08]   Nathalie Fabre, Loïc Lalouat, Benoit Cluzel, Xavier Mélique, Didier Lippens, Frédérique de Fornel, and Olivier Vanbésien. *Optical Near-Field Microscopy of Light Focusing through a Photonic Crystal Flat Lens.* Phys. Rev. Lett. **101**, 073901 (2008).

[Fan05]   Nicholas Fang, Hyesog Lee, Cheng Sun, and Xiang Zhang. *Sub-Diffraction-Limited Optical Imaging with a Silver Superlens.* Science **308**, 534–537 (2005).

[Ger08]   Nils Gerken. *Simulationsrechnungen an Metamaterialien.* Diplomarbeit, Universität Hamburg, Institut für Angewandte Physik, 2008.

[Gru03]   Marius Grundmann. *Nanoscroll Formation from Strained Layer Heterostructures.* Applied Physics Letters **83**, 2444–2446 (2003).

[Hey01]   Ch. Heyn. *Critical Coverage for Strain-Induced Formation of InAs quantum dots.* Phys. Rev. B **64**, 165306 (2001).

[Hjo96]   Klas Hjort. *Sacrificial Etching of III - V Compounds for Micromechanical Devices.* Journal of Micromechanics and Microengineering **6**, 370–375 (1996).

[Jac98]   John D. Jackson. *Classical Electrodynamics, 3. Auflage.* Wiley, 1998.

[Jac06]   Zubin Jacob, Leonid V. Alekseyev, and Evgenii Narimanov. *Optical Hyperlens: Far-field Imaging beyond the Diffraction Limit.* Opt. Express **14**, 8247–8256 (2006).

[Lam98]   Patrick Lambelet, Abdeljalil Sayah, Michael Pfeffer, Claude Philipona, and Fabienne Marquis-Weible. *Chemically Etched Fiber Tips for Near-Field Optical Microscopy: A Process for Smoother Tips.* Appl. Opt. **37**, 7289–7292 (1998).

[Liu07]   Zhaowei Liu, Hyesog Lee, Yi Xiong, Cheng Sun, and Xiang Zhang. *Far-Field Optical Hyperlens Magnifying Sub-Diffraction-Limited Objects.* Science **315**, 1686– (2007).

[Liu08]   Na Liu, Hongcang Guo, Liwei Fu, Stefan Kaiser, Heinz Schweizer, and Harald Giessen. *Three-dimensional Photonic Metamaterials at Optical Frequencies.* Nature Materials **7**, 31–37 (2008).

[MAP96]   Patrick J. Moyer Michael A. Paesler. *Near-Field Optics: Theory, Instrumentation, and Applications.* Wiley, 1996.

[Mat74]   J.W. Matthews and A.E. Blakeslee. *Defects in Epitaxial Multilayers: I. Misfit Dislocations.* Journal of Crystal Growth **27**, 118 – 125 (1974).

[Mei09]   Y. Mei, D. J. Thurmer, Ch. Deneke, S. Kiravittaya, Y. Chen, A. Dadgar, F. Bertram, B. Bastek, A. Krost, J. Christen, Th. Reindl, M. Stoffel, E. Coric, and O. G. Schmidt. *Fabrication, Self-Assembly, and Properties of Ultrathin AlN/GaN Porous Crystalline Nanomembranes: Tubes, Spirals, and Curved Sheets.* ACS Nano **3**, 1663–1668 (2009).

[Men05]   S. Mendach. *InGaAs-Mikro-und Nanoröhrchen.* Dissertation, University of Hamburg, 2005.

[Pal97]   Edward D. Palik. *Handbook of Optical Constants of Solids (5 Volume Set).* Academic Press, 1997.

[Pen99]   J.B. Pendry, A.J. Holden, D.J. Robbins, and W.J. Stewart. *Magnetism from Conductors and Enhanced Nonlinear Phenomena.* Microwave Theory and Techniques, IEEE Transactions on **47**, 2075–2084 (1999).

[Pen00]   J. B. Pendry. *Negative Refraction Makes a Perfect Lens.* Phys. Rev. Lett. **85**, 3966–3969 (2000).

[Pri00]   V. Ya. Prinz, V. A. Seleznev, A. K. Gutakovsky, A. V. Chehovskiy, V. V. Preobrazhenskii, M. A. Putyato, and T. A. Gavrilova. *Free-Standing and Overgrown InGaAs/GaAs Nanotubes, Nanohelices and their Arrays.* Physica E: Low-dimensional Systems and Nanostructures **6**, 828 – 831 (2000).

[Rac09]   K. Rachor. *Cyclotron Resonance of Carbon-Doped Two-Dimensional Hole Systems: From the Far-Infrared to the Microwave Regime.* Dissertation, Universität Hamburg, 2009.

[Ran00]   Jinendra K. Ranka, Robert S. Windeler, and Andrew J. Stentz. *Visible Continuum Generation in Air-Silica Microstructure Optical Fibers with Anomalous Dispersion at 800 nm.* Opt. Lett. **25**, 25–27 (2000).

[Rot10]   A. Rottler. *Analytical Calculations and Simulations on Rolled Up Metamaterials*. Diplomarbeit, Universität Hamburg, Institut für Angewandte Physik, 2010.

[Sch01]   Oliver G. Schmidt and Karl Eberl. *Nanotechnology: Thin Solid Films Roll Up into Nanotubes*. Nature **410**, 168–168 (2001).

[Sch05]   O. Schumacher, S. Mendach, H. Welsch, A. Schramm, Ch. Heyn, and W. Hansen. *Lithographically Defined Metal-Semiconductor-Hybrid Nanoscrolls*. Applied Physics Letters **86**, 143109 (2005).

[Sch06]   D. Schurig, J. J. Mock, B. J. Justice, S. A. Cummer, J. B. Pendry, A. F. Starr, and D. R. Smith. *Metamaterial Electromagnetic Cloak at Microwave Frequencies*. Science **314**, 977–980 (2006).

[Sch09]   Stephan Schwaiger, Markus Bröll, Andreas Krohn, Andrea Stemmann, Christian Heyn, Yuliya Stark, Daniel Stickler, Detlef Heitmann, and Stefan Mendach. *Rolled-Up Three-Dimensional Metamaterials with a Tunable Plasma Frequency in the Visible Regime*. Phys. Rev. Lett. **102**, 163903 (2009).

[Sha05]   Vladimir M. Shalaev, Wenshan Cai, Uday K. Chettiar, Hsiao-Kuan Yuan, Andrey K. Sarychev, Vladimir P. Drachev, and Alexander V. Kildishev. *Negative Index of Refraction in Optical Metamaterials*. Opt. Lett. **30**, 3356–3358 (2005).

[Smi00]   D. R. Smith, Willie J. Padilla, D. C. Vier, S. C. Nemat-Nasser, and S. Schultz. *Composite Medium with Simultaneously Negative Permeability and Permittivity*. Phys. Rev. Lett. **84**, 4184–4187 (2000).

[Smi05]   D. R. Smith, D. C. Vier, Th. Koschny, and C. M. Soukoulis. *Electromagnetic Parameter Retrieval from Inhomogeneous Metamaterials*. Phys. Rev. E **71**, 036617 (2005).

[Str39]   I.N. Stranski and L. Krastanov. Ber. Akad. Wiss. Wien **146**, 797 (1939).

[Tho89]   John A. Thornton and D.W. Hoffman. *Stress-Related Effects in Thin Films*. Thin Solid Films **171**, 5 – 31 (1989).

[Tsu97]   Y.C. Tsui and T.W. Clyne. *An Analytical Model for Predicting Residual Stresses in Progressively Deposited Coatings Part 1: Planar Geometry*. Thin Solid Films **306**, 23 – 33 (1997).

[Val08]   Jason Valentine, Shuang Zhang, Thomas Zentgraf, Erick Ulin-Avila, Dentcho A. Genov, Guy Bartal, and Xiang Zhang. *Three-Dimensional Optical Metamaterial with a Negative Refractive Index*. Nature **455**, 376–379 (2008).

[Veg21]   L. Vegard. *Die Konstitution der Mischkristalle und die Raumfüllung der Atome*. Zeitschrift für Physik A Hadrons and Nuclei **5**, 17 (1921).

[Ves68]   Viktor G Veselago. *The Electrodynamics of Substances with Simultaneously Negative Values of ϵ and μ*. Soviet Physics Uspekhi **10**, 509–514 (1968).

[Wel07]   H. Welsch. *Funktionalisierung von III/V-Halbleiterheterostrukturen durch Selbstorganisation und Nanostrukturierung*. Dissertation, University of Hamburg, 2007.

[WK91]   R. Müller W. Karthe. *Integrierte Optik*. Akademische Verlagsgesellschaft Geest & Portig K.-G., 1. Auflage, 1991.

[Woi96]   J. C. Woicik, K. E. Miyano, J. G. Pellegrino, P. S. Shaw, S. H. Southworth, and B. A. Karlin. *Strain and Relaxation in InAs and InGaAs Films Grown on GaAs(001)*. Applied Physics Letters **68**, 3010–3012 (1996).

[Xi09]   Sheng Xi, Hongsheng Chen, Tao Jiang, Lixin Ran, Jiangtao Huangfu, Bae-Ian Wu, Jin Au Kong, and Min Chen. *Experimental Verification of Reversed Cherenkov Radiation in Left-Handed Metamaterial*. Phys. Rev. Lett. **103**, 194801 (2009).

[Yak93]   B. I. Yakobson, P. J. Moyer, and M. A. Paesler. *Kinetic Limits for Sensing Tip Morphology in Near-Field Scanning Optical Microscopes*. Journal of Applied Physics **73**, 7984–7986 (1993).

Publications

- S. Schwaiger, M. Bröll, A. Krohn, A. Stemmann, Ch. Heyn, Y. Stark, D. Stickler, D. Heitmann, and S. Mendach, *Rolled-Up Three-Dimensional Metamaterials with a Tunable Plasma Frequency in the Visible Regime*, Phys. Rev. Lett. **102**, 163903 (2009)

Conference contributions

- 1st Mediterranean Conference on Nano-Photonics (MediNano-1), 6-7 October 2008, Instanbul, Turkey

- 2nd European Topical Meeting on Nanophotonics and Metamaterials (Nanometa 2009),
5-8 January, Seefeld, Austria

Danksagung

Im folgenden möchte ich mich bei allen bedanken, die zum Gelingen dieser Arbeit beigetragen haben:

- Professor Dr. Detlef Heitmann für die Möglichkeit, diese Arbeit in seiner Gruppe anfertigen zu dürfen, sowie für zahlreiche Diskussionen und Anregungen

- Professor Dr. Ulrich Merkt für die Übernahme des Zweitgutachtens der Dissertation und für die Organisation des Graduiertenkollegs

- Professor Dr. Wolfgang Hansen für die Übernahme des Zweitgutachtens der Disputation

- Dr. Stefan Mendach für die hervorragende Betreuung und Unterstützung, sowie seine mitreißende Begeisterung für Metamaterialien und den FC Bayern

- Den Diplomanden Stefan Schwaiger, Nils Gerken und Andreas Rottler, sowie den Werkstudenten Jochen Kerbst und Jens Ehlermann für die tolle Zusammenarbeit

- Dr. Holger Welsch, Andrea Stemmann und Dr. Christian Heyn für das Wachstum der in dieser Arbeit verwendeten Proben

- Daniel Stickler und Yuliya Stark für die FIB Präparation zahlreicher Nadeln und Proben

- Dr. Kevin Rachor für seine große Unterstützung während der FIR Messungen

- Herrn Klaus Beneke und der mechanischen Werkstatt

- Herrn Thomas Finger für die Instandhaltung und Betreuung des Reinraumes

- Allen Mitgliedern des Instituts für Angewandte Physik für die gute Arbeitsatmosphäre

- Meiner Familie für die immerwährende Unterstützung, die ich von ihnen erfahren habe

- Meiner Frau Daniela für die unzähligen, mannigfaltigen Reisen nach Hamburg, ihre große Geduld und Liebe und die wunderschöne Zeit mit ihr

- Der Deutschen Forschungsgemeinschaft für die Unterstützung und Finanzierung über das Graduiertenkolleg 1286 *Maßgeschneiderte Metall-Halbleiter-Hybridsysteme*